Chiral Thermodynamics of Nuclear Matter

PhD Thesis

by

Salvatore Fiorilla

September 2012

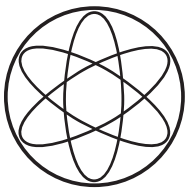

Technische Universität München

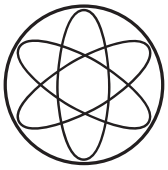

Technische Universität München

Physik-Department
Institut für Theoretische Physik T39
Univ.-Prof. Dr. Wolfram Weise

Chiral Thermodynamics of Nuclear Matter

Salvatore Fiorilla

Vollständiger Abdruck der von der Fakultät für Physik der Technischen Universität München zur Erlangung des akademischen Grades eines

Doktors der Naturwissenschaften (Dr. rer. nat.)

genehmigten Dissertation.

Vorsitzender:	Univ.-Prof. Dr. Stephan Paul
Prüfer der Dissertation:	1. Univ.-Prof. Dr. Wolfram Weise
	2. Univ.-Prof. Dr. Alejandro Ibarra

Die Dissertation wurde am 12.09.2012 bei der Technischen Universität München eingereicht und durch die Fakultät für Physik am 23.10.2012 angenommen.

Abstract

The equation of state of nuclear matter is calculated at finite temperature in the framework of in-medium chiral perturbation theory up to three-loop order. The dependence of its thermodynamic properties on the isospin-asymmetry is investigated. The chiral quark condensate is evaluated for symmetric nuclear matter. Its behaviour as a function of density and temperature sets important nuclear physics constraints for the QCD phase diagram.

Zusammenfassung

Die Zustandsgleichung von Kernmaterie wird bei endlicher Temperatur im Rahmen der chiralen Störungstheorie im Medium bis zur Dreischleifen-Ordnung berechnet. Die Abhängigkeit der thermodynamischen Eigenschaften nuklearer Materie von der Isospin-Asymmetrie wird untersucht. Das chirale Kondensat wird für symmetrische Kernmaterie berechnet. Das Verhalten dieses Kondensats als Funktion der Dichte und der Temperatur setzt wichtige kernphysikalische Randbedingungen für das Phasendiagramm der QCD.

Contents

Chapter 1

Introduction

In recent years the interest concerning the nuclear many-body problem has received a renewed impulse from the astrophysical side of this field of research. Crucial constraints on the equation of state of nuclear matter have recently come from accurate determinations of the masses and the radii of neutron stars [1, 2]. The study of the Shapiro delay in the binary radio pulsar systems has allowed to infer the mass of the pulsar J1614-2230 at a high level of accuracy, $M = (1.97 \pm 0.04) M_{\odot}$ [3]. A two-solar mass neutron star rules out almost all soft equations of state with hyperons and boson condensation. It is instead consistent with predictions arising from standard nuclear physics [2, 4].

The first step in describing the dynamics of a multi-nucleon system is to consider the simple case of a system consisting of just two nucleons, i.e. nucleon-nucleon (NN) scattering. In the early 1990's the Nijmegen group conducted an accurate analysis of all NN scattering data at energies below 350 MeV collected in almost 40 years and extracted thousands of reliable data [5]. The models of NN interaction that fits the Nijmegen database with $\chi_2/N_{\rm data} \sim 1$ are called "modern". "Modern" phenomenological potentials include the Nijmegen models [6], the Argonne v_{18} [7] and the CD-Bonn [8]. They all describe the long-distance part of the interaction, corresponding to inter-nucleon distances $r \gtrsim 2$ fm, by one-pion exchange, but follow different treatments at shorter distances. For instance, the CD-Bonn potential includes in addition two-pion exchange and that of σ, ρ and ω mesons. The Nijmegen potential comprehends a variety of mesons, such as $\pi, \eta, \eta', \rho, \omega, \phi, \delta$. However, nuclear matter with realistic NN interaction saturates at too high density and density-dependent interactions and three-nucleon interaction models have been proposed [9]. We note that these models have no connection with QCD, the gauge theory of strong interactions.

The Effective Field Theory (EFT) approach allows to organize the calculation in a systematic and model-independent way. After delineating the soft and hard scales of the problem in consideration, the most general Lagrangian consistent with the conserved and broken symmetries of the underlying theory, QCD, is written in terms of the active low-energy degrees of freedom. The effective Lagrangian is usually expanded in powers of the soft scales over the hard scale. A power counting scheme provides a method to estimate the magnitude of each contribution.

Chiral perturbation theory (ChPT) is a low-energy EFT of QCD, incorporating the spontaneous and explicit chiral symmetry breaking of the QCD Lagrangian with light quarks. Its characteristic breakdown (hard) scale is $\Lambda_\chi \sim 1$ GeV. The NN interaction is described in terms of the active degrees of freedom at the momentum scales involved, i.e. nucleons and pions. The pions are the Goldstone bosons arising from the spontaneous breaking of the chiral symmetry. One-pion exchange generates the long-range part of the NN interaction, two-pion exchange reproduces the attractive intermediate-distance NN interaction. Therefore perturbative pion-exchange dynamics are treated explicitly. The $\Delta(1232)$-isobar is the

first (spin-flip) excited state of the nucleon. Its inclusion as an explicit degree of freedom in ChPT improves the convergence of the theory. Within this scheme, many efforts have been made to understand the structure of nuclear forces. At the present time, the calculation of the nuclear potential is at the level of four-nucleon force contributions [11, 12].

We use ChPT for the description of nuclear matter. Our scheme is based on a separation of scales between the long- and intermediate-range physics, described primarily by pion-exchange dynamics, and the unresolved short-distance interaction, taken into account through contact terms tuned to reproduce some selected known properties of nuclear matter. The small scales in the nuclear medium problem are the pion mass $m_\pi \simeq 135$ MeV, the Fermi momentum k_F and the Δ-isobar - nucleon mass splitting $\Delta = 293$ MeV. Calculations are carried out using the in-medium nucleon propagator that accounts for the finite-density effects. Two-body and three-body correlations are systematically incorporated. The equation of state results in an expansion in powers of the soft scales over Λ_χ.

In this work we are going to extend in-medium ChPT formalism to perform calculations at finite temperature and for arbitrary isospin-asymmetry. The aim is to investigate the thermodynamic properties of nuclear matter and their modifications when varying the relative percentage of protons and neutrons. The remarkable aspect of our work is that, by adjusting a small number of contact terms, we are able to predict many realistic thermodynamic properties and features of nuclear matter. Moreover, we calculate the in-medium chiral condensate in symmetric nuclear matter and study its behaviour as a function of density and temperature to ascertain the presence or absence of a chiral phase transition in nuclear matter. The results constrain the location of the nuclear liquid-gas phase transition and of the chiral phase transition in the QCD phase diagram.

This thesis is organized as follows.

In chapter 2 we define nuclear matter and introduce its empirical properties used as constraints for the construction of the equation of state. These properties are obtained by extrapolation from nuclear data. From electron-nucleus scattering one obtains the saturation density ρ_0 of nuclear matter. From the semi-empirical mass formula one extrapolates the binding energy of infinite symmetric nuclear matter and the asymmetry energy at ρ_0. Multifragmentation studies of heavy-ion collision experiments indicate the presence of a liquid-gas phase transition in nuclear matter. Many different approaches and techniques have been developed to describe the properties of atomic nuclei and nuclear matter. We present a brief overview of the most common ones. In particular, we classify them into three categories: microscopic, phenomenological and effective field theory approaches.

Chapter 3 is dedicated to the construction of in-medium ChPT, the theoretical framework we adopt for the description of nuclear matter. In the first part of the chapter, we discuss the symmetries of the QCD Lagrangian with light quarks and introduce the chiral Lagrangian and the chiral power counting. The NN interaction is discussed up to next-to-leading order (NLO) in the chiral expansion. In the second part, the chiral formalism is generalized to finite densities with the individuation of the relevant scales and the definition of the in-medium nucleon propagator. The energy per particle of symmetric nuclear matter is calculated up to three-loop order in the diagrammatic expansion.

In chapter 4 we extend this computational scheme to finite temperatures and generalize it for arbitrary isospin-asymmetry. The appropriate thermodynamic potential is the free energy density. The only change in performing calculations at finite temperature is the replacement of the step function over the Fermi sea of the nucleons, appearing in the in-medium propagator, by the T-dependent momentum distribution function. The free energy density is then given by a sum of convolution integrals. The generalization to isospin-asymmetric nuclear matter requires to differentiate between proton and neutron medium insertions, because the Fermi momenta of the two particles are now different. We evalu-

ate numerically the equation of state of nuclear matter as a function of nucleon density at different temperatures and construct the corresponding phase diagrams. We study their isospin-dependence providing a complete picture of the evolution of the liquid-gas coexistence region for varying proton fraction $x_p = Z/A$. Finally, we make a comparison with some recent results obtained with other approaches.

In chapter 5 we consider the thermodynamic properties of the chiral (quark) condensate in symmetric nuclear matter. This is the order parameter of the chiral phase transition. It is expected to drop with increasing density and temperature. Through the Hellmann-Feynman theorem one can relate the chiral condensate to the derivative of the free energy per particle with respect to the pion mass. This derivative is straightforwardly performed because the pion mass is an explicit parameter in our computational scheme. We study the behaviour of the in-medium chiral condensate as a function of nucleon density and temperature and analyze the interplay of two-body and three-body forces. We find that the explicit involvement of Δ-isobar degree of freedom together with the Pauli principle for nucleons delays the decrease of the condensate with increasing density at low temperature. No indication of a chiral phase transition is found in the nuclear matter terrain of the QCD phase diagram.

Chapter 6 deals with a known problem affecting the equation of state at low density, especially in the case of neutron-rich matter. The perturbative expansion of the $\mathcal{T}$-matrix is invalidated by the large NN spin-singlet scattering length, $a_s \simeq 19$ fm. To treat the problem, we carry out an in-medium resummation of the S-wave contact interaction to all orders. The features of the resulting equation of state are discussed.

In chapter 7, we conclude this thesis with a summary of the results achieved and an outlook. The appendices report some details of the calculations.

Chapter 2

From Nuclei to Nuclear Matter

From a modern, QCD oriented point of view, the nucleon-nucleon interaction is interpreted as the residual strong interaction between the colorless nucleons composed of quarks and gluons. This interaction is responsible for the binding of the nucleons and the formation of atomic nuclei, the properties of which have been extensively investigated. These studies enable to perform extrapolations for systems with a large number of protons and neutrons where the electromagnetic forces can be ignored, defining the basic properties of nuclear matter. Another source of information about the behaviour of nuclear matter at finite temperature is provided by heavy-ion collision experiments.

Here we give a brief overview of theoretical approaches to nuclear matter that have been developed in the past decades.

2.1 Empirical Properties of Nuclear Matter

The experimental data of electron-nucleus scattering show that the charge density is almost constant within the nuclear volume. Assuming that the nucleus is a uniformly charged sphere with radius R, the following relation is valid:

$$R \simeq 1.21\, A^{\frac{1}{3}}\ \text{fm}\ . \tag{2.1}$$

The charge distribution measured by electron-nucleus scattering is different from the mass distribution of the nucleus containing both protons and neutrons. The central charge density $\rho(r=0)$ is almost constant, decreasing only slightly with increasing mass number. If we take into account the presence of the neutrons multiplying by A/Z, the nuclear density $\rho(0)\,A/Z$ is the same for almost all nuclei. By extrapolation, infinitely extended nuclear matter has a baryon density

$$\rho_0 \approx 0.16\,\text{nucleons/fm}^3\ . \tag{2.2}$$

The binding energy of the nucleons inside atomic nuclei is well parameterized by the Weizsäcker formula or semi-empirical mass formula, introduced in 1935. For a nucleus with Z protons and N neutrons the following phenomenological formula is worth:

$$B(A,Z) = a_v A - a_s A^{\frac{2}{3}} - a_c \frac{Z^2}{A^{\frac{1}{3}}} - \left(a_a + \frac{a_{as}}{A^{\frac{1}{3}}}\right)\frac{(N-Z)^2}{A} - \delta_P + E_D \tag{2.3}$$

This parametrization is inspired to the nuclear liquid drop model. The different terms have the following interpretation:

- *Volume term.* This contribution is proportional to the number of nucleons $A \sim R^3$. Therefore we deduce that a nucleon interacts only with its neighbours, otherwise the

dependence would be proportional to $A(A-1)$. Any nucleon in the interior of a large nucleus has a binding energy of about 16 MeV. This phenomenon is called saturation. The density ρ_0 defined in eq. (2.2) takes the name of saturation density.

- *Surface term.* Nucleons that are on the surface of the nucleus are surrounded by a smaller number of particles than nucleons that are inside the nucleus. The surface term is proportional to the square of the radius, $R^2 \sim A^{\frac{2}{3}}$.

- *Coulomb term.* The repulsive Coulomb interaction of Z protons in the nucleus can be approximated by assuming that the charge is uniformly distributed on a sphere of radius $R_c \sim A^{\frac{1}{3}}$.

- *Asymmetry term.* With increasing mass number nuclei become richer in neutrons than protons. The corresponding coefficient in eq. (2.3) distinguishes between the bulk asymmetry energy proportional to $a_a \approx 33$ MeV and the surface asymmetry energy proportional to a_{as}.

- *Pairing term.* Nuclei with an even number of protons and/or neutrons are most stable.

- *Deformation term.* The energy E_D takes into account the deformation effects coming from the non-perfect sphericity of the nuclei.

A piece of information of primary interest for us is the coefficient of the asymmetry term, a_s, with a value of about 33 MeV once finite size effects are taken into account [13] .

We now consider the limit $A \to \infty$ in eq. (2.3). If we turn off the Coulomb interaction, only the volume and asymmetry terms survive. The binding energy per nucleon for infinitely extended nuclear matter is

$$\bar{B}(\delta) = a_v + a_a \delta^2, \tag{2.4}$$

with $\delta = (N - Z)/A$ the asymmetry parameter. This simple expression, derived by the semi-empirical mass formula, is actually a good approximation of the energy per nucleon in nuclear matter at the saturation point $\rho_0 \approx 0.16\,\mathrm{fm}^{-3}$. We discuss it in more detail in section 4.8. Note that symmetric nuclear matter ($N = Z$) has a binding energy per nucleon of about 16 MeV at ρ_0.

Last but not least, heavy-ion collision experiments show evidence for a phase transition occurring in nuclear matter. The caloric curves of the nuclear fragments produced in nucleus-nucleus collision experiments present a plateau usually interpreted as being related to the latent heat of a liquid-gas first-order phase transition [14–16].

2.2 Approaches to the Nuclear Many-Body Problem

The construction of a realistic equation of state of nuclear matter is one of the key problems in nuclear physics and astrophysics. It represents an essential input for the description of nuclear properties and the modeling of dense matter produced in heavy-ion collisions and formed in the center of neutron stars.

Starting from the pioneering work of Brueckner et al. [17] in the late 1960's, many different approaches and numerical techniques are nowadays available for dealing with the nuclear many-body problem. They can be classified into three categories [18]: microscopic many-body approaches, phenomenological approaches and effective field theory approaches.

2.2.1 Microscopic Many-Body Approaches

BHF approach. The Brueckner-Hartree-Fock approach [19–21] is a mean-field theory at lowest order of the non-relativistic Brueckner-Bethe-Goldstone theory. The main problem with the application of perturbative techniques to nuclear matter is the divergence of the transition matrix elements because of the strongly repulsive core in the NN interaction. The Hamiltonian is then split in two pieces by means of a single-particle auxiliary potential U in order to speed-up the convergence of the expansion:

$$H = (H_0 + U) + (V - U) = H_0' + V' \ , \tag{2.5}$$

$$H_0' = \sum_{\vec{k}} \left[-\frac{k^2}{2M} + U(\vec{k}\,) \right] = \sum_{\vec{k}} e_k \, a_{\vec{k}}^\dagger \, a_{\vec{k}}. \tag{2.6}$$

The e_k's are interpreted as the new single-particle spectrum. V' is the interaction Hamiltonian that is treated perturbatively summing the infinite set of ladder diagrams arising from its iteration. The auxiliary potential U is not unique and must be chosen in such a way as to make the expansion convergent.

The diagrammatic expansion gives rise to diagrams with insertions of the potentials V and U and can be ordered according to the number n of hole-lines, where n hole-lines correspond to n-body correlations. The infinite set of diagrams with the insertion of the potential V can be formally summed up by introducing the G-matrix equation:

$$G = V - V \frac{Q}{W} G \ , \tag{2.7}$$

where W is the energy denominator related to the propagation of the intermediate state and Q is an operator that forbids scattering to states in the Fermi sea ($k > k_F$). The G-matrix represents an effective in-medium NN interaction and regularizes the non-perturbative short-range part of the NN interaction.

At two hole-line approximation, the corresponding sum of diagrams leads to the Brueckner-Hartree-Fock (BHF) approximation. There are essentially two ways of choosing the auxiliary potential U. In the "standard choice" or "gap choice", it is assumed that the potential is rigorously zero for $k > k_F$. In the "continuous choice" the potential is extended to momenta larger than k_F, making it a continuous function through the Fermi surface.

CBF approach. The Correlated Basis Functions approach or variational approach looks for a optimal set of wave functions or states of the system that makes it possible to treat the problem in a perturbative way [22–27]. Rather than implementing the non-perturbative effects by means of a matrix equation as in the BHF approach, these effects are now directly included in the choice of the basis functions.

The unperturbed Fermi gas states $|n_0\rangle$ are replaced by the correlated states

$$|n\rangle = \frac{F\,|n_0\rangle}{\langle n_0\,|\,F^\dagger F\,|\,n_0\rangle} \ , \tag{2.8}$$

where F is the correlation operator whose structure reflects that of the NN interaction. Assuming a certain operatorial structure for F, the latter is fully determined by the variational method minimizing the expectation value of the ground state, $E_V = \langle 0|H|0\rangle$.

Once the correlation operator F has been determined, the Hamiltonian is split into two parts as in eq. (2.5). H_0' is diagonal in the correlated basis, while V' contributes with off-diagonal elements. If F is well chosen, E_V results close to the eigenvalue of H_0', the correlated states have a large overlap with the true eigenstates of the system and the matrix elements of V' are small.

The calculation of the matrix elements of H between correlated states is extremely difficult due to the large number of particles involved. A possible procedure is that of

expanding the matrix elements in a series whose terms represent the contribution of clusters with an increasing number of particles. The terms in this series can be summed up to all orders by solving a set of coupled integral equations known as Fermi hyper-netted chain equations [28–31].

SCGF approach. In the self-consistent Green's function approach the in-medium single-particle propagator, obtained via the Dyson equation by summing all ladder diagrams generated by the iteration of the effective interaction, is the key ingredient to calculate the binding energy and the single-particle properties of nuclear matter [32–34]. Particles and holes are treated on an equal footing in contrast to the BHF approach where only intermediate particles with momenta above the Fermi sea ($k > k_F$) are considered in the ladder diagrams.

DBHF approach. The Dirac-Brueckner-Hartree-Fock approach is a relativistic extension of the BHF approach. Its formalism is based on a quantum field theoretical model for nucleons, and their interaction with mesons [35–41]. The essential point is to use the Dirac equation for the single particle motion in the nuclear medium. The free NN interaction is described by a one-boson-exchange model. Two-nucleon scattering is implemented in the medium by means of the covariant Bethe-Salpeter equation through a self-consistent summation of the ladder diagrams. The common feature of all DBHF results is a density-dependent relativistic many-body repulsion that is able to describe the saturation properties of nuclear matter. In fact, the relativistic approach describes quite well the binding energy and the saturation density of symmetric nuclear matter in contrast to corresponding non-relativistic calculations.

2.2.2 Phenomenological Approaches

These schemes are based on effective density-dependent nuclear forces or effective interaction Lagrangians with parameters fitted to known properties of atomic nuclei or nuclear matter. This category includes the RMF models [42–44], the Hartree-Fock approaches [45–47], Thomas-Fermi approximations and phenomenological potential models.

RMF model. The relativistic mean field model uses effective interaction Lagrangians with nucleons interacting through the exchange of mesons ($\sigma - \omega$ model, for instance). The operators of the meson fields are replaced by their expectation values.

Non-relativistic Hartree-Fock approach. We mention here the Skyrme-Hartree-Fock approach based on effective energy-density functionals. One of the first thermodynamic studies of the equation of state of nuclear matter was conducted using this approach [48].

2.2.3 Effective Field Theory Approach

The Effective Field Theory (EFT) approach is used to systematically describe the low-energy behaviour of a physical system. After identifying the active degrees of freedom in the momentum range of interest, one can write the effective Lagrangian according to the basic principle of the EFT approach enunciated by Weinberg [49]: the construction of the most general Lagrangian consistent with the symmetries of the underlying interaction leads to the most general scattering matrix consistent with these symmetries. The effective Lagrangian is perturbatively expanded in powers of the ratio of the soft momenta over the hard scale. A power counting scheme specifies the terms required at a given accuracy. A separation of scales between the non-perturbative short-range physics and the (perturbative) long-range dynamics is introduced. This division is characterized by a breakdown scale that determines the radius of convergence and the range of applicability of the theory. The resulting effective interaction is used to derive the equation of state of nuclear matter in a controlled way, i.e. in an expansion in powers of the Fermi momentum.

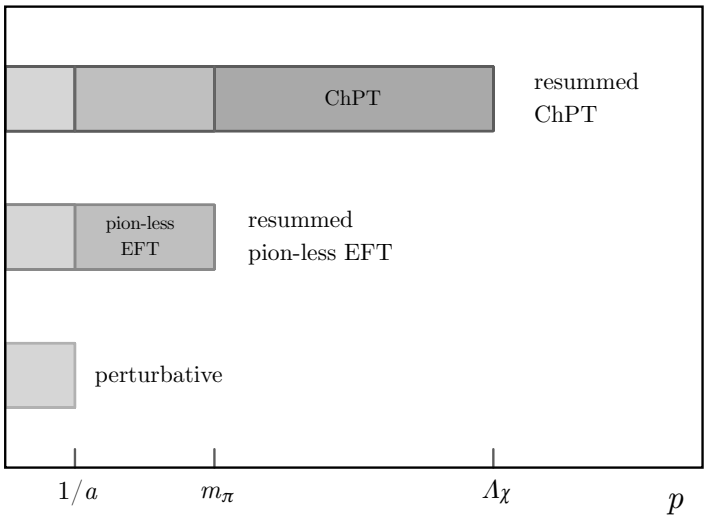

Figure 2.1: Characteristic momentum scales in the NN scattering problem and range of validity of the corresponding EFTs.

We can clarify the concepts of range of validity and breakdown scale of an EFT considering the NN scattering problem, for instance, identifying the relevant characteristic scales depending on the momenta involved. They are displayed in Fig. 3.1. At low energy, the problem is characterized by the scattering lengths of the NN channels. Consider neutron-proton scattering. The corresponding scattering lengths range from $a(^1S_0) \simeq 5.4$ fm for the spin-singlet case to $a(^3S_1) \simeq 24$ fm for the spin-triplet case. The latter sets a hard scale of $1/a(^3S_1) \approx 8.2$ MeV for a perturbative treatment of the problem. If we want to extend the theory to higher momenta, we have to perform a non-perturbative resummation of the S-wave NN interaction to all orders (see Ref. [50]). As long as pion-exchange dynamics are not treated explicitly, the limiting scale of this pion-less effective field theory is the pion mass m_π. The inclusion of the pion-exchange dynamics leads to ChPT and extends the convergence of the expansion in powers of the soft momenta up to $\Lambda_\chi \sim 1$ GeV.

ChPT is the approach we adopt for our description of nuclear matter and we present it in detail in the next chapter [51–56]. The problem of the non-perturbative resummation of the S-wave contact interaction arising from the large NN scattering length is discussed in chapter 6 [50, 57]. In addition to in-medium ChPT, the EFT approach includes also the density functional theory (DFT), oriented to the calculation of the properties of finite nuclei [58–61].

Chapter 3

Chiral Perturbation Theory for Nuclear Matter

The strong interactions between quarks are described by the gauge theory called Quantum chromodynamics (QCD) based on the $SU(3)$ color symmetry. In particular, quark fields interact through the exchange of massless bosons, the *gluons*. In contrast to QED, QCD is a non-abelian gauge theory, a feature which has important consequences. While the electromagnetic interaction is weak at large distances and strong at small distances, in QCD the opposite behaviour takes place: the interaction between coloured objects is weak at small distances (*asymptotic freedom*) and become strong for distances larger than about 1 fm, so strong to bind and confine the quarks in colorless objects, the hadrons. Consequently, perturbation theory can be used only at high energies, whereas the low-energy regime is non-perturbative. This is the case for the nuclear interactions.

The description of nuclear forces in terms of quarks and gluons from QCD is enormously complicated. One can try to gain information by solving the field equations numerically on a discretized, Euclidean space-time lattice with huge computing power. This field of research, called Lattice QCD, is useful for investigating how hadron physics emerges from QCD. For practical nuclear physics calculations, however, it does not represent a realistic tool so far.

An efficient approach is that of building an effective field theory representing the low-energy QCD. The first step is to identify the relevant scales. A characteristic feature that one encounters in the hadron spectrum is the big gap between the masses of the pions (~ 135 MeV) and the masses of the vector mesons ($m_\rho = 770$, for instance). So we can assume the pion mass is a soft scale, $Q \sim m_\pi$, and the ρ mass the hard scale, $\Lambda_\chi \sim m_\rho$. An estimation based on consistency arguments concerning the meson-meson scattering sets as hard scale $\Lambda_\chi \approx 4\pi f_\pi \sim 1$ GeV [62], where $f_\pi = 92.4$ MeV. The effective theory will consist of an expansion of the lagrangian in powers of Q/Λ_χ. Therefore the active degrees of freedom are no longer quarks and gluons but pions coupled to heavy sources such as nucleons. The link to QCD is given by Weinberg's theorem [49]: it states that the effective field theory must share all symmetries of the basic theory. The construction of the effective field theory of low-energy QCD can be summarized in the following five points [56]:

- Identification of the soft and hard scales and the active degrees of freedom.
- Identification of the symmetries of QCD and their possible breaking.
- Construction of the most general lagrangian respecting the conserved and broken symmetries of QCD.
- Elaboration of a power counting, an organization scheme that allows to identify a hierarchy of important contributions in a low-momentum expansion.

- Calculation of the Feynman diagrams of the different contributions up to desired accuracy.

This lists the steps leading to *Chiral Perturbation Theory* (ChPT), to be described in the present chapter. Still, our primary purpose is to attack the nuclear many-body problem and obtain predictions for the properties of nuclear matter. So the last part of the chapter is dedicated to the extension of ChPT to systems at finite density using the novel approach developed in Refs. [53–55] and relying on the separation between long- and short-distance dynamics.

3.1 Symmetries of QCD

3.1.1 Chiral Symmetry

The first point of the list of "things to be done" for the construction of an effective field theory has already been discussed. We now proceed to the second point, the study of the symmetries of the low-energy QCD lagrangian. This is written as follows:

$$\mathcal{L}_{QCD}(x) = \bar{q}(x)\,(i\gamma^\mu D_\mu - M)\,q(x) - \frac{1}{4}\,G_{\mu\nu,a}(x)\,G^{\mu\nu,a}(x)\ . \tag{3.1}$$

Quarks exist in six different flavours. Three of them, the u, d and s quarks, have a mass smaller than Λ_χ. In low-energy QCD only these three quarks are relevant. In our model for nuclear interactions no strange particle appears, so we restrict the discussion to the two flavour case, with up and down quarks. Under such restriction the quark field $q(x)$ is a flavour doublet

$$q(x) = \begin{pmatrix} u(x) \\ d(x) \end{pmatrix} \tag{3.2}$$

and the fields $u(x)$ and $d(x)$ are in turn colour triplets

$$u(x) = \begin{pmatrix} u_r(x) \\ u_g(x) \\ u_b(x) \end{pmatrix}\ , \qquad d(x) = \begin{pmatrix} d_r(x) \\ d_g(x) \\ d_b(x) \end{pmatrix}\ . \tag{3.3}$$

M is a diagonal 2×2 matrix containing the quark masses m_u and m_d. D_μ is the covariant derivative

$$D_\mu = \partial_\mu - ig\frac{\lambda_a^C}{2}A_{\mu,a}(x)\ , \tag{3.4}$$

with λ_a^C the eight linearly independent 3×3 Gell-Mann matrices, the generators of the $SU(3)$ colour symmetry group. $A_{\mu,a}$ $(a = 1, \ldots 8)$ are the gluon fields and g is the strong coupling constant. $G_{\mu\nu,a}(x)$ is the gluon strength tensor defined as

$$G_{\mu\nu,a}(x) = \partial_\mu A_{\nu,a}(x) - \partial_\nu A_{\mu,a}(x) + g f_{abc}\,A_{\mu,b}(x)\,A_{\nu,c}(x)\ , \tag{3.5}$$

with f_{abc} the fine structure constants of the $SU(3)$ group. The non-abelian character of QCD appears in the last term of $G_{\mu\nu,a}(x)$, in which the gluon fields interact with each other.

According to the PDG [63], the masses of the u and d quarks are:

$$m_u = 2.5^{+0.6}_{-0.8}\ \text{MeV}\ , \qquad m_d = 5.0^{+0.7}_{-0.9}\ \text{MeV}\ , \tag{3.6}$$

at a renormalization scale $\mu = 2$ GeV. These values are very small compared to the characteristic scale Λ_χ, so it is meaningful to discuss the QCD Lagrangian in the limit of vanishing quark masses. In eq. (3.1) we set $M = 0$. As a consequence, the Lagrangian acquires the

so called chiral symmetry. By introducing the left-handed and the right-handed projection operators

$$P_R = \frac{1+\gamma_5}{2} \ , \qquad P_L = \frac{1-\gamma_5}{2} \ , \tag{3.7}$$

we define the right-handed and the left-handed quark fields:

$$q_R = P_R\, q \ , \qquad q_L = P_L\, q \ . \tag{3.8}$$

In terms of these fields, the Lagrangian reads

$$\mathcal{L}^0_{QCD} = \bar{q}_L\, i\gamma^\mu D_\mu\, q_L + \bar{q}_R\, i\gamma^\mu D_\mu\, q_R - \frac{1}{4}\, G_{\mu\nu,a}\, G^{\mu\nu,a} \ . \tag{3.9}$$

We note that for vanishing quark masses, the left-handed and the right-handed quark fields decouple. In this limit the Lagrangian $\mathcal{L}^0_{QCD}$ is invariant under the following global unitary transformations:

$$q_L \longrightarrow U_L\, q_L = e^{-i\theta_i^L \frac{\tau_i}{2}}\ e^{-i\theta_L} q_L \ , \tag{3.10}$$

$$q_R \longrightarrow U_R\, q_R = e^{-i\theta_i^R \frac{\tau_i}{2}}\ e^{-i\theta_R} q_R \ , \tag{3.11}$$

where U_L and U_R are two independent unitary 2×2 matrices, τ_i with $i = 1, 2, 3$ are the (isospin) Pauli matrices and the θ's are the parameters of the transformations acting in flavour space. $\mathcal{L}^0_{QCD}$ has a classical global $U(2)_L \times U(2)_R$ symmetry. Applying Noether's theorem we find $2 \times (3+1) = 8$ conserved currents:

$$L_i^\mu = \bar{q}_L \gamma^\mu \frac{\tau_i}{2} q_L \ , \qquad L^\mu = \bar{q}_L \gamma^\mu q_L \ . \tag{3.12}$$

$$R_i^\mu = \bar{q}_R \gamma^\mu \frac{\tau_i}{2} q_R \ , \qquad R^\mu = \bar{q}_R \gamma^\mu q_R \ . \tag{3.13}$$

The 6 currents L_i^μ and R_i^μ are associated with the $SU(2)_L \times SU(2)_R$ symmetry, while the remaining two currents L^μ and R^μ are linked to the $U(1)_L \times U(1)_R$ symmetry. The left-hand and right-hand currents are also written in terms of vector and axial currents:

$$V_i^\mu = \bar{q}\gamma^\mu \frac{\tau_i}{2} q = R_i^\mu + L_i^\mu \ , \qquad V^\mu = \bar{q}\gamma^\mu q = R^\mu + L^\mu \tag{3.14}$$

$$A_i^\mu = \bar{q}\gamma^\mu\gamma_5 \frac{\tau_i}{2} q = R_i^\mu - L_i^\mu \ , \qquad A^\mu = \bar{q}\gamma^\mu\gamma_5\, q = R^\mu - L^\mu \ . \tag{3.15}$$

To summarize, the total symmetry group of $\mathcal{L}^0_{QCD}$ is $SU(3)_{color} \times SU(2)_L \times SU(2)_R \times U(1)_V \times U(1)_A$. However, the singlet axial current is conserved only on a classical level. The associated symmetry is broken by quantization ("$U(1)_A$ anomaly") and is no longer a symmetry of the system. $U(1)_V$ is related to the conservation of the baryon number. According to this property, we can classify the particles into mesons with $B = 0$ and baryons with $B = 1$.

The charge operators satisfy the commutation relations of the $SU(2)_L \times SU(2)_R \times U(1)_V$ Lie algebra:

$$Q_i^L = \int \mathrm{d}^3x\, q_L^\dagger \frac{\tau_i}{2} q_L \ , \qquad Q_i^R = \int \mathrm{d}^3x\, q_R^\dagger \frac{\tau_i}{2} q_R \ , \tag{3.16}$$

$$[Q_i^L, Q_j^L] = i\epsilon_{ijk}\, Q_k^L \ , \qquad [Q_i^R, Q_j^R] = i\epsilon_{ijk}\, Q_k^R \ , \qquad [Q_i^L, Q_j^R] = 0 \ , \tag{3.17}$$

$$[Q_i^L, Q^V] = [Q_i^R, Q^V] = 0 \ . \tag{3.18}$$

In terms of the vector and axial charge operators the commutation rules are:

$$[Q_i^V, Q_j^V] = i\epsilon_{ijk}\, Q_k^V \ , \qquad [Q_i^A, Q_j^A] = i\epsilon_{ijk}\, Q_k^V \ , \qquad [Q_i^V, Q_j^A] = i\epsilon_{ijk}\, Q_k^A \tag{3.19}$$

$$[Q_i^V, Q^V] = [Q_i^A, Q^V] = 0 \ . \tag{3.20}$$

3.1.2 Explicit Chiral Symmetry Breaking

The chiral symmetry is exact only for vanishing quark masses and is broken by the mass term in eq. (3.1). This can be easily seen writing the mass term in terms of the left- and right-handed quark fields:

$$\mathcal{L}_M = -\bar{q}Mq = -\bar{q}_R M q_L - \bar{q}_L M q_R \ . \tag{3.21}$$

The mass term mixes left-handed and right-handed quarks. We write explicitly the matrix M:

$$M = \begin{pmatrix} m_u & 0 \\ 0 & m_d \end{pmatrix} = \frac{m_u + m_d}{2} I + \frac{m_u - m_d}{2} \tau_3 \ . \tag{3.22}$$

Because of the negligible mass of the quarks, the chiral symmetry breaking is small. In the particular case of $m_u = m_d$, the second term in (3.22) vanishes and the Lagrangian recovers the $SU(2)_V$ symmetry, better known as isospin symmetry.

3.1.3 Spontaneous Chiral Symmetry Breaking

What are the physical implications of the $SU(2)_V \times SU(2)_A$ symmetry? The associated charge operators commute with the Hamiltonian. So, with regard to the vector symmetry, we expect to find degenerate isospin multiplets in the hadron spectrum. This is indeed the case: neutron and proton, π^+, π^0 and π^-, ρ^+, ρ^0 and ρ^-, just to mention some of them. The axial charges Q_i^A have instead negative parity and degenerate parity doublets should be associated with the axial symmetry. However, for the ρ-meson is an isospin triplet with $J^P = 1^-$ and mass about 775 MeV, the lightest meson with the same quantum numbers but opposite parity is the a_1-meson. Its mass is 1230 MeV and cannot at all be considered as degenerate with the ρ-meson. We conclude that the $SU(2)_A$ symmetry is spontaneously broken.

Given a symmetry of the Lagrangian, the ground state of the theory can share the same symmetry of the Lagrangian or not. In the first case the charge operators annihilate the vacuum, $Q_i^A |0\rangle = 0$ for example, and we have the so called *Wigner-Weyl realization* of the symmetry. In the second case, the charge operators do not annihilate the vacuum, $Q_i^A |0\rangle \neq 0$, and the so called *Nambu-Goldstone realization* of the symmetry takes place. The Goldstone theorem states that there exists a massless Goldstone boson with spin zero for each operator that does not annihilate the vacuum, and with the same quantum numbers as this operator.

From the breaking of $SU(2)_A$, three Goldstone bosons are generated and we identify them with the pion triplet. In the more general three flavour case we expect eight Goldstone bosons that can be identified with the pseudoscalar meson octet. However, these mesons are not massless, because the symmetry is not exact but explicitly broken by the finite mass of the quarks. So the pions are the result of both the spontaneous and the explicit chiral symmetry breaking. Pions are degenerate with the vacuum and their interactions must vanish at zero momentum and in the chiral limit $m_\pi \to 0$.

3.2 Chiral Effective Lagrangian

We are at the third point of the list, the construction of the most general effective Lagrangian with the same conserved and broken symmetries of the QCD Lagrangian. Such effective Lagrangian results in an expansion in powers of Q/Λ_χ, where, as already mentioned, Q is a soft scale, the pion momentum or the pion mass.

3.2.1 Pion sector

The pion-pion Lagrangian is expanded in even powers of the soft scale because of Lorentz invariance:

$$\mathcal{L}_{\pi\pi} = \mathcal{L}^{(2)}_{\pi\pi} + \mathcal{L}^{(4)}_{\pi\pi} + \dots \tag{3.23}$$

The superscript indicates the number of derivatives or pion mass insertions. The interaction behaves correctly at zero momentum and in the chiral limit.

The leading order (LO) term is written as:

$$\mathcal{L}^{(2)}_{\pi\pi} = \frac{1}{4} f_\pi^2 \,\mathrm{Tr}\left[\partial_\mu U \partial^\mu U^\dagger + m_\pi^2 (U + U^\dagger)\right] \ . \tag{3.24}$$

The trace is in isospin space, f_π can be identified with the pion decay constant after evaluating the weak pion decay $\pi^+ \to \mu^+ \nu_\mu$. U is a $SU(2)$ matrix in flavour space containing the pion fields. It can be parameterized in different ways. The usual choices are the exponential parameterization [1]

$$U = e^{i(\boldsymbol{\tau}\cdot\boldsymbol{\pi})/f_\pi} \ , \tag{3.25}$$

and the sigma parameterization

$$U = (\sigma + i\,\boldsymbol{\tau}\cdot\boldsymbol{\pi})/f_\pi \ , \qquad \sigma = \sqrt{f_\pi^2 - \boldsymbol{\pi}^2} \ . \tag{3.26}$$

If we expand U in powers of pion field π we obtain:

$$U = 1 + \frac{i}{f_\pi}\boldsymbol{\tau}\cdot\boldsymbol{\pi} - \frac{1}{2f_\pi^2}\boldsymbol{\pi}^2 - \frac{i\,\alpha}{f_\pi^3}(\boldsymbol{\tau}\cdot\boldsymbol{\pi})^3 + \frac{8\alpha - 1}{8f_\pi^2}\boldsymbol{\pi}^4 + \dots \ , \tag{3.27}$$

with $\alpha = 1/6$ for the exponential parameterization and $\alpha = 0$ for the sigma parameterization. Clearly, the observables must not depend on the unphysical parameter α. Under global chiral rotations, U transforms as:

$$U \longrightarrow g_L\, U\, g_R^\dagger \ , \tag{3.28}$$

where $g_L = e^{-i\theta_i^L \frac{\tau_i}{2}}$ and $g_R = e^{-i\theta_i^R \frac{\tau_i}{2}}$ are elements of $SU(2)_L \times SU(2)_R$. The Lagrangian (3.24) is then invariant under the transformation (3.28). After replacing the expansion (3.27) in (3.24), we find the following lowest order Lagrangian:

$$\begin{aligned}\mathcal{L}^{(2)}_{\pi\pi} = \frac{1}{2}\partial_\mu\boldsymbol{\pi}\cdot\partial^\mu\boldsymbol{\pi} - \frac{1}{2}m_\pi^2\boldsymbol{\pi}^2 + \frac{1-4\alpha}{2f_\pi^2}(\boldsymbol{\pi}\cdot\partial_\mu\boldsymbol{\pi})(\boldsymbol{\pi}\cdot\partial^\mu\boldsymbol{\pi}) \\ - \frac{\alpha}{f_\pi^2}\boldsymbol{\pi}^2\partial_\mu\boldsymbol{\pi}\cdot\partial^\mu\boldsymbol{\pi} + \frac{8\alpha-1}{8f_\pi^2}m_\pi^2\boldsymbol{\pi}^4 + \mathcal{O}(\boldsymbol{\pi}^6)\end{aligned} \tag{3.29}$$

The first two terms are the kinetic term and the mass term of the pion field. The other terms describe the interaction between 4 pions, 6 pions and so forth.

3.2.2 Baryon sector

At leading order the most general relativistic πN Lagrangian is [64] :

$$\mathcal{L}^{(1)}_{\pi N} = \bar\psi\left(i\gamma^\mu D_\mu - M_N + \frac{1}{2}g_A\gamma^\mu\gamma_5 u_\mu\right)\psi \ , \tag{3.30}$$

[1] We use the arrow to indicate vectors in coordinate space, such as $\vec{r}$, $\vec{p}$, $\vec{\sigma}$, and the bold symbol to indicate vectors in isospin space, such as $\boldsymbol{\tau}$, $\boldsymbol{\pi}$. This notation is useful to easily recognize scalar products in Dirac space and in isospin space.

where $\psi = (p, n)^T$ is the nucleon field composed of the isospin doublet of proton and neutron fields and g_A the axial vector coupling constant. The covariant derivative is given by

$$D_\mu = \partial_\mu + \Gamma_\mu \ , \tag{3.31}$$

where Γ_μ is the chiral connection:

$$\Gamma_\mu = \frac{1}{2}[\xi^\dagger, \partial_\mu \xi] = \frac{i}{4f_\pi^2}\epsilon_{abc}\,\tau_a\,\pi_b\,\partial_\mu\pi_c + \mathcal{O}(\boldsymbol{\pi}^4) \ , \qquad \xi = \sqrt{U} \ , \tag{3.32}$$

which couples the nucleon with an even number of pions. Instead, u_μ couples the nucleon with an odd number of pions:

$$u_\mu = i\{\xi^\dagger, \partial_\mu \xi\} = -\frac{1}{f_\pi}\boldsymbol{\tau}\cdot\partial_\mu\boldsymbol{\pi} + \frac{4\alpha - 1}{2f_\pi^3}(\boldsymbol{\tau}\cdot\boldsymbol{\pi})(\boldsymbol{\pi}\cdot\partial_\mu\boldsymbol{\pi}) + \frac{\alpha}{f_\pi^3}\boldsymbol{\pi}^2(\boldsymbol{\tau}\cdot\partial_\mu\boldsymbol{\pi}) + \mathcal{O}(\boldsymbol{\pi}^5). \tag{3.33}$$

Inserting in the Lagrangian (3.30) we obtain:

$$\mathcal{L}_{\pi N}^{(1)} = \bar{\psi}\left(i\gamma^\mu\partial_\mu - M_N - \frac{1}{4f_\pi^2}\gamma^\mu\epsilon_{abc}\,\tau_a\,\pi_b\,\partial_\mu\pi_c - \frac{g_A}{2f_\pi}\gamma^\mu\gamma_5\boldsymbol{\tau}\cdot\partial_\mu\boldsymbol{\pi} + \dots\right)\psi \tag{3.34}$$

The term containing the Levi-Civita tensor is called *Weinberg-Tomozawa* coupling. It is a 2π-contact term arising from the covariant derivative. The term proportional to g_A is the known axial vector derivative coupling of the nucleon with a pion.

In the relativistic formulation the time derivative of the nucleon field implies a factor $E \approx M_N$ comparable to the hard scale $\Lambda_\chi \approx 1$ GeV. Moreover, the nucleon mass does not vanish in the chiral limit. Such problems can be overcome if nucleons are treated as high massive static sources so that the momentum transfer due to pion exchange is very small compared to the nucleon mass. The Lagrangian can then be expanded in powers of the momentum transfer over the nucleon mass. This approach is known as Heavy Baryon Chiral Perturbation Theory (HBChPT) [65] and represents the non-relativistic limit of ChPT.

The basic idea is to decompose the nucleon four-momentum p_μ as

$$p_\mu = M_N v_\mu + k_\mu \tag{3.35}$$

with v_μ the nucleon four-velocity, satisfying $v^2 = 1$, and k_μ its small residual momentum, $v \cdot k \ll M_N$. We introduce the velocity-dependent spinor fields

$$N = e^{iM_N v\cdot x}P_v^+\psi \ , \qquad h = e^{iM_N v\cdot x}P_v^-\psi \ , \tag{3.36}$$

where the projectors $P_v^\pm$ are defined as:

$$P_v^+ = \frac{1 + \gamma^\mu v_\mu}{2} \ , \qquad P_v^- = \frac{1 - \gamma^\mu v_\mu}{2} \ . \tag{3.37}$$

For $v_\mu = (1, 0, 0, 0)$ (static limit), the fields N and h are respectively interpreted as the large/upper component and the small/lower component of the Dirac spinor field ψ. Rewriting the Lagrangian (3.30) in terms of the field N ($\bar{N} = N^\dagger$) we obtain:

$$\tilde{\mathcal{L}}_{\pi N}^{(1)} = \bar{N}\left(iD_0 - \frac{1}{2}g_A\vec{\sigma}\cdot\vec{u}\right)N \ . \tag{3.38}$$

The $1/M_N$ corrections give rise to a second-order Lagrangian:

$$\tilde{\mathcal{L}}_{\pi N, M_N}^{(2)} = \bar{N}\left[\frac{1}{2M_N}\vec{D}\cdot\vec{D} + i\frac{g_A}{4M_N}\{\vec{\sigma}\cdot\vec{D}, u_0\}\right]N \ . \tag{3.39}$$

The second-order Lagrangian is not complete. It receives a contribution from the correction of order $1/M_N$ to the first order Lagrangian, but still we can add combinations of operators O_i of the form $c_i\,\bar{\psi}\,O_i^{(2)}\psi$. The coefficients c_i are low-energy constants (LECs) determined by the fit to πN scattering data. They originate the following contribution to the second order Lagrangian:

$$\tilde{\mathcal{L}}^{(2)}_{\pi N,ct} = \bar{N}\left[2\,c_1\,m_\pi^2(U+U^\dagger) + \left(c_2 - \frac{g_A^2}{8\,M_N}\right)u_0^2 + c_3\,u_\mu u^\mu \right. \\ \left. + \frac{i}{2}\left(c_4 + \frac{1}{4\,M_N}\right)\vec{\sigma}\cdot(\vec{u}\times\vec{u})\right] + \dots\ , \quad (3.40)$$

neglecting the isospin-breaking c_5-term.

3.2.3 Nucleon-Nucleon Lagrangian

The short-distance dynamics is integrated out by the description in terms of low-energy degrees of freedom. Nevertheless they are, although unresolved, still essential to get a complete description of nuclear forces. Chiral pion dynamics reproduces the long and intermediate range parts of the NN interaction. These long range pieces dominate the higher partial waves, but NN observables at low energy depend largely on the contribution of the lower partial waves with $L \leq 2$. The lower partial waves are governed by short-distance. We need to set contact terms to account for them.

Due to parity conservation, only even powers of derivates can appear in the contact Lagrangian:

$$\tilde{\mathcal{L}}_{NN} = \tilde{\mathcal{L}}^{(0)}_{NN} + \tilde{\mathcal{L}}^{(2)}_{NN} + \tilde{\mathcal{L}}^{(4)}_{NN} + \cdots \quad (3.41)$$

The lowest order term reads [66]:

$$\tilde{\mathcal{L}}^{(0)}_{NN} = -\frac{1}{2}\,C_S\,\bar{N}N\bar{N}N - \frac{1}{2}\,C_T\,(\bar{N}\vec{\sigma}N)\cdot(\bar{N}\vec{\sigma}N)\ , \quad (3.42)$$

where C_S and C_T are constants determined by the fit to NN scattering data.

3.3 Power Counting

The Feynman diagrams that can be calculated from the effective Lagrangian are infinite in number. To be of some practical use, we need criteria for an ordering scheme that enables to distinguish between large and small contributions.

In ChPT, each diagram gives a contribution of the form $(Q/\Lambda_\chi)^\nu$, and we would like to determine the power ν, also called *chiral order*.

Without going into details, the following power counting rule results [56, 67–69]:

$$\nu = 2A - 2 - 2C + 2L + \sum_i \Delta_i\ , \quad (3.43)$$

with

$$\Delta_i \equiv d_i + \frac{n_i}{2} - 2. \quad (3.44)$$

A is the number of nucleons involved, C is the number of separately connected pieces and L the number of loops. Δ_i is the interaction index of the vertex i, with d_i the number of derivatives or pion mass insertions and n_i the number of nucleons involved in vertex i. Note $\Delta_i \geq 0$.

In any case, the most important aspect of such formula is that the chiral power ν is bounded from below, $\nu \geq 0$, so that an expansion in powers of the small momentum Q is convergent.

In the case of two interacting nucleons, $A = 2$ and the formula for the chiral order reduces to

$$\nu = 2L + \sum_i \Delta_i \ . \tag{3.45}$$

For the evaluation of the chiral order of the Feynman diagrams, it is useful to rearrange the heavy baryon Lagrangian in terms of increasing interaction index Δ. We show the first orders [56]:

$$\begin{aligned}
\tilde{\mathcal{L}}^{\Delta=0} &= \frac{1}{2}\partial_\mu \boldsymbol{\pi}\cdot\partial^\mu\boldsymbol{\pi} - \frac{1}{2}m_\pi^2\boldsymbol{\pi}^2 + \frac{1-4\alpha}{2f_\pi^2}(\boldsymbol{\pi}\cdot\partial_\mu\boldsymbol{\pi})(\boldsymbol{\pi}\cdot\partial^\mu\boldsymbol{\pi}) - \frac{\alpha}{f_\pi^2}\boldsymbol{\pi}^2\partial_\mu\boldsymbol{\pi}\cdot\partial^\mu\boldsymbol{\pi} + \frac{8\alpha-1}{8f_\pi^2}m_\pi^2\boldsymbol{\pi}^4 \\
&+\bar{N}\left[i\partial_0 - \frac{g_A}{2f_\pi}\boldsymbol{\tau}\cdot(\vec{\sigma}\cdot\vec{\nabla})\boldsymbol{\pi} - \frac{1}{4f_\pi^2}\boldsymbol{\tau}\cdot(\boldsymbol{\pi}\times\partial_0\boldsymbol{\pi})\right]N \\
&+\bar{N}\left\{\frac{g_A(4\alpha-1)}{4f_\pi^3}(\boldsymbol{\tau}\cdot\boldsymbol{\pi})\left[\boldsymbol{\pi}\cdot(\vec{\sigma}\cdot\vec{\nabla})\boldsymbol{\pi}\right] + \frac{g_A\alpha}{2f_\pi^3}\boldsymbol{\pi}^2\left[\boldsymbol{\tau}\cdot(\vec{\sigma}\cdot\vec{\nabla})\boldsymbol{\pi}\right]\right\}N \\
&-\frac{1}{2}C_S\bar{N}N\bar{N}N - \frac{1}{2}C_T(\bar{N}\vec{\sigma}N)\cdot(\bar{N}\vec{\sigma}N) + \dots \ ,
\end{aligned} \tag{3.46}$$

$$\begin{aligned}
\tilde{\mathcal{L}}^{\Delta=1} &= \bar{N}\left\{\frac{\vec{\nabla}^2}{2M_N} - \frac{i\,g_A}{4M_Nf_\pi}\boldsymbol{\tau}\cdot\left[\vec{\sigma}\cdot\left(\overleftarrow{\nabla}\partial_0\boldsymbol{\pi} - \partial_0\boldsymbol{\pi}\overrightarrow{\nabla}\right)\right]\right. \\
&\left.-\frac{i}{8M_Nf_\pi^2}\boldsymbol{\tau}\cdot\left[\overleftarrow{\nabla}\cdot(\boldsymbol{\pi}\times\vec{\nabla}\boldsymbol{\pi}) - (\boldsymbol{\pi}\times\vec{\nabla}\boldsymbol{\pi})\cdot\overrightarrow{\nabla}\right]\right\}N \\
&+\bar{N}\left[4\,c_1m_\pi^2 - \frac{2\,c_1}{f_\pi^2}m_\pi^2\boldsymbol{\pi}^2 + \left(c_2 - \frac{g_A^2}{8M_N}\right)\frac{1}{f_\pi^2}(\partial_0\boldsymbol{\pi}\cdot\partial_0\boldsymbol{\pi})\right. \\
&\left.+\frac{c_3}{f_\pi^2}(\partial_\mu\boldsymbol{\pi}\cdot\partial^\mu\boldsymbol{\pi}) - \left(c_4 + \frac{1}{4M_N}\right)\frac{1}{2f_\pi^2}\epsilon^{ijk}\epsilon^{abc}\sigma^i\tau^a(\partial^j\pi^b)(\partial^k\pi^c)\right]N \\
&-\frac{D}{4f_\pi}(\bar{N}N)\bar{N}\left[\boldsymbol{\tau}\cdot(\vec{\sigma}\cdot\vec{\nabla})\boldsymbol{\pi}\right]N - \frac{1}{2}E(\bar{N}N)(\bar{N}\boldsymbol{\tau}N)\cdot(\bar{N}\boldsymbol{\tau}N) + \dots \ ,
\end{aligned} \tag{3.47}$$

$$\tilde{\mathcal{L}}^{\Delta=2} = \mathcal{L}^{(4)}_{\pi\pi} + \tilde{\mathcal{L}}^{(3)}_{\pi N} + \tilde{\mathcal{L}}^{(2)}_{NN} + \dots \ , \tag{3.48}$$

$$\tilde{\mathcal{L}}^{\Delta=4} = \tilde{\mathcal{L}}^{(4)}_{NN} + \dots \ , \tag{3.49}$$

neglecting terms that are not relevant for nuclear forces up to $\nu = 4$. The terms with coefficients D and E are, respectively, a πNN-contact term and a NNN-contact term. Note that all the constants appearing in the Lagrangian are taken in the chiral limit.

We are now able to construct the scattering diagrams for each chiral order in a controlled way. In Fig. 3.1 we report a list of such diagrams organized according to their chiral order.

At leading order LO ($\nu = 0$) only the terms of the Lagrangian with interaction index $\Delta = 0$ (eq. (3.46)) contribute. They generate a NN contact interaction (with coefficient C_S and C_T) and the well known static 1π-exchange, which introduces the tensor force and reproduces the peripheral partial waves ($L \geqslant 2$). As concerns the two contact terms, they contribute only in S-waves.

The order $\nu = 1$ is forbidden by parity and time-reversal invariance.

The next-to-leading contribution (NLO) comes at order $\nu = 2$. Eq. (3.45) guides us in the construction of the diagrams. One-loop diagrams are allowed in combination with $\Delta = 0$ interaction vertices. Therefore we can include at this order 2π-exchange diagrams

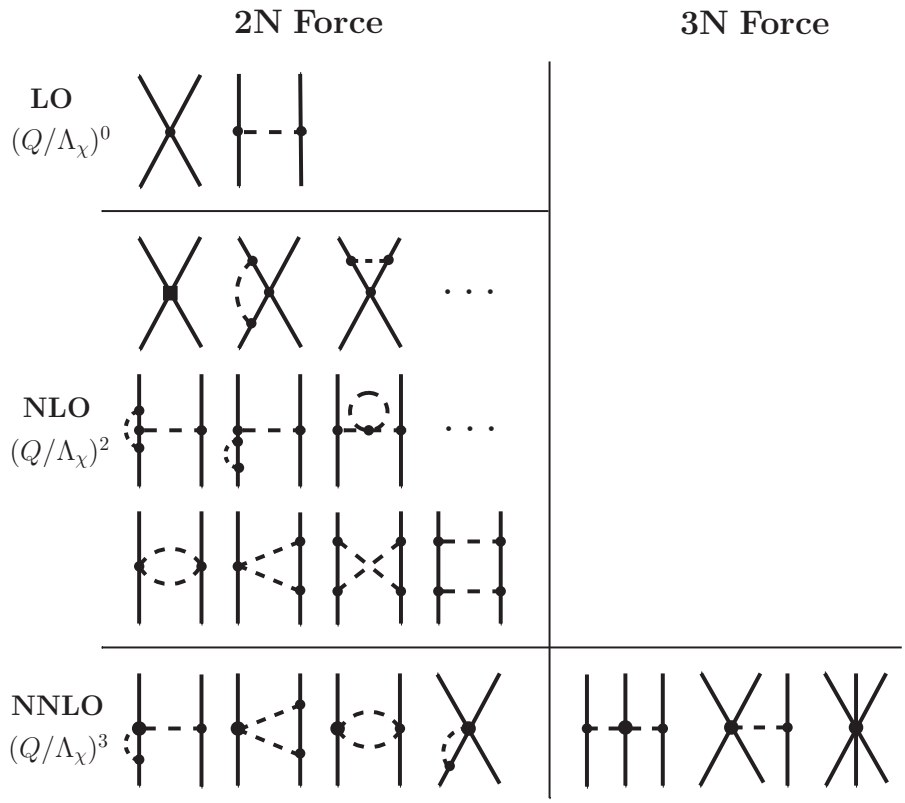

Figure 3.1: NN scattering diagrams organized according their contribution in powers of Q/Λ_χ. The small dot indicates a vertex with $\Delta = 0$, the solid square a vertex with $\Delta = 1$ and the large dot a vertex with $\Delta = 2$.

with πNN (axial) and $\pi\pi NN$ (Weinberg-Tomozawa) vertices. We can also consider the combination $L = 0$ and $\Delta = 2$ and use the seven contact terms of $\mathcal{O}(Q^2)$ in the Lagrangian $\tilde{\mathcal{L}}^{(2)}_{NN}$. They are indicated with a solid square to distinguish them from the lower order contact terms labeled with a small dot. They contribute in S and P waves. The structure of the short- and intermediate-range parts of the NN interaction is well reproduced.

At next-to-next-to-leading order (NNLO) ($\nu = 3$), the contributions come from one-loop diagrams with an insertion of a $\pi\pi NN$ contact-vertex with $\Delta = 1$ proportional to c_i. These contact terms include the correlated 2π-exchange as well as intermediate Δ-isobar contributions. Note that also the first relativistic corrections of $\mathcal{O}(1/M_N)$ come at this order.

Three-body diagrams appear at NLO, but it has been shown that they cancel each other at this order. So the first contribution from 3-body forces takes place at NNLO.

3.4 Nucleon-Nucleon Interaction at One Loop

The NN interaction in the framework of ChPT has been calculated in Refs. [51, 52]. The calculation is performed in the center of mass frame:

$$N(\vec{p}) + N(-\vec{p}) \longrightarrow N(\vec{p}\,') + N(-\vec{p}\,') \ , \tag{3.50}$$

with $p = |\vec{p}| = |\vec{p}\,'|$. The results are given in terms of contribution to the elastic NN $\mathcal{T}$-matrix in momentum space, whose general structure is written as:

$$\begin{aligned}\mathcal{T}_{NN} &= V_C + W_C\,\boldsymbol{\tau}_1\cdot\boldsymbol{\tau}_2 + [V_S + W_S\,\boldsymbol{\tau}_1\cdot\boldsymbol{\tau}_2]\,\vec{\sigma}_1\cdot\vec{\sigma}_2 + [V_T + W_T\,\boldsymbol{\tau}_1\cdot\boldsymbol{\tau}_2]\,(\vec{\sigma}_1\cdot\vec{q})(\vec{\sigma}_2\cdot\vec{q}) \\ &\quad + [V_{SO} + W_{SO}\,\boldsymbol{\tau}_1\cdot\boldsymbol{\tau}_2]\,i\,(\vec{\sigma}_1+\vec{\sigma}_2)\cdot(\vec{q}\times\vec{p}) \\ &\quad + [V_Q + W_Q\,\boldsymbol{\tau}_1\cdot\boldsymbol{\tau}_2]\,[\vec{\sigma}_1\cdot(\vec{q}\times\vec{p})][\vec{\sigma}_2\cdot(\vec{q}\times\vec{p})]\;, \end{aligned} \tag{3.51}$$

where $\vec{q} = \vec{p}\,' - \vec{p}$ is the momentum transfer with $q = |\vec{q}| = p\sqrt{2(1-z)}$ ($z = \cos\theta$, with θ the scattering angle). The ten complex functions V and W depend on p and z.

We adopt such form of the NN $\mathcal{T}$-matrix in the present manuscript. Whenever results for the functions V and W are given, it is implied that they refer to the form of the $\mathcal{T}$-matrix in eq. (3.51).

3.4.1 Pion-Exchange Dynamics

The pion-exchange contributions to NN scattering have been calculated in Ref. [51] up to one-loop order and at NNLO. In the following, we briefly discuss this approach.

At LO we have the usual static 1π-exchange described by the second diagram in Fig. 3.1. At NLO the diagrams involved are those in the third row in Fig. 3.1: they just renormalize the nucleon and pion mass and the axial coupling constant to their physical values [51]. The renormalizations of f_π, g_A, M_N and m_π are taken into account by working with their physical values.

The contributions from 2π-exchange are more involved and need to be treated carefully. In Ref. [51] the covariant relativistic Lagrangian Eq. (3.34) is used as starting point. The resulting transition matrix element is expanded in powers of $1/M_N$ and only afterwards the loop integral is solved and treated by means of dimensional regularization. The result is of course the same of that obtained in HBChPT, but as regards the planar box diagram it avoids the problem of the Pinch singularity that affects the HBChPT approach. Such singularity in the loop integral originates from taking the limit $M_N \to \infty$ from the beginning. In a perturbative expansion in $1/M_N$ the nucleon mass is finite and the box diagram is well defined. The calculation of the box diagram produces a term proportional to M_N and a term of order zero in M_N (neglecting the small relativistic corrections). The term proportional to M_N corresponds to the iterated 1π-exchange which is usually generated by the non-relativistic Lippmann-Schwinger equation. This term is infinite in the heavy baryon limit. The other term, not depending on the nucleon mass, corresponds to the irreducible part of the 2π-exchange and causes no problem in the heavy baryon limit. The detailed calculation of the 2π-exchange diagrams can be found in Ref. [56].

3.4.2 Explicit Inclusion of the Δ-Isobar Excitation

The $\Delta(1232)$-isobar is the lowest excited state of the nucleon. It is a πN resonance with both spin and isospin $3/2$ and excitation energy $\Delta = 293$ MeV. It gives an important contribution to the attractive intermediate-range NN interaction.

Given that $\Delta \simeq 2m_\pi \ll \Lambda_\chi$, it is useful to treat the Δ-isobar as an explicit degree of freedom. In this case Δ is treated as a small parameter together with the pion mass and external momenta. This scheme is called *small scale expansion* [70].

We report the leading-order Lagrangian involving the $\Delta(1232)$ in the heavy baryon formalism:

$$\tilde{\mathcal{L}}^{(\Delta=0)}_{\mathcal{D}} = \bar{\mathcal{D}}(i\partial_0 - \Delta)\mathcal{D} - \frac{3\,g_A}{2\sqrt{2}f_\pi}\left(\bar{N}\mathbf{T}\vec{S}\,\mathcal{D} + \text{h.c.}\right)\cdot\vec{\nabla}\boldsymbol{\pi} - D_T\,\bar{N}\boldsymbol{\tau}\vec{\sigma}N\cdot(\bar{N}\boldsymbol{\tau}\vec{S}\,\mathcal{D} + h.c.)\;, \tag{3.52}$$

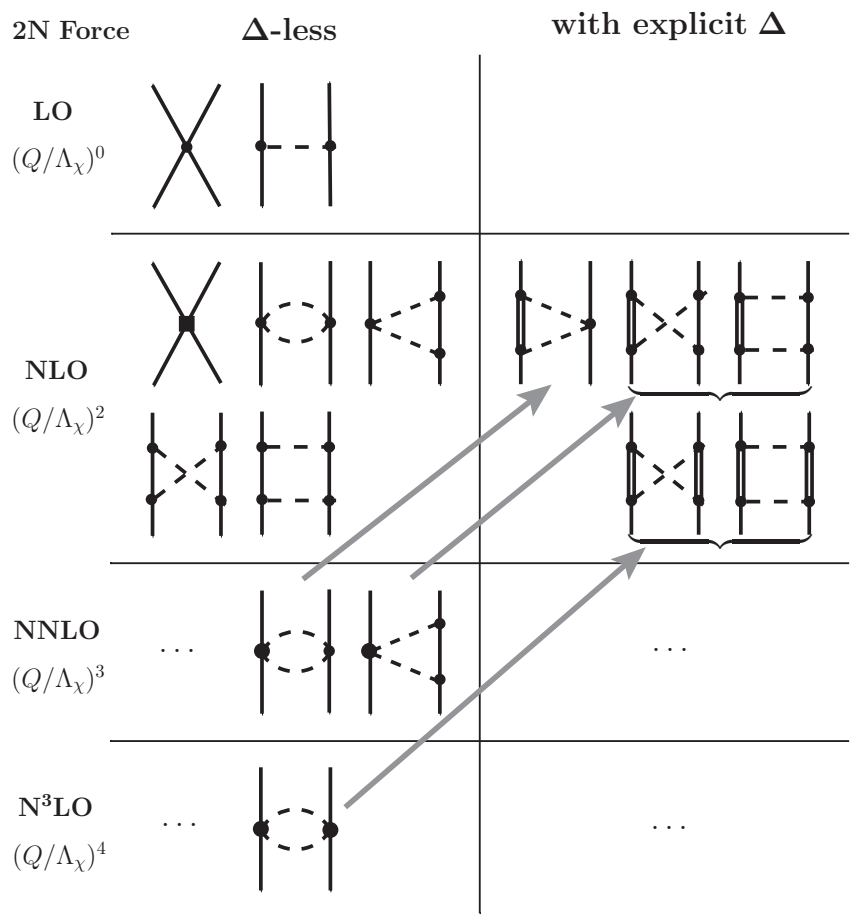

Figure 3.2: Chiral NN interaction diagrams without (left) and with (right) explicit inclusion of the Δ-isobar excitation. A large amount of the c_i-contact terms strength is taken out by the Δ-isobar intermediate state (indicated by a double line), which increases the chiral power by one unit, as pointed out by the arrows.

where $\mathcal{D}$ is a four-spinor field representing the Δ-isobar and D_T a low energy constant. This Lagrangian gives rise to a $N\pi\Delta$-isobar vertex and to a $NNN\Delta$-isobar contact interaction. The spin 1/2 to spin 3/2 transition operators S^i $(i = 1, 2, 3)$ are 2×4 spin matrices satisfying $S^i S^{j\dagger} = (2\delta^{ij} - i\epsilon^{ijk}\sigma^k)/3$. The same property is valid for the isospin 1/2 to isospin 3/2 transition matrices T^a: $T^a T^{b\dagger} = (2\delta^{ab} - i\epsilon^{abc}\tau^c)/3$.

In the Δ-less theory the effects of the Δ-isobar are implicitly taken into account through the low-energy constants c_i. The resonance contributes significantly to these coefficients [71]. Explicit inclusion of the Δ-isobar reduces the magnitude of some of the c_i, improving the convergence of the perturbative expansion. For instance, while in the Δ-less theory the values of c_3 and c_4 are between 3 and 5 GeV^{-1} in modulo, resulting from the fit to the πN scattering data, for the theory with the Δ-isobar they decrease to around 1 GeV^{-1}.

In Fig. 3.2, we display the additional diagrams contributing to the NN force when the Δ-isobar degree of freedom is included. In comparison to the c_i contact vertex, the explicit insertion of a Δ-isobar intermediate state increases the chiral power by one unit.

2π-exchange diagrams with Δ-isobar at NLO have been evaluated in covariant perturbation theory in Ref. [52]. For instance, the analytical form of the attractive isoscalar central potential from diagrams with single Δ-isobar excitation is

$$V_C^{(N\Delta)}(r) = -\frac{3\,g_A^4}{64\pi^2 f_\pi^4 \Delta}\frac{e^{-2x}}{r^6}(6 + 12\,x + 10\,x^2 + 4\,x^3 + x^4)\ , \tag{3.53}$$

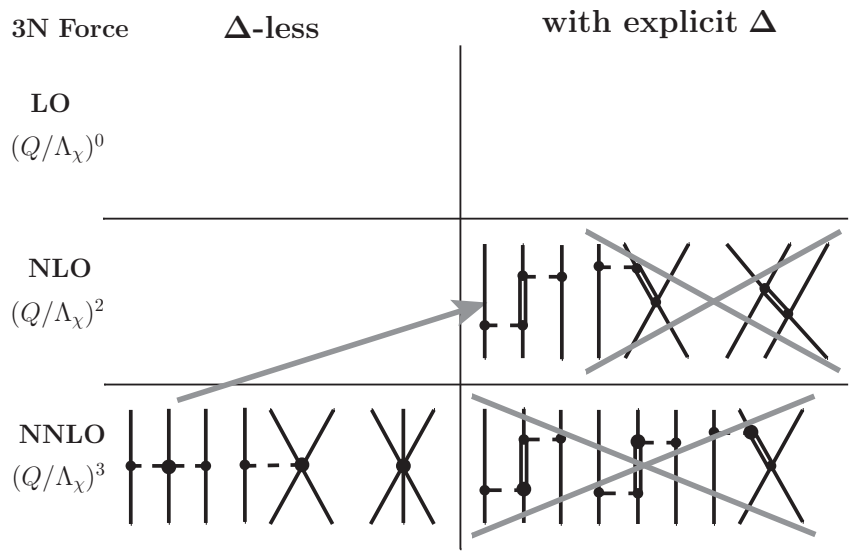

Figure 3.3: Chiral $3N$ interaction diagrams without (left) and with (right) explicit inclusion of the Δ-isobar excitation. Diagrams with Δ-isobar start to contribute already at NLO. The two diagrams at NLO cancel after antisymmetrization. The three diagrams at NNLO are suppressed because the subleading $N\Delta\pi$ vertex involves a time derivative [72].

with $x = m_\pi r$. It agrees almost perfectly with the phenomenological σ-exchange model at distances $r > 2$ fm and is reminiscent of the Van der Waals interaction, which fully emerges in the chiral limit ($x = 0$).

In Fig. 3.3 we show the contributions to the $3N$ force. Note that $3N$ diagrams appear already at NLO when the Δ-isobar is included. Only one of the three diagrams at NLO remains. The other two diagrams cancel after antisymmetrization [72]. Diagrams at NNLO are suppressed in the chiral counting [72].

3.5 In-Medium Chiral Perturbation Theory

In the last two decades a novel approach to the nuclear many-body problem has been developed, based on the understanding of the NN interaction in the framework of chiral effective field theories [53–55]. The basic assumption of this approach is the scale separation between the short-range physics and the long- and intermediate-distance dynamics. While the latter, described primarily by pion dynamics in the presence of the nuclear medium, are treated explicitly, the unresolved short-distance physics is encoded in a few contact terms with coefficients fixed in order to reproduce selected known bulk properties of nuclear matter. Many other ground state and single-particle properties and nuclear thermodynamics emerge as predictions.

In the following we consider the case of isospin-symmetric nuclear matter at temperature zero, that is nuclear natter composed of an equal amount of protons and neutrons. Their Fermi seas are identical as well as their Fermi momenta. Isospin-symmetric nuclear matter is the simplest case because protons and neutrons can be treated indifferently as isospin-doublet nucleons in performing calculations. The generalization to arbitrary isospin-asymmetry and extension to finite temperature are the topics of the next chapter.

3.5.1 Small Scales in Nuclear Matter

The relevant active degrees of freedom for the description of the nuclear many-body problem are nucleons and pions. In-medium ChPT is applicable to nuclear many-body

systems as long as the Fermi momentum k_F is small compared to the scale of spontaneous chiral symmetry breaking in QCD, $\Lambda_\chi \sim 4\pi f_\pi \sim 1$ GeV.

The characteristic range of nuclear momenta is comparable to about twice the pion mass ($k_{F0} \approx 2\, m_\pi$, where $k_{F0} \simeq 263$ MeV is the Fermi momentum at the saturation density of nuclear matter, $\rho_0 \simeq 0.16\,\mathrm{fm}^{-3}$). This implies that 1π- and 2π-exchange processes have to be treated explicitly in the presence of the nuclear medium. Moreover, to complete the picture it is mandatory to include the $\Delta(1232)$-isobar excitation as an explicit degree of freedom, as mentioned before, because the splitting between the Δ-isobar mass and the nucleon mass, $\Delta = 293$ MeV, is again comparable to $2\, m_\pi$. Consequently, the "small scales" that appear in our scheme are the Fermi momentum of the nucleons, k_F, the pion mass, m_π, and the $\Delta(1232)$-nucleon mass splitting Δ.

3.5.2 In-Medium Nucleon Propagator

The basic ingredient in performing calculations at finite baryon density is the *in-medium nucleon propagator*.

At finite density, the ground state of a fermionic system is the filled Fermi sea $|\phi_0\rangle$. At $T = 0$, all momentum levels up to the Fermi momentum k_F are occupied. For momenta below k_F, one can only annihilate a particle of the Fermi sea or, equivalently, create a hole. The creation of a particle with momentum smaller than k_F is forbidden by the saturation of the energy levels. There is no such restriction for creating a particle above the Fermi sea.

The Fermi momentum k_F is related to the density ρ through the relation

$$\rho = g \int_0^\infty \frac{\mathrm{d}^3 p}{(2\pi)^3}\, \theta(k_F - |\vec{p}\,|) = g\, \frac{k_F^3}{6\,\pi^2}\ , \tag{3.54}$$

with g the degeneracy factor ($g = 4$ for symmetric nuclear matter).

The definition of the nucleon propagator must now be modified in the medium in comparison with the vacuum case:

$$S_{F0}(x-y) = \langle 0|\, T[\Psi(x)\bar{\Psi}(y)]\, |0\rangle \longrightarrow S_F(x-y) = \langle \phi_0|\, T[\Psi(x)\bar{\Psi}(y)]\, |\phi_0\rangle\ , \tag{3.55}$$

with T the time-ordering operator. The detailed derivation of the in-medium propagator can be found in Appendix A.1. The in-medium nucleon propagator in momentum space results:

$$S_N(p) = (\not{p} + M_N)\left[\frac{i}{p^2 - M_N^2 + i\epsilon} - 2\pi\delta(p^2 - M_N^2)\,\theta(k_F - |\vec{p}\,|)\,\theta(p_0)\right]\ , \tag{3.56}$$

with $p^\mu = (p_0, \vec{p}\,)$, and $M_N = 939$ MeV is the free nucleon mass. The propagator consists of two terms. The first term is the vacuum nucleon propagator. The second term is the modification coming from the presence of the medium and is called *medium insertion*. It originates from the Pauli blocking effects in dense matter. The contributions to the energy density are then organized according to the number of medium insertions.

3.5.3 Low-momentum Expansion of the Energy Density

The observable we are interested in is the energy per particle $\bar{E}$ as a function of the nucleon density ρ. For symmetric nuclear matter the degeneracy factor is $g = 4$, a factor 2 coming from the spin degeneracy, the other factor 2 coming from the isospin degeneracy.

The energy density of the system is given by the sum of all connected linked Feynman diagrams, i.e. the vacuum or bubble diagrams [74, 75]. They are obtained closing the legs of the diagrams in Fig. 3.2 in all possible ways and respecting the direction of the arrows. The

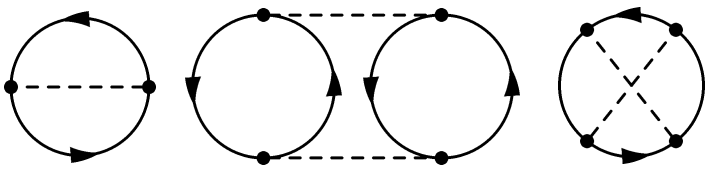

(a) (b) (c)

Figure 3.4: (a): 1π-exchange Fock diagram; (b): iterated 1π-exchange Hartree diagram; (c): iterated 1π-exchange Fock diagram. Diagram (a) includes two medium insertions, diagrams (b) and (c) involve two and three medium insertions. The combinatoric factors are respectively 1/2, 1/4, 1/4.

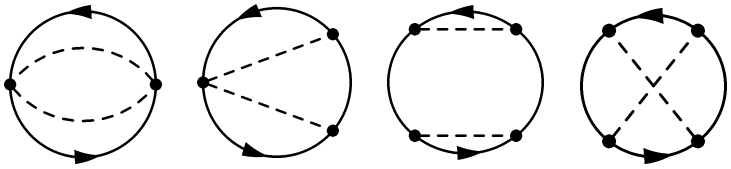

Figure 3.5: Irreducible 2π-exchange diagrams to be evaluated with two medium insertions. Diagrams with three medium insertions contribute only at $\mathcal{O}(k_F^6)$. The combinatoric factors are respectively 1/4, 1, 1/2, 1/4.

calculation is performed up to NLO and at three-loop order. Some of the vacuum diagrams that contribute to the energy density are showed in Figs. 3.4 and 3.5.

The interaction vertices that are relevant for the vacuum diagrams in the present calculation are the pseudo-vector $NN\pi$ vertex and the Weinberg-Tomozawa $NN\pi\pi$-contact vertex, both coming from the interaction Lagrangian eq. (3.34), and the $N\pi\Delta$-isobar vertex from the Lagrangian (3.52):

$$\frac{g_A}{2f_\pi}\,\not{q}_a\gamma_5\,\tau_a\ , \qquad \frac{1}{4f_\pi^2}\,\epsilon_{abc}\,(\not{q}_b-\not{q}_a)\,\tau_c\ , \qquad -\frac{3g_A}{2\sqrt{2}f_\pi}\,\vec{S}\cdot\vec{q}_a\,T_a\ . \tag{3.57}$$

The convention for the pion momenta is that $q_{a,b}$ are outgoing. The values of the constant used are $f_\pi = 92.4$ MeV and $g_A = 1.37$ [54].

The use of the in-medium nucleon propagator Eq. (3.56) to evaluate ground state expectation values of the energy per particle generates diagrams with different numbers of medium insertions. Diagrams with no medium insertion give an unobservable shift of the vacuum energy. Diagrams with one medium insertion renormalize the nucleon mass to its physical value and provide a description at the level of the (non-interacting) Fermi gas. The interesting many-body effects originate from diagrams with two and three medium insertions. Two-body terms are directly related to the NN $\mathcal{T}$-matrix and are generated from diagrams with two medium insertions. Diagrams with three medium insertions generate the important three-body terms, such as the Pauli-blocking effects on the two-body terms. Diagrams with four medium insertions are imaginary and cancels the imaginary part of the diagrams with two and three medium insertions, so that the energy is real. Convergence in the series of medium insertions, or powers of k_F, at the three-loop level is realized for $k_F \ll \Lambda_\chi \sim 1$ GeV as long as four-nucleon correlations are not prominent. Effects of four-body correlations are still an open issue and subjects of ongoing investigations [73, 76].

The energy per particle at $T = 0$ is then derived as an expansion in powers of k_F:

$$\bar{E}(\rho) = \sum_n F_n\left(\frac{k_F}{m_\pi}, \frac{m_\pi}{\Delta}\right)\, k_F^n\ . \tag{3.58}$$

The coefficients F_n of the expansion are non-trivial functions of the dimensionless ratios k_F/m_π and m_π/Δ. The energy per particle of nuclear matter is calculated up to and including $\mathcal{O}(k_F^5)$.

Fig. 3.4a shows the 1π-exchange Fock diagram. The corresponding Hartree diagram is trivially null, because the exchanged momentum appearing in the spin trace is $q_\mu = 0$. Figs. 3.4b and 3.4c display respectively the iterated 1π-exchange Hartree- and Fock-diagrams. We recall that the meaning of "iterated" and "irreducible" diagrams has been discussed in section 3.4.1. In particular, the iterated 1π-exchange diagrams 3.4b and 3.4c are proportional to the nucleon mass, so that their contribution is generally large. Such diagrams are taken with two and three medium insertions.

The next set in Fig. 3.5 contains the irreducible 2π-exchange Fock-diagrams, to be considered with two medium insertions. Diagrams with three medium insertions give a contribution to the energy density of order $\mathcal{O}(k_F^6)$. In the case of isospin-symmetric nuclear matter, the contribution of the corresponding Hartree diagrams with two medium insertions vanishes. This can be easily seen considering the isospin-trace of the general form of the NN $\mathcal{T}$-matrix (Eq. (3.51)).

The irreducible 2π-exchange diagrams with single and double Δ-isobar excitation as intermediate state, arising from the scattering diagrams depicted in Fig. 3.2, are also included.

For the treatment of the irreducible 2π-exchange vacuum diagrams with two medium insertions a twice-subtracted dispersion relation is used [77]. It is worth to spend some words to describe this method.

The NN transition matrix can be represented in the form of a dispersion relation:

$$\mathrm{Re}\mathcal{T}(\omega) = \frac{1}{\pi}\int_{4m_\pi^2}^{\infty} \mathrm{d}\omega' \, \frac{\mathrm{Im}\mathcal{T}(\omega')}{\omega' - \omega} \ . \tag{3.59}$$

The integration runs over the brunch-cut of the $\mathcal{T}$-matrix starting at the two-pion state and propagating to infinity. We set $\omega' = \mu^2$ and limit $\mathcal{T}$ to the physical domain imposing that ω be space-like, $\omega = -q^2 = -|\vec{q}\,|^2 < 0$, with $\vec{q}$ the momentum transfer in scattering process. The integral becomes:

$$\mathrm{Re}\mathcal{T}(q) = \frac{2}{\pi}\int_{2m_\pi}^{\infty} \mathrm{d}\mu \, \frac{\mu}{\mu^2 + q^2} \, \mathrm{Im}\mathcal{T}(i\mu) \ . \tag{3.60}$$

Under the integral, $\mathcal{T}$ is a function of $i\mu$ and not of μ in order to preserve the singularity at the denominator. The integral is ultraviolet divergent and its regularization requires two subtractions:

$$\frac{\mu}{\mu^2 + q^2} \longrightarrow \frac{\mu}{\mu^4(\mu^2 + q^2)} \ , \tag{3.61}$$

or, in a more suitable form,

$$\frac{\mu}{\mu^2 + q^2} = \frac{1}{\mu} - \frac{q^2}{\mu^3} + \frac{q^4}{\mu^3(\mu^2 + q^2)} \ . \tag{3.62}$$

After the integration, we get two subtraction constants:

$$\mathrm{Re}\mathcal{T}(q) = \mathrm{Re}\mathcal{T}(0) + \frac{q^2}{2}\mathrm{Re}\mathcal{T}''(0) + \frac{2}{\pi}\int_{2m_\pi}^{\infty} \mathrm{d}\mu \, \frac{q^4}{\mu^3(\mu^2 + q^2)} \, \mathrm{Im}\mathcal{T}(i\mu) \ , \tag{3.63}$$

where the derivative is taken with respect to q. The energy density is then obtained integrating over the two Fermi spheres in momentum space. The subtraction constants give rise to a contribution to the energy per particle proportional to k_F^3 and k_F^5, respectively. They can be considered as two contact terms that encode the unresolved short-distance part of

the 2π-exchange dynamics. In general, we can introduce two contact terms subsuming the contributions from unresolved short-distance physics,

$$\bar{E}(k_F)^{(ct)} = B_3 \frac{k_F^3}{M_N^2} + B_5 \frac{k_F^5}{M_N^4} \ , \tag{3.64}$$

whose dimensionless coefficients B_3 and B_5 can be tuned to some selected properties of nuclear matter. Note that the two contact terms are equivalent to the contribution of two S-wave (one of which q^2-dependent) contact interactions. As concerns the long-range part of the irreducible 2π-exchange, its contribution to the energy per particle of symmetric nuclear matter is:

$$\bar{E}(k_F)^{(irrF)} = \int\limits_{|p_1,p_2|<k_F} \frac{\mathrm{d}^3p_1}{(2\pi)^3}\frac{\mathrm{d}^3p_2}{(2\pi)^3}\int_{2m_\pi}^{\infty}\mathrm{d}\mu\,\frac{q^4}{\mu^3(\mu^2+q^2)}\,\mathrm{Im}(V_C+3W_C+2\mu^2V_T+6\mu^2W_T) \ , \tag{3.65}$$

where the spectral functions V_C, W_C, V_T and W_T are calculated in Refs. [51, 52] and reported in Appendix B.1.

The Hartree diagrams related to the irreducible 2π-exchange with Δ-isobar excitation give a contribution proportional to k_F^3 or, equivalently, to the density ρ, and it is absorbed in the B_3 contact term.

For a good description of nuclear matter properties an additional three-nucleon contact interaction, controlled by the parameter ζ, is required [55]. It is introduced to counteract the strongly-repulsive ρ^2-term arising from the three-body Hartree contribution to the irreducible 2π-exchange with Δ-isobar excitation. Imposing only the minimum of the energy curve to be -16 MeV, the optimal set of values for the coefficients of the contact terms has been found to be $B_3 = -7.99$, $B_5 = 0$, $\zeta = -3/4$ [55]. For instance, with such a parameter set, the predicted saturation density is $\rho_0 \simeq 0.157\,\mathrm{fm}^{-3}$ and the compressibility of nuclear matter at the saturation point results $K \simeq 300$ MeV.

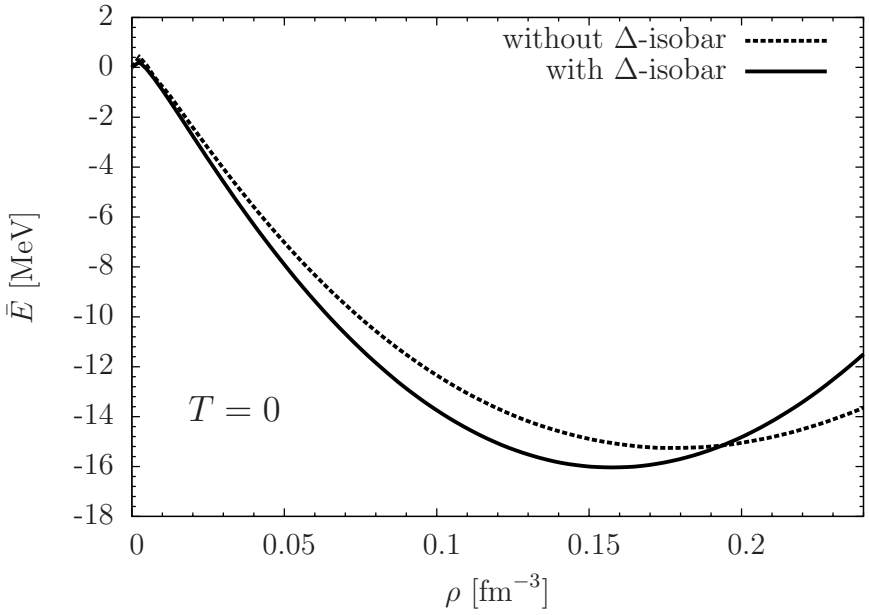

Figure 3.6: Energy per particle of isospin-symmetric nuclear matter as a function of the nucleon density. The dashed line shows the equation of state obtained without the inclusion of the Δ-isobar excitation as an explicit degree of freedom [54], the solid line displays the equation of state obtained including the Δ-isobar [55].

We conclude the present chapter showing the resulting equation of state of isospin-symmetric nuclear matter at $T = 0$. In Fig. 3.6 the energy per particle is plotted as a function of the nucleon density ρ. The dashed line shows the equation of state without the inclusion of the Δ-isobar excitation [54], the solid line displays the equation of state with the inclusion of the Δ-isobar excitation as an explicit degree of freedom [55]. One can note how the inclusion of the Δ-isobar shifts the saturation point to a more realistic density.

Chapter 4

Chiral Thermodynamics of Nuclear Matter

In this chapter we extend the in-medium Chiral Perturbation Theory approach to nuclear matter at finite temperature with arbitrary isospin-asymmetry. A systematic investigation of the thermodynamic properties of the resulting equations of state and their isospin dependence is performed [76].

4.1 Thermodynamic Potentials

The thermodynamic potentials that are relevant for our work are the Helmoltz free energy $F(T, V, N)$ and the thermodynamic grand-potential $\Omega(T, V, \mu)$.

The differential form of the free energy is

$$\mathrm{d}F = -S\,\mathrm{d}T - P\,\mathrm{d}V + \mu\,\mathrm{d}N \ , \tag{4.1}$$

with the chemical potential μ given by

$$\mu = \left.\frac{\partial F}{\partial N}\right|_{T,V} \ . \tag{4.2}$$

Concerning the grand-potential, its differential form is

$$\mathrm{d}\Omega = -S\,\mathrm{d}T - P\,\mathrm{d}V - N\,\mathrm{d}\mu \ , \tag{4.3}$$

where the number of particles is given by

$$N = -\left.\frac{\partial \Omega}{\partial \mu}\right|_{T,V} \ . \tag{4.4}$$

The two potentials are connected by the following relation:

$$F = E - TS = \Omega + \mu N \ . \tag{4.5}$$

4.2 Linked Cluster Expansion at Finite Temperature

In the grand-canonical ensemble the partition function and the thermodynamic potential are defined through:

$$Z = e^{-\beta\Omega} = \mathrm{Tr}\left\{e^{-\beta\hat{K}}\right\} = \mathrm{Tr}\left\{e^{-\beta\hat{K}_0}\hat{\mathcal{S}}(\beta)\right\} \ , \tag{4.6}$$

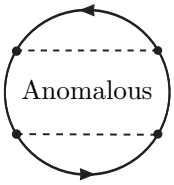

Figure 4.1: Anomalous Fock diagram with combinatoric factor 1/2.

with $\beta = 1/T$ and the operator $\hat{K}$ given by

$$\hat{K} = \hat{H} - \mu\hat{N} = \hat{K}_0 + \hat{V} = (\hat{H}_0 - \mu\hat{N}) + \hat{V} \ . \tag{4.7}$$

$\hat{\mathcal{S}}(\beta)$ is the finite-temperature $\mathcal{S}$-Matrix, i.e. the evolution operator of the interacting system.

The thermodynamic potential is the summation of all different, connected diagrams without external lines [75]:

$$\Omega = \Omega_0 + \sum_n \Omega_n \ , \tag{4.8}$$

with Ω_0 the potential of the non-interacting Fermi gas and Ω_n the contribution of the diagrams of order n in the quantity in which one expands.

The diagrams that contribute to the thermodynamic potential are the same of the zero-temperature expansion described in section 3.5, with the addition of the so-called anomalous diagram shown in Fig. 4.1. The anomalous diagrams are a particular class of diagrams that arises in the finite-temperature treatment. They involve particle- and hole-lines with the same momenta, a peculiarity that is forbidden by the zero-temperature formalism, for which $\vec{p}_{\text{hole}} \neq \vec{p}_{\text{particle}}$.

4.3 Expansion in the Limit $T \to 0$

We expect that in the limit $T \to 0$ the ground state of the system provided by the finite-T formalism coincides with that of the $T = 0$ formalism. However, the anomalous diagrams introduced by the finiteness of the temperature do not vanish generally for $T = 0$. As a consequence, the diagrammatic expansions of the two formalisms are different due to the presence of the additional anomalous diagrams. Furthermore, they also differ because the finite-T formalism in the limit $T \to 0$ makes use of the exact chemical potential $\mu = \epsilon_F$, i.e. the Fermi energy of the interacting system, while the $T = 0$ formalism uses the unperturbed Fermi energy $\mu_0 = \epsilon_F^0$, i.e. the Fermi energy of the non-interacting system, and generates the exact ground state adiabatically from the unperturbed ground state.
In the following, we show how a Taylor expansion of $\Omega(T, V, \mu)$ around $\Omega(T, V, \mu_0)$ gives rise to additional terms that cancel the contribution of the anomalous diagrams in the limit $T \to 0$ under the conditions specified by the Luttinger-Ward theorem [78, 79].

The contributions to the potential up to NLO are:

$$\begin{aligned} \Omega(T, V, \mu) &= \Omega_0 + \Omega_1 + \Omega_2 + \dots \\ &= \Omega_0 + \Omega_{1\pi} + \Omega_{it} + \Omega_{irr} + \Omega_A + \dots \ , \end{aligned} \tag{4.9}$$

where $\Omega_1 = \Omega_{1\pi}$ is the LO contribution in the chiral power counting and the remaining term $\Omega_2 = \Omega_{it} + \Omega_{irr} + \Omega_A$ belongs to NLO. The subscripts it, irr, A mean respectively iterated 1π-exchange, irreducible 2π-exchange and anomalous term.

To the same order, the number of particles is

$$N(T,V,\mu) = -\frac{\partial\Omega_0}{\partial\mu} - \frac{\partial\Omega_1}{\partial\mu} - \frac{\partial\Omega_2}{\partial\mu} \ . \tag{4.10}$$

We can expand first μ in the chiral-order contributions as done for Ω,

$$\mu = \mu_0 + \mu_1 + \mu_2 + \dots \ , \tag{4.11}$$

then replace it in eq. (4.10) and consider a Taylor expansion around $\mu = \mu_0$:

$$N = -\left.\frac{\partial\Omega_0}{\partial\mu}\right|_{\mu_0} - (\mu_1+\mu_2)\left.\frac{\partial^2\Omega_0}{\partial\mu^2}\right|_{\mu_0} - \frac{1}{2}\mu_1^2\left.\frac{\partial^3\Omega_0}{\partial\mu^3}\right|_{\mu_0} - \left.\frac{\partial\Omega_1}{\partial\mu}\right|_{\mu_0} - \mu_1\left.\frac{\partial^2\Omega_1}{\partial\mu^2}\right|_{\mu_0} - \left.\frac{\partial\Omega_2}{\partial\mu}\right|_{\mu_0} + \dots \tag{4.12}$$

Solving iteratively, we obtain:

$$\text{0th-order:} \qquad N = -\left.\frac{\partial\Omega_0}{\partial\mu}\right|_{\mu_0} \ , \tag{4.13}$$

$$\text{1st-order:} \qquad \mu_1 = -\frac{\partial\Omega_1/\partial\mu|_{\mu_0}}{\partial^2\Omega_0/\partial\mu^2|_{\mu_0}} \ . \tag{4.14}$$

We can now eliminate μ in favour of μ_0. We replace eq. (4.9) in the thermodynamic relation (4.5) and expand again in chiral powers up to second order around μ_0:

$$F = \Omega_0(\mu_0) + (\mu_1+\mu_2)\left.\frac{\partial\Omega_0}{\partial\mu}\right|_{\mu_0} + \frac{1}{2}\mu_1^2\left.\frac{\partial^2\Omega_0}{\partial\mu^2}\right|_{\mu_0} + \Omega_1(\mu_0) + \mu_1\left.\frac{\partial\Omega_1}{\partial\mu}\right|_{\mu_0} + \Omega_2(\mu_0) + \mu_0 N + (\mu_1+\mu_2)N. \tag{4.15}$$

Using Eqs. (4.13) and (4.14), we note that the terms in μ_2 cancel. Moreover, we set $F_0 = \Omega_0 + \mu_0 N$: this is the free energy of the free Fermi gas. Because we deal with an infinitely extended system, it is more appropriate to introduce the free energy density $\mathcal{F}(\rho,T) = F(T,V,N)/V$, with $\rho = N/V$ the density of the system:

$$\mathcal{F}(\rho,T) = \mathcal{F}_0(\rho,T) + \Omega_{1\pi}(\mu_0) + \Omega_{it}(\mu_0) + \Omega_{irr}(\mu_0) + \left[\Omega_A(\mu_0) - \frac{1}{2}\frac{(\partial\Omega_{1\pi}/\partial\mu|_{\mu_0})^2}{\partial^2\Omega_0/\partial\mu^2|_{\mu_0}}\right] \ , \tag{4.16}$$

where $\Omega = \Omega/V$.

At $T = 0$, the free energy density reduces to the energy density and we recover the expansion of the $T = 0$ formalism if the last term in the square bracket vanishes. Such property is ensured by the Luttinger-Ward theorem under the condition that the unperturbed Fermi sea is spherically symmetric and the interaction is invariant under spatial rotations [79], a condition certainly satisfied in nuclear matter. In detail, the cancellation between the anomalous diagram and the extra contribution results from the shift of the chemical potential from μ to μ_0 that takes place at $T = 0$.

4.4 The Approximation Scheme

The free energy density in eq. (4.16) depends on the chemical potential μ_0 of the free Fermi gas. We want to understand the approximations implied by this relation.

From the thermodynamic relations (4.4) and (4.5), we find the free energy per particle and the particle density:

$$\bar{F} = \frac{F}{N} = \bar{\Omega} - \mu \frac{\partial \bar{\Omega}}{\partial \mu} \ , \qquad \rho = \frac{N}{V} = -\frac{\partial \Omega}{\partial \mu} \ . \tag{4.17}$$

We separate the contribution of the non-interacting Fermi gas from that of the interactions writing $\Omega = \Omega_0 + \Omega'$. The two relations become:

$$\bar{F} = \rho^{-1} \left[\mu + \Omega_0 + \Omega' - \mu \frac{\partial \Omega'}{\partial \mu} \right] \ , \tag{4.18}$$

$$\rho = -\frac{\partial \Omega_0}{\partial \mu} - \frac{\partial \Omega'}{\partial \mu} = \frac{g}{2\pi^2} \int_0^\infty \mathrm{d}p \, p^2 \, n_F(p) - \frac{\partial \Omega'}{\partial \mu} \ , \tag{4.19}$$

with $n_F(p)$ the Fermi distribution function, $n_F(p) = \{1 + e^{\beta[\epsilon(p) - \mu]}\}^{-1}$.

The calculation of the thermodynamic quantities could in principle be performed for fixed μ and T, but the density and the thermodynamic potential are double-valued for $\mu \leq 0$ due to the presence of the liquid-gas phase transition. Then, we use the density as an input and find the chemical potential inverting eq. (4.19). This can be achieved neglecting the derivative term $\partial \Omega'/\partial \mu$, i.e. considering just the free Fermi gas. Such procedure follows in part the scheme in Ref. [19]. The chemical potential so obtained is μ_0 and does not correspond to the true chemical potential of the system. If we consider for the derivative term in eq. (4.18) only the 1π-exchange and set $\mathcal{F}_0 = \mu + \Omega_0$, we essentially recover eq. (4.16).

To summarize, the present approximation scheme neglects the μ-dependence of the interaction between the particles in the evaluation of the chemical potential and uses the free chemical potential μ_0 for the calculation of the thermodynamic quantities.

4.5 Finite-Temperature Extension of the Perturbative Expansion

The description of isospin-symmetric nuclear matter in terms of medium insertions at $T = 0$ that has been presented in section 3.5 is now extended to finite temperature. Due to the relatively low temperatures ($T \leq 30$ MeV) that are of interest in the discussion of the thermodynamic properties of nuclear matter, one can neglect the effects coming from thermal pions ($m_\pi \simeq 135$ MeV) or the thermal production of nucleon-antinucleon pairs. Moreover, the nucleons can be treated non-relativistically.

A consistent extension to finite temperature, with the correct $T \to 0$ limit eq. (3.58), is the following [80]:

$$\begin{aligned} \rho \, \bar{F}(\rho, T) = 4 \int_0^\infty \mathrm{d}p \, p \, \mathcal{K}_1(p) \, d(p) + \int_0^\infty \mathrm{d}p_1 \int_0^\infty \mathrm{d}p_2 \, \mathcal{K}_2(p_1, p_2) \, d(p_1) \, d(p_2) \\ + \int_0^\infty \mathrm{d}p_1 \int_0^\infty \mathrm{d}p_2 \int_0^\infty \mathrm{d}p_3 \, \mathcal{K}_3(p_1, p_2, p_3) \, d(p_1) \, d(p_2) \, d(p_3) + \rho \, \bar{\mathcal{A}}(\rho, T) \ . \end{aligned} \tag{4.20}$$

The free energy per particle $\bar{F}$ is a function of particle density ρ and temperature T and is given by a sum of convolution integrals. The corresponding kernels $\mathcal{K}_j$ and the anomalous contribution $\bar{\mathcal{A}}(\rho, T)$ are specified in Appendix B.1. The one-body term with $\mathcal{K}_1$ is the contribution of the non-interacting Fermi gas, the terms $\mathcal{K}_2$ and $\mathcal{K}_3$ involve the two-body and three-body contributions and correspond, in the $T = 0$ formalism, to diagrams with two and three medium insertions, respectively.

The function $d(p)$ is the density of nucleon states in momentum space:

$$d(p) = \frac{p}{2\,\pi^2}\left[1 + \exp\frac{p^2/2M_N - \mu_0}{T}\right]^{-1} , \tag{4.21}$$

where $p/2\pi^2$ is a factor included for convenience and the other factor is just the Fermi distribution function $n_F(p)$.

The one-body "chemical potential" μ_0 is related to the density ρ through

$$\rho = 4\int_0^\infty \mathrm{d}p\, p\, d(p) = -\sqrt{2}\left(\frac{MT}{\pi}\right)^{\frac{3}{2}} \mathrm{Li}_{3/2}\left(-e^{\mu_0/T}\right) , \tag{4.22}$$

where $\mathrm{Li}_\nu(x)$ is the polylogarithmic function of index ν for $|x| < 1$. The true chemical potential of the system can be found using the thermodynamic relations:

$$\mu = \left.\frac{\partial(\rho\bar{F})}{\partial\rho}\right|_T = \bar{F} + \rho\,\frac{\partial\bar{F}}{\partial\rho} . \tag{4.23}$$

The anomalous contribution $\bar{\mathcal{A}}(\rho,T)$ corresponds to the term in the square brackets of eq. (4.16). It is evaluated considering only the static part ($M_N \to \infty$) of the 1π-exchange dynamics and, as concerns the anomalous diagram, using the Bloch-De Dominicis rules (see eq. (22) in Ref. [78]). It is a small contribution in the range of temperatures considered and vanishes in the limit $T \to 0$ because of the Kohn-Luttinger-Ward theorem, as explained in section 4.3.

Note that, using the finite-temperature nucleon propagator eq. (A.44) obtained in Thermal Field Theory, one recovers the expansion (4.20) in complete analogy with the $T = 0$ formalism: the step function in the medium insertion is now replaced by the Fermi distribution function. The finite-temperature propagator provides a theoretical foundation of the extension eq. (4.20).

The calculation can then be generalized to isospin-asymmetric nuclear matter and neutron matter. In comparison with the calculation for symmetric nuclear matter, the only changes required are in isospin factors and the introduction of two new contact terms whose coefficients are labeled by $B_{n,3}$ and $B_{n,5}$, corresponding to subtraction constants in the dispersion relation for neutron-neutron scattering. These coefficients are adjusted in order to reproduce the values of 34 MeV for the asymmetry energy at the saturation point [55]. The propagator (3.56) at $T = 0$ is split into proton and neutron contributions using isospin-projectors:

$$\theta(k_F - |\vec{p}\,|) \longrightarrow \frac{1+\tau_3}{2}\,\theta(k_p - |\vec{p}\,|) + \frac{1-\tau_3}{2}\,\theta(k_n - |\vec{p}\,|) , \tag{4.24}$$

with k_p and k_n denoting, respectively, the Fermi momenta of protons and neutrons. The "one-body" chemical potentials of the two nucleon species in eq. (4.22) are now different. At finite temperature we replace

$$d(p) \longrightarrow \frac{1+\tau_3}{2}\,d_p(p) + \frac{1-\tau_3}{2}\,d_n(p) , \tag{4.25}$$

where d_p and d_n are the proton and neutron distributions. Each diagram now involves the sum of all possible combinations of proton and neutron medium insertions with their specific isospin factors. In Appendix B.2 a complete list of the modifications to be done on the kernels for generalizing to isospin-asymmetric nuclear matter is reported [76].

Finally, using the differential relation eq. (4.1), the pressure is derived from the free energy per particle:

$$P(\rho,T) = \rho^2\,\frac{\partial\bar{F}(\rho,T)}{\partial\rho} . \tag{4.26}$$

In the following sections we show the results of the numerical calculation of the equation of state of nuclear matter.

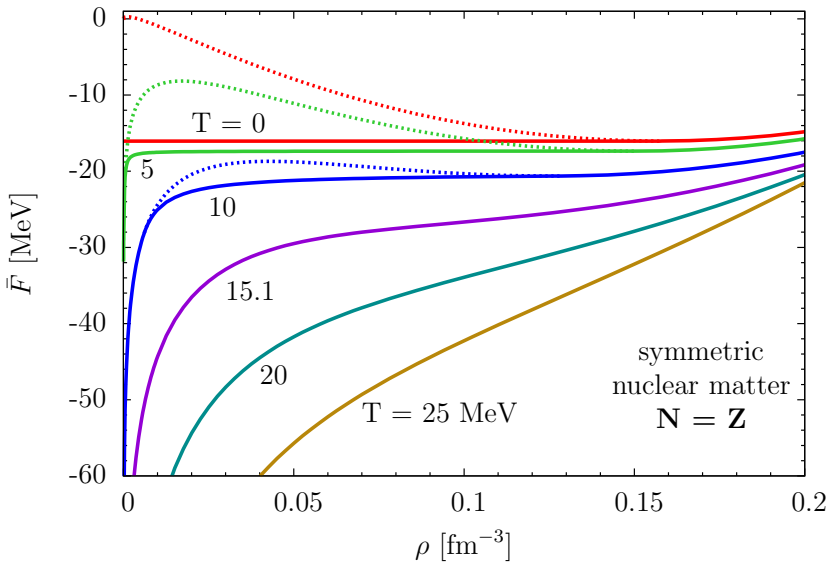

Figure 4.2: Free energy per particle of isospin-symmetric nuclear matter as a function of baryon density ρ for different temperatures. The dotted line indicates the non-physical behaviour of the free energy in the liquid-gas coexistence region. The physical free energy (solid lines) at low temperatures ($T \lesssim 15$ MeV) is obtained using the Maxwell construction.

4.6 Equation of State of Isospin-Symmetric Nuclear Matter

We consider first the case of isospin-symmetric nuclear matter. The free energy per particle $\bar{F}(\rho, T)$ as a function of density ρ for a sequence of temperatures up to 25 MeV is calculated using eq. (4.20) with the input for the interaction kernels $\mathcal{K}_n$ specified in Appendix B.1. The result is shown in Fig. 4.2. The dotted lines indicate the non-physical behaviour of the equation of state in the liquid-gas first-order transition region. This part of each curve is substituted by the physical one (solid lines) using the Maxwell construction.

We briefly remind the main steps of the Maxwell construction. We plot first the free energy per particle $\bar{F}(\rho)$ as a function of the volume per particle $v = 1/\rho$. The region with negative curvature is unphysical and is eliminated through the double tangent construction: we search for the two points of the curve with the same tangent. This tangent line is the physical free energy in the phase coexistence region and its negative slope gives the physical pressure, which is constant. The two points with the same tangent are the boundary of the coexistence region.

At $T = 0$ the free energy equals the internal energy of the system. The minimum of the curve (the saturation point) is located at $\bar{E}_0 = -16.0$ MeV, $\rho_0 = 0.157$ fm^{-3}, $k_{F0} = 1.33$ fm^{-1} $= 262$ MeV. At finite temperatures the free energy displays a singular behaviour for $\rho \to 0$; this is a well-known generic feature that the present calculation shares with other types of many-body calculations [23, 81].

The energy per particle of symmetric nuclear matter is commonly expanded around the saturation point:

$$\bar{E}(\rho) \approx \bar{E}_0 + \frac{K}{2}\left(\frac{\rho - \rho_0}{3\rho_0}\right)^2 \quad , \tag{4.27}$$

with K the compression modulus. From the curve at $T = 0$ we extract the value $K \simeq 300$ MeV, slightly larger than the values deduced from relativistic mean field models ($K \approx 250 - 270$ MeV)[82] and from the systematics of nuclear monopole resonances ($K = 240 \pm 20$ MeV) [83].

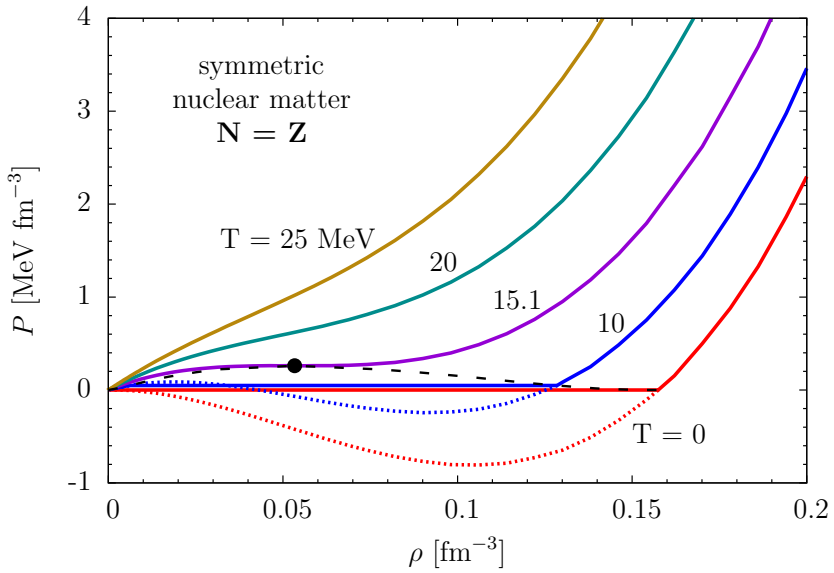

Figure 4.3: Pressure isotherms as a function of density for symmetric nuclear matter displaying a first-order liquid-gas phase transition. The dotted lines at low temperature show the non-physical behaviour of the isotherms in the transition region. The physical pressure is calculated using the Maxwell construction. The dashed line delimits the boundary of the coexistence region. The dot indicates the critical point ($T_c \simeq 15.1$ MeV, $\rho_c \simeq \rho_0/3$).

Fig. 4.3 shows isotherms of the pressure $P(\rho, T)$ as a function of density ρ. The emerging picture is qualitatively reminiscent of a van der Waals gas with its generic liquid-gas first-order phase transition. The liquid-gas phase transition is the result of a sensitive balance between intermediate range attraction and short-range repulsion, the former originating from 2π-exchange with intermediate Δ-isobar excitation and the latter represented by contact terms encoding non-perturbative physics unresolved in detail in the range of momenta relevant to the present study.

The critical temperature for the liquid-gas phase transition is found at $T_c \simeq 15.1$ MeV. For $T < T_c$ the usual Maxwell construction is applied, keeping the pressure constant in the liquid-gas coexistence region. Empirical values of this transition temperature deduced from multifragmentation and fission measurements locate T_c between 15 and 20 MeV [84–86]. Phenomenological Skyrme model studies gave a similar range for T_c [48].

In order to assess possible uncertainties of the thermodynamic properties in our calculation we have considered variations of the parameters B_5 and ζ. Within the ranges $-0.5 \leq B_5 \leq 0.5$ and $-0.8 \leq \zeta \leq -0.7$ the critical temperature varies from $T_c = 14.6$ MeV to $T_c = 15.8$ MeV, implying at most a change of $\pm 5\%$.

As a digression, we can interpret the behaviour of nuclear matter according to the equations of state in Fig. 4.2 and 4.3. We move for a given isotherm from $\rho = 0$ to increasing densities. At $T = 0$ (red curve), for densities below the saturation point, the energy of the system stays constantly at -16 MeV with zero pressure: in the absence of any repulsive Coulomb interaction, it is convenient for nuclear matter to form a liquid with density ρ_0. The energy of the system is negative and nuclear matter is self-bounded. For densities higher than ρ_0, the pressure rises as well as its energy. At finite temperature the picture is slightly different. At very low density nuclear matter is gaseous and, when compressed, it enter the transition region with the appearance of a liquid phase. As a result, pressure during the change of phase is non zero (see blue curve). As density increases the nucleon gas passes to the liquid phase and the nuclear liquid "cluster" grow in size. At the end of

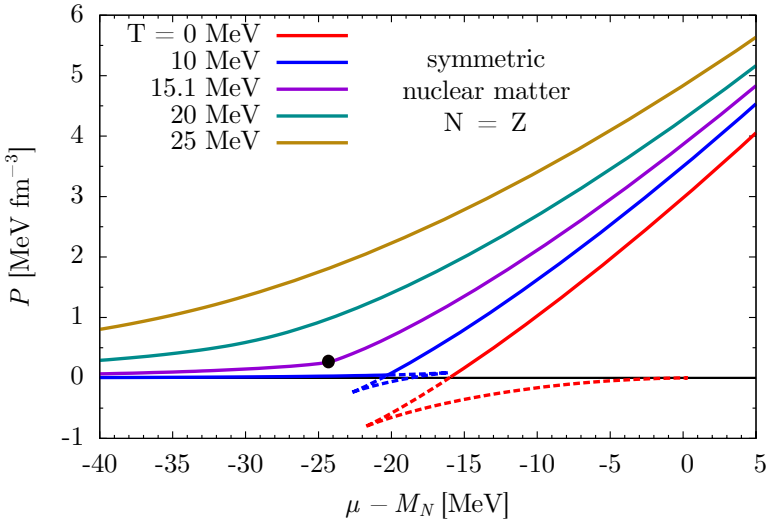

Figure 4.4: Pressure isotherms as functions of the nucleon chemical potential μ for isospin-symmetric nuclear matter. The dotted double-valued region of the curves at temperatures below $T_c \simeq 15.1$ MeV corresponds to the non-physical behaviour of the equation of state in the liquid-gas coexistence region. In this region the actual pressure and chemical potential are constant and determined by the Maxwell construction. The dot indicates the critical point.

the transition, the nuclear liquid occupies the whole volume. Above T_c no phase transition takes place and nuclear matter is an interacting Fermi liquid.

We complete the discussion of the equation of state by displaying the pressure as a function of the nucleon chemical potential (including the free nucleon mass),

$$\mu = M_N + \left(1 + \rho \frac{\partial}{\partial \rho}\right) \bar{F}(\rho, T) \ , \tag{4.28}$$

in Fig. 4.4. The non-physical (dotted) curves in $P(\rho, T)$ of Fig. 4.3 are related to the double-valued behaviour of P as function of μ at temperatures below T_c. In this coexistence region the actual pressure and chemical potential are constant and given by the intersection point of the double-valued loop according to the Maxwell construction. The temperature at which this loop reduces to a point is the critical temperature T_c.

All relevant informations about the phase transition are collected in the $T - \mu$, $P - T$ and $T - \rho$ phase diagrams (Fig. 4.5). In Fig. 4.5a we display temperature versus chemical potential ($T - \mu$) and in Fig. 4.5b pressure versus temperature ($P - T$). In these diagrams the coexistence region gets projected onto a first-order phase transition line. The first-order transition region terminates at the critical point indicated by the dot. The following critical values of thermodynamic quantities (pressure, baryon chemical potential and density) are found: $P_c \simeq 0.261\,\text{MeV fm}^{-3}$, $\mu_c \simeq 914.7$ MeV and $\rho_c \simeq 0.053\,\text{fm}^{-3}$ at $T_c = 15.1$ MeV. The $T - \rho$ phase diagram, Fig. 4.5c, clearly illustrates the extension of the gas-liquid coexistence region.

At $T = 0$ the third law of thermodynamics gives important constraints about the slope of the boundaries of the transition region. It implies that the boundaries of the transition region at $T = 0$ have an infinite slope in the $T - \rho$ and $T - \mu$ diagrams and a zero slope in the $P - T$ diagram. Moreover, the chemical potential at $T = 0$ is known and given by the total energy per particle at the saturation point, i.e. $\mu = M_N + \bar{E}_0 \simeq 923$ MeV.

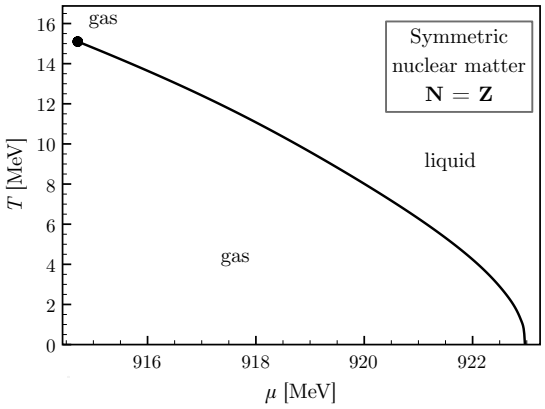

(a) Temperature vs chemical potential.

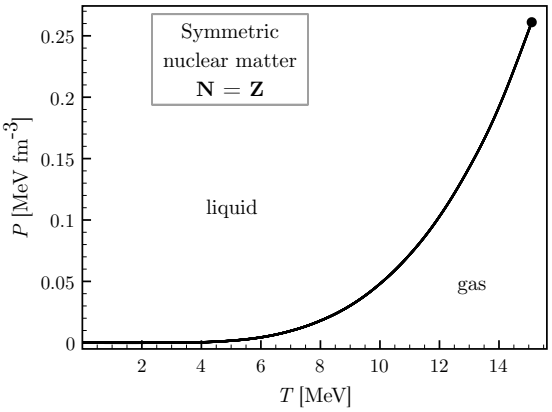

(b) Pressure vs temperature.

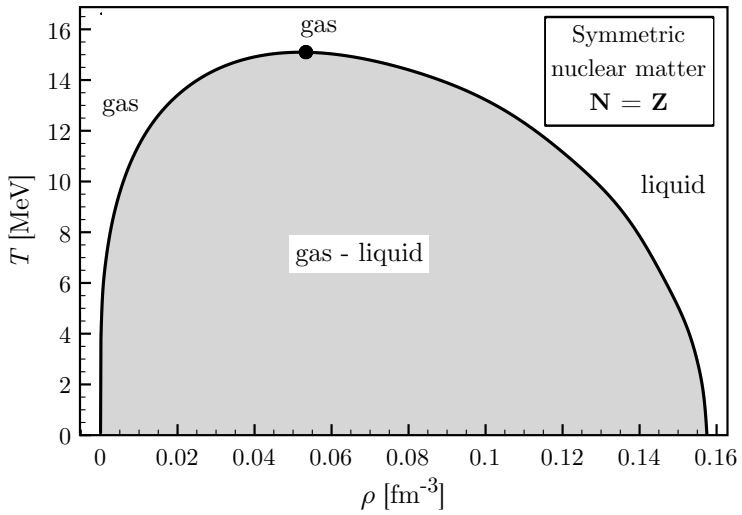

(c) Temperature vs density.

Figure 4.5: Phase diagrams of symmetric nuclear matter [76]. The dot indicates the critical point.

Proton fraction	*Saturation point*	
$\mathbf{x_p}$	ρ_{sat} [fm^{-3}]	$\bar{E}_{sat}$ [MeV]
0.5	0.157	-16.0
0.4	0.152	-14.7
0.3	0.137	-10.9
0.2	0.113	-5.24
0.12	0.087	0

Table 4.1: Saturation point as a function of the proton fraction $x_p = Z/A$: listed are the saturation density and the binding energy.

4.7 Equation of State of Isospin-Asymmetric Nuclear Matter

The next step is the investigation of the dependence of nuclear matter properties on the isospin-asymmetry. The amount of asymmetry is given in terms of the proton fraction, $x_p = Z/A = \rho_p/(\rho_p + \rho_n)$. The calculations are based on the expansion of the free energy density, eq. (4.20), with modifications specified in Appendix B.2.

The resulting equations of state are shown in Fig. 4.6 for different values of the proton fraction, $x_p = 0.3$, 0.1 and 0. The limiting case $x_p = 0$ corresponds to pure neutron matter. The left column of Fig. 4.6 displays the free energy per particle, the right column shows the pressure, both as a function of the baryon density $\rho = \rho_n + \rho_p$.

As the neutron-proton asymmetry increases, the free energy and the pressure increase at given density, indicating the reduced binding in neutron-rich matter, because of the Pauli exclusion principle and the smaller degeneracy. Pure neutron matter is unbound. The coexistence region of the liquid-gas phase transition shrinks with decreasing proton fraction until it disappears and only the interacting Fermi gas phase remains.

Note that for pure neutron matter the Pauli principle forbids a three-body contact interaction. The behaviour of pure neutron matter at low density ($\rho \lesssim 0.02\,\mathrm{fm}^{-3}$) is dictated by the unnaturally large neutron-neutron scattering length, $a_{nn} \simeq 19$ fm [117, 118], which invalidates the usual perturbative momentum expansion [50]. For a realistic description of pure or rich-neutron matter the resummation of the short-distance NN interaction to all orders in the presence of the medium is required [57].

To complete the picture, consider the evolution of the saturation point, defined as the minimum of the energy curve at $T = 0$, in Fig. 4.7. Starting from its minimum for symmetric nuclear matter, $\bar{E}_0 \simeq -16$ MeV at $\rho_0 \simeq 0.157\,\mathrm{fm}^{-3}$, the binding energy per nucleon is reduced continuously with decreasing x_p until it vanishes at a proton fraction $x_p \simeq 0.12$. Beyond this point neutron-rich matter at $T = 0$ is unbound. In Tab. 4.1 the saturation density and the corresponding binding energy are reported for decreasing values of x_p.

Phase diagrams of isospin-asymmetric nuclear matter are shown in Fig. 4.8 for different proton fractions, demonstrating how the matter evolves with increasing asymmetry. The dashed line shows the evolution of the critical point and its disappearance at $x_p \simeq 0.053$. At this particular proton fraction the coexistence region reduces to a point, as can be seen in the $T - \rho$ diagram, meaning that the liquid-gas phase transition does not take place any more. Neutron-rich matter with $x_p \lesssim 0.053$ is always in a gaseous phase. The values of the thermodynamic quantities at the different critical points are listed in Tab. 4.2. Note that the critical point disappears at a small but finite pressure.

The following features of the phase diagram in Fig. 4.8 are worth noting. Above a proton fraction close to $x_p \simeq 0.1$ (0.12 more precisely), the gas-liquid coexistence region starts at zero density. A qualitative change in the behaviour of the coexistence region takes place at

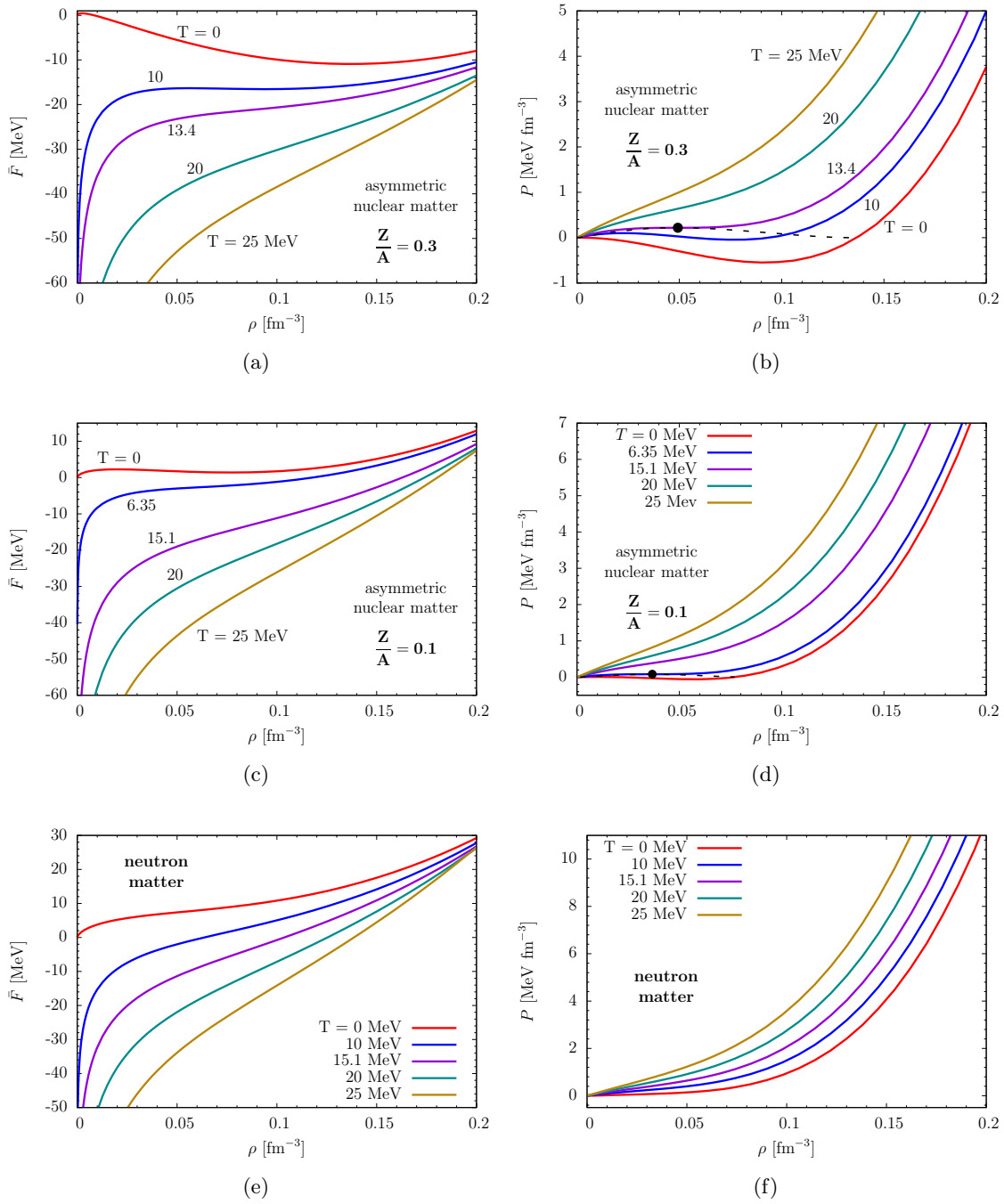

Figure 4.6: Isospin-asymmetric nuclear matter: free energy per particle (left column) and pressure isotherms (right column) as a function of nucleon density for proton fractions x_p = 0.3, 0.1 and 0 [76]. The coexistence region, with boundary delimited by the dashed line, gradually diminishes with increasing isospin-asymmetry until it disappears at $x_p = 0.053$. The dot indicates the critical point.

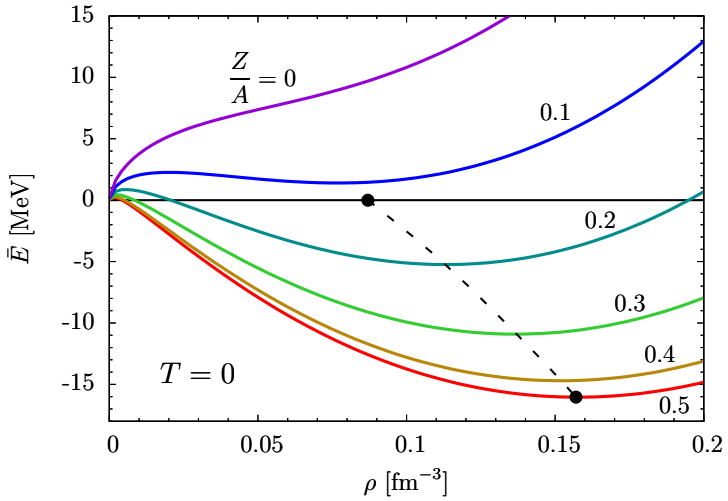

Figure 4.7: Dependence of energy per particle and saturation point of nuclear matter at $T = 0$ on the asymmetry [76]. The solid lines represent the energy per particle as a function of nucleon density $\rho = \rho_n + \rho_p$ for different proton fractions $x_p = Z/A$. The dashed line shows the trajectory of the saturation point as x_p varies. For $x_p \lesssim 0.12$ the energy is always positive.

Proton fraction	*Critical point*			
$\mathbf{x_p}$	T_c [MeV]	P_c [MeV fm^{-3}]	μ_c [MeV]	ρ_c [fm^{-3}]
0.5	15.1	0.26	914.7	0.053
0.4	14.7	0.25	916.1	0.053
0.3	13.4	0.22	920.1	0.049
0.2	10.9	0.16	927.2	0.044
0.1	6.4	0.08	937.6	0.037
0.053	0	0.02	943.6	0.032

Table 4.2: Critical point as a function of the proton fraction $x_p = Z/A$: listed are the temperature, pressure, chemical potential and density.

$x_p = 0.12$, the point at which the binding energy at $T = 0$ vanishes. Following the dashed line in Fig. 4.7 that represents absolute minima of the energy per particle, one observes that for $x_p \lesssim 0.12$ there is still a local minimum in $\bar{E}(\rho, x_p)$, but the absolute minimum is now located at $\rho = 0$. Consequently, neutron-rich nuclear matter for $x_p \lesssim 0.12$ is a gas at very low density and $T = 0$, and then enters the coexistence region as the density increases. This is the reason why the transition line in the $T - \rho$ phase diagram starts at finite density for $x_p \lesssim 0.12$. In the range $0.053 \lesssim x_p \lesssim 0.12$ nuclear matter is not self-bound but it can still have a liquid-gas phase transition.

The present chiral thermodynamics framework for nuclear matter is, of course, oversimplified at low densities ($\rho \lesssim 0.05\,\text{fm}^{-3}$) where nuclear clustering takes place. However, in a detailed study combining the appearance of clusters of light nuclei (deuteron, triton and helium, i.e. $A < 4$) with relativistic mean field phenomenology [87], only modest changes of the $T - \mu$ phase diagram have been found when cluster formation is incorporated: a variation of less than 10% for T_c and less than 1% for μ_c.

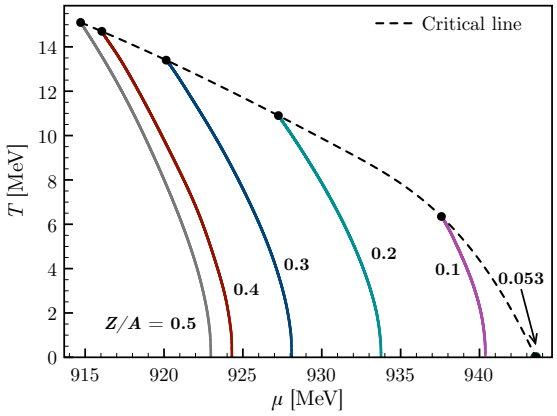

(a) Temperature vs chemical potential.

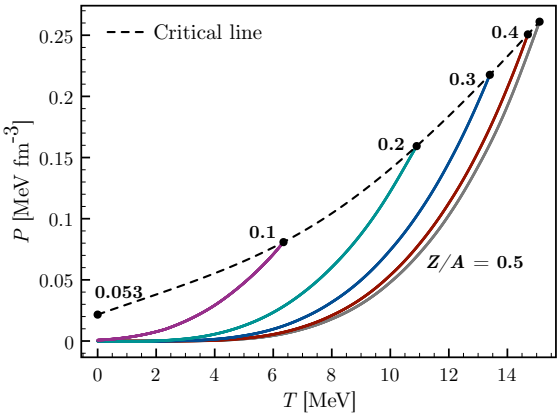

(b) Pressure vs temperature.

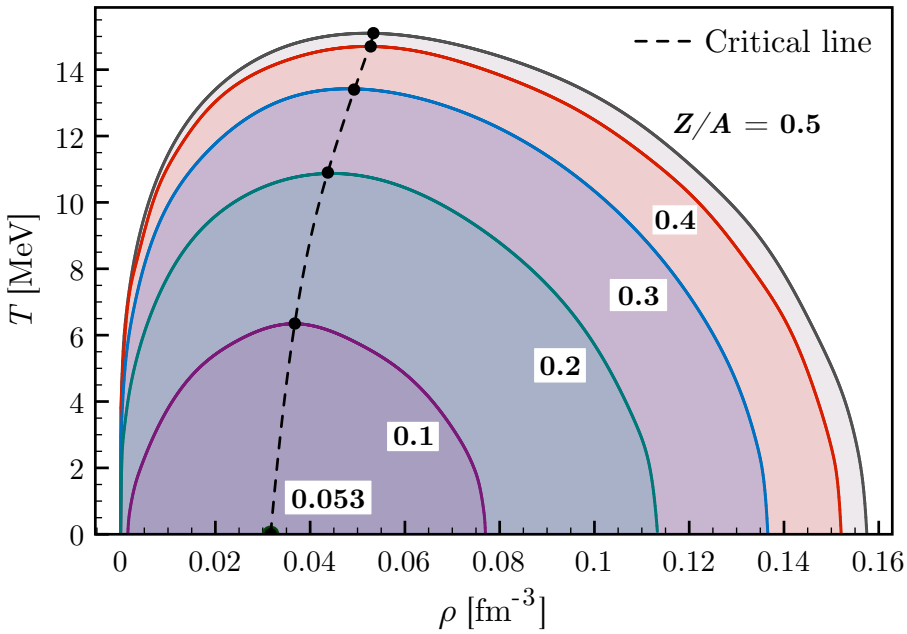

(c) Temperature vs density.

Figure 4.8: Phase diagrams of isospin-asymmetric nuclear matter for different proton fractions [76]. The dashed line shows the evolution of the critical point.

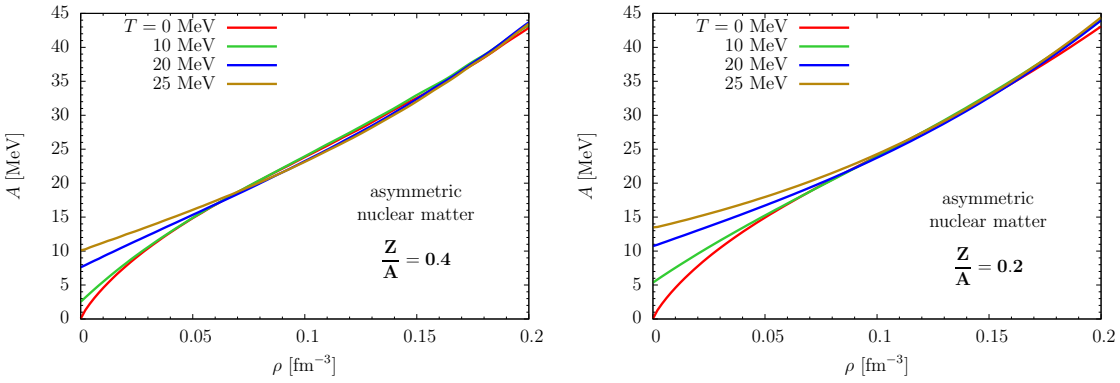

Figure 4.9: Asymmetry free energy per particle as a function of the density for different temperatures. In the left panel $\delta = 0.2$ ($x_p = 0.4$), in the right panel $\delta = 0.6$ ($x_p = 0.2$).

4.8 Asymmetry Free Energy

Introducing the asymmetry parameter

$$\delta = \frac{\rho_n - \rho_p}{\rho} = 1 - 2x_p \ , \tag{4.29}$$

the free energy per particle can be expanded in powers of δ around the free energy of isospin-symmetric nuclear matter:

$$\bar{F}(\rho_p, \rho_n, T) = \bar{F}(\rho, T) + A(\rho, T)\,\delta^2 + \mathcal{O}(\delta^4) \ . \tag{4.30}$$

This defines the asymmetry free energy per particle, $A(\rho, T)$. The expansion of $\bar{F}$ involves only even powers of δ as long as we ignore isospin-symmetry breaking effects. In this limit nuclear matter is invariant under the interchange of protons and neutrons. The asymmetry energy is related to the asymmetry term of the semi-empirical mass formula (2.3) that is non-vanishing for $N \neq Z$.

In Fig. 4.9 we show the behaviour of the asymmetry free energy $A(\rho, T)$ for $\delta = 0.2$ ($x_p = 0.4$) and $\delta = 0.6$ ($x_p = 0.2$) as a function of the nucleon density for different temperatures. We note that the asymmetry free energy is sensitive to the temperature only at low densities, $\rho < 0.1\,\mathrm{fm}^{-3}$.

A test of the validity of the parabolic approximation is shown in Fig. 4.10, where we plot the free energy difference with respect to isospin-symmetric nuclear matter as a function of δ^2 for different densities $\rho = \rho_n + \rho_p$. At $T = 0$ (Fig. 4.10a) the linear dependence on δ^2 is seen to be realized very well even up to large δ. At higher temperature ($T = 20$ MeV, 4.10b), a slight bending is observed especially at low density. In summary, eq. (4.30) is confirmed to be a good approximation of the free energy; the term of order δ^4 is generally negligible for most applications, even for large values of δ. This feature has also been observed in other calculations [18, 21]. Estimates give a value of the quartic term smaller than 1 MeV at the saturation point [18].

At the saturation density ρ_0 we have imposed $A(\rho_0, T = 0) \simeq 34.0$ MeV in our calculation in order to fix the contact terms associated with the isospin-dependent part of the interaction. For comparison, a relativistic mean-field model [82] constrained by the properties of selected nuclei gives $A(\rho_0) = 34 \pm 2$ MeV. A more recent estimate using the same relativistic mean-field phenomenology constrained by giant dipole resonances [90] suggests $A(\rho_0)$ in the range (33 - 37) MeV. A further estimate in the same paper gives the asymmetry energy at lower density, $\rho = 0.1$ fm^{-3}, in a window between 21 and 23 MeV, slightly lower than our calculated value $A(0.1\,\mathrm{fm}^{-3}, T = 0) \simeq 23.9$ MeV. Previous determinations from extensive fits of nuclide masses [91, 92] gave $A(\rho_0)$ between 33 and 37 MeV.

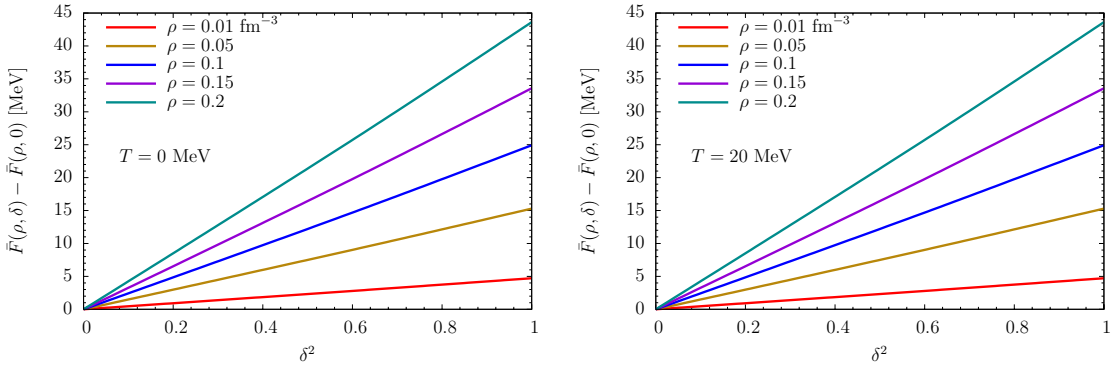

(a) $T = 0$. (b) $T = 20$ MeV.

Figure 4.10: Free energy per particle of nuclear matter as a function of the asymmetry parameter δ^2 for different densities.

Around the saturation point ρ_0, the asymmetry energy at $T = 0$ can be expanded in powers of $\rho - \rho_0$ as follows:

$$A(\rho) = A(\rho_0) + L\,\frac{\rho-\rho_0}{3\rho_0} + \frac{K_{as}}{2}\left(\frac{\rho-\rho_0}{3\rho_0}\right)^2 + \dots \tag{4.31}$$

We extract the coefficients $L \simeq 90.1$ MeV and $K_{as} \simeq 153$ MeV. The value of L, in particular, is compatible with empirical constraints from isospin diffusion which give $L = 88 \pm 25$ MeV [18].

For small asymmetries δ, the saturation density can be calculated taking the minimum of the curve (4.30) at $T = 0$:

$$\left.\frac{\partial \bar{E}(\rho,\delta)}{\partial\rho}\right|_{\rho=\rho_{sat}} = \left.\frac{\partial \bar{E}(\rho,0)}{\partial\rho}\right|_{\rho=\rho_{sat}} + \delta^2 \left.\frac{\partial A(\rho)}{\partial\rho}\right|_{\rho=\rho_{sat}} = 0\ . \tag{4.32}$$

Using eqs. (4.27) and (4.31) to evaluate the derivatives, the saturation density gets lowered to:

$$\rho_{sat}(\delta) \approx \rho_0\left[1 - \frac{3L}{K}\,\delta^2\right]\ . \tag{4.33}$$

The corresponding compression modulus $K(\delta)$ is often expressed as an expansion in powers of δ:

$$K(\delta) = K + K_\tau \delta^2 + \mathcal{O}(\delta^4)\ , \tag{4.34}$$

where K is the compressibility of symmetric nuclear matter and K_τ is called isobaric compressibility. If we consider the definition of compressibility, we can relate K_τ to the other quantities L and K_{as}:

$$K(\delta) = 9\,\rho_{sat}^2 \left.\frac{\partial^2 \bar{E}(\rho,\delta)}{\partial\rho^2}\right|_{\rho=\rho_{sat}} \approx K + (K_{as} - 6L)\,\delta^2\ , \tag{4.35}$$

with

$$K_\tau \approx K_{as} - 6L\ . \tag{4.36}$$

Our calculated value is $K_\tau = -388$ MeV. The empirical determination suffers from large uncertainties. A recent result from measurements of the isotopic dependence of giant monopole resonances in even-A isotopes gives $K_\tau = -550 \pm 100$ MeV [93].

4.9 Comparison to Other Approaches

In the recent literature several calculations of the thermodynamic properties of nuclear matter using different approaches can be found [94–98]. In the following we comment on some of these, based either on the self-consistent Green's function (SCGF) method [97] or on mean field theory [98].

As pointed out in Ref. [94], many traditional studies of nuclear matter at finite temperature in mean field approximation treat the temperature dependence in a naive way. The temperature dependence arises mainly from the replacement of the step function momentum distribution at zero temperature by the corresponding Fermi-Dirac distribution. In this way the temperature dependence of the phenomenological interactions accounting for the correlations between nucleons is ignored. On the other hand, in many-body calculations based on microscopic approaches, such as ours, the nuclear medium generates Pauli blocking effects that are weakened with increasing temperature. Consequently nuclear matter properties and correlations in the medium are temperature dependent in a non-trivial way.

In the SCGF approach the ladder approximation provides the minimal scheme for the description of the effective NN interaction in the medium. The three-body Green's function is decomposed into a one-body and a two-body propagator and arranged in an integral equation for the in-medium T-matrix that sums the ladder diagrams to all orders. The set of equations including the T-matrix, the nucleon self-energy and the single-particle Green's function can then be solved self-consistently. In Ref. [97] the equation of state of isospin-symmetric nuclear matter has been calculated using such an approach in combination with the CD-Bonn and Nijmegen NN potentials. Contributions of three body forces are included via an effective (density-dependent) two-body interaction. The pressure $P(\rho, T, \delta)$ is found to be strongly dependent on three body correlations and the liquid-gas coexistence region gets reduced in size when they are included. With the CD-Bonn NN potential the critical temperature results in $T_c = 12.5$ MeV. When using the Nijmegen potential T_c reduces to 11.5 MeV. The critical density lies in the range $\rho_c \simeq 0.09 - 0.11\,\mathrm{fm}^{-3}$ and the critical pressure is about $0.15\,\mathrm{MeV\ fm}^{-3}$. The results of these calculations, including the very low value of T_c, differs significantly from ours (compare with Tab. 4.2).

In Ref. [98] the properties of nuclear matter have been calculated in the framework of relativistic mean field theory with density-dependent meson-nucleon couplings accounting for medium modifications. This method has been successful in describing many properties of both nuclear matter and finite nuclei. For symmetric nuclear matter a critical temperature of $T_c = 13.2$ MeV is found, while the liquid-gas coexistence region vanishes at $x_p \simeq 0.07$. The emerging picture is closer to the one we have obtained in the present paper. The main difference is a somewhat smaller phase transition region.

Chapter 5

Thermodynamics of the Chiral Condensate in Symmetric Nuclear Matter

The chiral condensate is the order parameter of the chiral phase transition. It is expected to drop with increasing density and temperature. Its vanishing determines the transition from the Nambu-Goldstone phase of QCD with spontaneously broken chiral symmetry to the Wigner-Weyl realization of the chiral symmetry. Next to this chiral phase restoration the pions would loose their status of Goldstone bosons arising from the spontaneous chiral symmetry breaking.

Many lattice QCD calculations indicate that the chiral "phase transition" is actually a crossover whose critical temperature is deduced by the peak of the chiral susceptibility $\chi = -\partial \langle \bar{q}q \rangle / \partial m_q$. According to Ref. [100], the transition temperature lies in the band $T_c = (160 \pm 30)$ MeV. A recent estimate from the HotQCD Collaboration, employing the staggered fermions scheme and an extrapolation to the continuum limit, gives $T_c = 154 \pm 9$ MeV [101]. The same collaboration, using the technique of domain wall fermions, finds a crossover behaviour going from a temperature of 159 MeV up to 168 MeV [102].

The calculation of the chiral condensate that we present systematically incorporates for the first time two-pion exchange dynamics in the nuclear medium. The Δ-isobar excitation and the medium effects are fundamental ingredients for stabilizing the condensate at large nucleon densities. The results obtained set important nuclear physics constraints for the construction of the QCD phase diagram at baryon densities and temperatures that are reached in relativistic heavy-ion collisions [103].

5.1 The Scalar Quark Condensate

We consider the following scalar and pseudoscalar densities for the case of light quarks:

$$S_0(x) = \bar{q}(x)q(x) \ , \qquad S_i(x) = \bar{q}(x)\tau_i q(x) \tag{5.1}$$

$$P_0(x) = i\bar{q}(x)\gamma_5 q(x) \ , \qquad P_i(x) = i\bar{q}(x)\gamma_5\tau_i q(x) \ . \tag{5.2}$$

Next we derive the commutators of these quark densities with the vector and axial charge operators:

$$Q_i^V(t) = \int \mathrm{d}^3x \ q^\dagger(\vec{x},t)\frac{\tau_i}{2}\, q(\vec{x},t) \ , \tag{5.3}$$

$$Q_i^A(t) = \int \mathrm{d}^3x \ q^\dagger(\vec{x},t)\,\gamma_5\frac{\tau_i}{2}\, q(\vec{x},t) \ . \tag{5.4}$$

A useful general expression is:

$$[q^\dagger(x)\hat{A}_1(x)\,q(x), q^\dagger(y)\hat{A}_2(y)\,q(y)] = \hat{A}^{rs}_{1\alpha\beta}(x)\,\hat{A}^{tu}_{2\gamma\delta}(y)\,[q^{\dagger r}_\alpha(x)\,q^s_\beta(x), q^{\dagger t}_\gamma(y)\,q^u_\delta(y)]\ , \tag{5.5}$$

where $x = (\vec{x}, t)$ and $y = (\vec{y}, t)$. $\alpha, \beta, \gamma, \delta$ are Dirac indices and r, s, t, u flavour indices. $\hat{A}_1$ and $\hat{A}_2$ are operators in Dirac and flavour space.

Using the following relation for the commutator

$$\begin{aligned}[AB, CD] &= [AB, C]D + C[AB, D] \\ &= A\{B, C\}D - \{A, C\}BD + CA\{B, D\} - C\{A, D\}B\end{aligned} \tag{5.6}$$

and the anticommutation rules of the quark fields, we find:

$$\{B, C\} = \{q^s_\beta(x), q^{\dagger t}_\gamma(y)\} = \delta^3(\vec{x} - \vec{y})\delta_{\beta\gamma}\delta^{st}\ , \tag{5.7}$$

$$\{A, C\} = \{q^{\dagger r}_\alpha(x), q^{\dagger t}_\gamma(y)\} = 0\ , \tag{5.8}$$

$$\{B, D\} = \{q^s_\beta(x), q^u_\delta(y)\} = 0\ , \tag{5.9}$$

$$\{A, D\} = \{q^{\dagger r}_\alpha(x), q^u_\delta(y)\} = \delta^3(\vec{x} - \vec{y})\delta_{\alpha\delta}\delta^{ru}\ . \tag{5.10}$$

Replacing in eq. (5.5), one arrives at the general relation

$$[q^\dagger(x)\hat{A}_1(x)\,q(x), q^\dagger(y)\hat{A}_2(y)\,q(y)] = \delta^3(\vec{x} - \vec{y})\,q^\dagger(x)[\hat{A}_1(x), \hat{A}_2(x)]q(x)\ . \tag{5.11}$$

Using eq. (5.11) in combination with

$$\left[\frac{\tau_i}{2}, \gamma_0\right] = 0\ , \qquad \left[\frac{\tau_i}{2}, \gamma_0\tau_j\right] = \gamma_0 i\epsilon_{ijk}\tau_k\ , \tag{5.12}$$

the commutators of the scalar densities are:

$$[Q^V_i(t), S_0(y)] = 0\ , \qquad [Q^V_i(t), S_i(y)] = i\epsilon_{ijk}S_k(y)\ . \tag{5.13}$$

The property of the Levi-Civita tensor

$$\epsilon_{ijk}\epsilon_{ijn} = 2\delta_{kn} \tag{5.14}$$

enables to invert the second equation in (5.13) and to express the isovector scalar field as

$$S_k(y) = -\frac{i}{2}\epsilon_{ijk}[Q^V_i(t), S_j(y)]\ . \tag{5.15}$$

In the chiral limit, $Q^V_i\,|0\rangle = 0$ because the $SU(2)_V$ symmetry is unbroken. It follows that

$$\langle 0\,|\,S_k(y)\,|\,0\rangle = \langle 0\,|\,S_k(0)\,|\,0\rangle \equiv \langle S_k\rangle = 0\ , \tag{5.16}$$

where we used the translational invariance of the vacuum. The third components gives the relation

$$\langle\bar{u}u\rangle - \langle\bar{d}d\rangle = 0 \longrightarrow \langle\bar{u}u\rangle = \langle\bar{d}d\rangle\ . \tag{5.17}$$

From the definition of scalar density we get the scalar quark condensate:

$$\langle S_0\rangle = \langle\bar{q}q\rangle = \langle\bar{u}u + \bar{q}q\rangle = 2\,\langle\bar{u}u\rangle = 2\,\langle\bar{d}d\rangle\ . \tag{5.18}$$

Concerning the pseudoscalar quark density, with the use of

$$\left[\gamma_5\frac{\tau_i}{2}, \gamma_0\gamma_5\tau_j\right] = -\gamma_0\delta_{ij}\ , \tag{5.19}$$

we evaluate the commutator with the axial charges:

$$i[Q_i^A(t), P_j(y)] = (\bar{u}u + \bar{d}d)\delta_{ij} \ . \tag{5.20}$$

Again, taking the vacuum expectation value, we find:

$$\left\langle 0 \,\middle|\, i[Q_i^A(t), P_j(y)] \,\middle|\, 0 \right\rangle = \langle \bar{q}q \rangle \, \delta_{ij} \ . \tag{5.21}$$

If the scalar quark condensate is not vanishing, $\langle \bar{q}q \rangle \neq 0$, this implies $Q_i^A \left|0\right\rangle \neq 0$ and $P_i(0) \left|0\right\rangle \neq 0$. A non-vanishing quark condensate is a sufficient condition for the spontaneous chiral symmetry breaking in QCD. The chiral condensate can be used as the order parameter of the chiral phase transition and its variation with density and temperature is the key issue to locate the chiral phase restoration in the QCD phase diagram.

5.2 Quark-Mass Dependence of the Pion Mass

The quark mass term in the QCD Lagrangian eq. (3.21) breaks the chiral symmetry explicitly. It is related to the pion mass term present in the ChPT Lagrangian eq. (3.24), as follows.

Consider the most general explicit symmetry breaking term in ChPT. At lowest order, it can be written:

$$\mathcal{L}_M = \frac{1}{2} f_\pi^2 B_0 \, \mathrm{Tr}(MU^\dagger + UM^\dagger) \ , \tag{5.22}$$

where M is the quark mass matrix eq. (3.22), B_0 is a parameter to be determined and the matrix U is given in eq. (3.27).

With $U = 1$, i.e. for the lowest-order term of the expansion (3.27), the energy density of the ground state results:

$$\langle \mathcal{H}_M \rangle = -f_\pi^2 B_0 (m_u + m_d) = -2 f_\pi^2 B_0 \, m_q \ , \tag{5.23}$$

with $m_q = (m_u + m_d)/2$.

At this point, we introduce the Hellmann-Feynman theorem. Given a Hamiltonian $H(\lambda)$ depending on a parameter λ that can be varied adiabatically, and given an eigenstate $|\psi(\lambda)\rangle$ of this Hamiltonian, the theorem states:

$$\frac{\mathrm{d}}{\mathrm{d}\lambda} \langle \psi(\lambda) \,|\, H \,|\, \psi(\lambda) \rangle = \left\langle \psi(\lambda) \left| \frac{\mathrm{d}H(\lambda)}{\mathrm{d}\lambda} \right| \psi(\lambda) \right\rangle \ , \tag{5.24}$$

with normalization $\langle \psi(\lambda) \,|\, \psi(\lambda) \rangle = 1$.

We apply this theorem to the QCD Hamiltonian density $\mathcal{H}_{\mathrm{QCD}} = \mathcal{H}_0 + m_q(\bar{u}u + \bar{d}d)$, with $\mathcal{H}_0$ the Hamiltonian density in the chiral limit. The parameter λ is the quark mass m_q. First, we calculate

$$\langle 0 | \frac{\partial \mathcal{H}_{\mathrm{QCD}}}{\partial m_q} | 0 \rangle \bigg|_{m_q=0} = \langle \bar{q}q \rangle_0 \ , \tag{5.25}$$

where the subscript indicates that all quantities are taken in the chiral limit. Then, because of the Hellmann-Feynman theorem, we have:

$$\langle \bar{q}q \rangle_0 = -2 f_\pi^2 B_0 \ . \tag{5.26}$$

At second order in the expansion of U, the Lagrangian (5.22) takes the form:

$$\mathcal{L}_M = -\frac{B_0}{2}\,\mathrm{Tr}(M\boldsymbol{\pi}^2) \tag{5.27}$$

$$= -\frac{B_0}{2}[2(m_u+m_d)\pi^+\pi^- + (m_u+m_d)\pi^0\pi^0] \tag{5.28}$$

$$= -B_0\, m_q(2\pi^+\pi^- + \pi^0\pi^0)\ . \tag{5.29}$$

Setting

$$m_\pi^2 = 2B_0\, m_q \tag{5.30}$$

to reproduce eq. (3.24) and combining with eq. (5.26) to eliminate the coefficient B_0, we obtain the Gell-Mann-Oakes-Renner relation

$$m_\pi^2 = -\frac{1}{f_\pi^2} m_q \langle \bar{q}q\rangle_0 = -\frac{1}{2f_\pi^2}(m_u+m_d)\left\langle \bar{u}u+\bar{d}d\right\rangle_0\ , \tag{5.31}$$

which links the pion mass to the quark mass at leading order in m_q. In the chiral limit $m_u = m_d = 0$, the pion mass also vanishes.

5.3 Quark-Mass Dependence of the Nucleon Mass

The nucleon mass is affected by the explicit chiral symmetry breaking as well. Consider again the Hellmann-Feynman theorem and the one-nucleon state $|N\rangle$ as eigenstate of the QCD Hamiltonian ($\langle N\,|\,H_{\rm QCD}\,|\,N\rangle = M_N$ in the rest frame):

$$\int \mathrm{d}^3x\, \frac{\left\langle N\,\middle|\,\bar{u}u+\bar{d}d\,\middle|\,N\right\rangle}{2M_N} = \frac{\left\langle N\,\middle|\,\bar{u}u+\bar{d}d\,\middle|\,N\right\rangle(\vec{p}=0)}{2M_N} = \frac{\partial M_N}{\partial m_q}\ . \tag{5.32}$$

The factor $2M_N$ in the denominator normalizes the nucleon wave function $|N\rangle$ ($\langle N\,|\,N\rangle = 2M_N$). The integration is a Fourier transform in coordinate space with $\vec{p}=0$.

The pion-nucleon sigma term is defined as:

$$\sigma_N = \frac{\left\langle N\,\middle|\,m_q(\bar{u}u+\bar{d}d)\,\middle|\,N\right\rangle}{2M_N} = m_q\frac{\partial M_N}{\partial m_q} = m_\pi^2\frac{\partial M_N}{\partial m_\pi^2}\ , \tag{5.33}$$

where we have used in the last equality the Gell-Mann-Oakes-Renner relation eq. (5.31). It is a measure of the contribution of the quark mass to the nucleon mass:

$$M_N \simeq M_{N0} + \sigma_N + \mathcal{O}(m_q^{3/2})\ , \tag{5.34}$$

with M_{N0} the nucleon mass in the chiral limit.

The sigma term can be extrapolated from low-energy pion-nucleon scattering data. The empirical value adopted in the present calculation is [104]:

$$\sigma_N = (45\pm 8)\ \mathrm{MeV}\ . \tag{5.35}$$

Recent studies about the quark mass dependence of the nucleon mass in Lattice QCD [105] and accurate chiral extrapolations [106] show a tendency to slightly smaller values, but still consistent with that in Ref. [104] within the given errors. The large error band of the sigma term is the primary source of uncertainty in our calculation.

5.4 Scalar Quark Condensate at Finite Density

In section 5.2 we have used the Hellmann-Feynman theorem to calculate the chiral condensate in vacuum. We now employ the theorem to evaluate the chiral condensate at finite nucleon density ρ.

If the eigenstate of the Hamiltonian density $\mathcal{H}_{\rm QCD}$ is nuclear matter at density ρ, $|\rho\rangle$, one finds from (5.24):

$$\frac{\partial\epsilon(m_q)}{\partial m_q} = \left\langle \rho \left| \, \bar{u}u + \bar{d}d \, \right| \rho \right\rangle = \langle \bar{q}q \rangle (\rho) \ , \tag{5.36}$$

with ϵ the energy density of the fermionic system. Only the energy shift $\epsilon - \epsilon_0$ from the vacuum is observable. Adding and subtracting at the same time the contribution of the vacuum, the equation becomes:

$$\langle \bar{q}q \rangle (\rho) = \langle \bar{q}q \rangle_0 + \frac{\partial(\epsilon - \epsilon_0)}{\partial m_q} \ . \tag{5.37}$$

The condensate ratio between the finite-density quark condensate and the vacuum quark condensate is:

$$\begin{aligned} \frac{\langle \bar{q}q \rangle (\rho)}{\langle \bar{q}q \rangle_0} &= 1 + \frac{1}{\langle \bar{q}q \rangle_0} \frac{\partial(\epsilon - \epsilon_0)}{\partial m_q} = 1 - \frac{1}{f_\pi^2} \frac{\partial(\epsilon - \epsilon_0)}{\partial m_\pi^2} \\ &= 1 - \frac{\rho}{f_\pi^2} \frac{\partial \bar{E}(\rho)}{\partial m_\pi^2} \end{aligned} \tag{5.38}$$

with $\bar{E}(\rho)$ given by eq. (3.58).

The energy of the free Fermi gas depends on the pion mass through the nucleon mass. With $\bar{E} = \bar{E}_0 + \bar{E}_{\rm int}$ the condensate ratio takes the form [107]:

$$\begin{aligned} \frac{\langle \bar{q}q \rangle (\rho)}{\langle \bar{q}q \rangle_0} &= 1 - \frac{\rho}{f_\pi^2} \left\{ \frac{\sigma_N}{m_\pi^2} \frac{\partial \bar{E}_0}{\partial M_N} + \frac{\partial \bar{E}_{\rm int}}{\partial m_\pi^2} \right\} \\ &= 1 - \frac{\rho}{f_\pi^2} \left\{ \frac{\sigma_N}{m_\pi^2} \left(1 - \frac{3k_F^2}{10 M_N^2} \right) + \frac{\partial \bar{E}_{\rm int}}{\partial m_\pi^2} \right\} \ . \end{aligned} \tag{5.39}$$

The derivative of the interaction part $\bar{E}_{\rm int}$ gives the contribution of the pion-exchange dynamics to the condensate beyond the linear density approximation.

The extension to finite temperature is easily performed replacing the energy per particle $\bar{E}(\rho)$ by the free energy per particle $\bar{F}(\rho, T)$, eq. (4.20):

$$\frac{\langle \bar{q}q \rangle (\rho, T)}{\langle \bar{q}q \rangle_0} = 1 - \frac{\rho}{f_\pi^2} \left\{ \frac{\sigma_N}{m_\pi^2} \frac{\partial \bar{F}_0(\rho, T)}{\partial M_N} + \frac{\partial \bar{F}_{\rm int}}{\partial m_\pi^2} \right\} \ . \tag{5.40}$$

We keep in mind that the quantities f_π, g_A and M_N in the equations are taken in the chiral limit.

5.5 Calculation of the In-Medium Chiral Condensate

Eq. (5.40) links the chiral condensate to the pion-mass derivative of the free energy per particle of nuclear matter and enables its calculation. The derivatives with respect to the pion mass of the two- and three-body kernels of isospin-symmetric nuclear matter are given explicitly in Appendix C. In the following we discuss the salient points of the derivation.

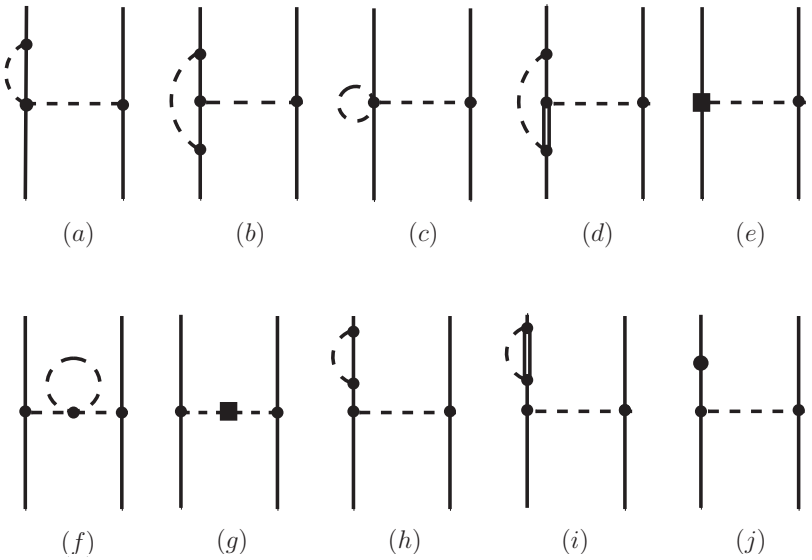

Figure 5.1: NLO diagrams that renormalize the 1π-exchange NN interaction. The diagrams (a-e) renormalize the pion-nucleon interaction vertex; diagrams (f) and (g) cause a pion-mass shift and diagrams (h-j) renormalize the nucleon mass. The small dot indicates a vertex with interaction index $\Delta = 0$. The large dot represents a vertex with $\Delta = 1$. The solid square labels a vertex with $\Delta = 2$.

5.5.1 1π-Exchange

At three-loop order in the free energy density one encounters pion-loop corrections to 1π-exchange. Such corrections have been taken into account in the calculation of the equation of state of nuclear matter using the physical value of the pion and nucleon masses and of the pion-nucleon coupling. We are now interested in their pion-mass dependence that gives rise to a non-trivial contribution to the chiral condensate.

In Fig. (5.1) we show the diagrams renormalizing the 1π-exchange at NLO. Corrections to the pion-nucleon interaction vertex come from diagrams (a-e). The diagram (a) vanishes because it involves an integration over an odd power of the loop momentum. The diagrams (b-e) generate the vertex renormalization factor

$$\begin{aligned}\Gamma(m_\pi) = 1 + \frac{g_A^2 m_\pi^2}{(2\pi f_\pi)^2}\left[4\gamma + 1 - 2\,\ln\frac{m_\pi}{\lambda}\right] + \frac{g_A^2}{3\pi^2 f_\pi^2}\left\{\frac{\pi m_\pi^3}{\Delta} - \frac{m_\pi^2}{2}\right. \\ + (3m_\pi^2 - 2\Delta^2)\ln\frac{m_\pi}{2\Delta} - \frac{2}{\Delta}(\Delta^2 - m_\pi^2)^{\frac{3}{2}}\,\ln\frac{\Delta + \sqrt{\Delta^2 - m_\pi^2}}{m_\pi} \\ + \frac{9\,g_A^2}{(4\pi f_\pi)^2}\left\{m_\pi^2 + (4\Delta^2 - 2m_\pi^2)\,\ln\frac{m_\pi}{2\Delta} + 4\Delta\sqrt{\Delta^2 - m_\pi^2}\,\ln\frac{\Delta + \sqrt{\Delta^2 - m_\pi^2}}{m_\pi}\right\}\,. \quad (5.41)\end{aligned}$$

The low-energy constant $\gamma(\lambda)$ takes care of the contribution of the diagram (e) with the d_{18}-contact term from $\tilde{\mathcal{L}}_{\pi N}^{(3)}$, responsible for the Goldberger-Treiman discrepancy. It is determined, for a given renormalization scale λ, by imposing the condition:

$$\left.\frac{g_{\pi N}}{M_N}\right|_{\rm phys} = \sqrt{\Gamma(m_\pi)}\;\frac{g_A}{f_\pi}\,. \quad (5.42)$$

As seen in eq. (C.4), the factor $\Gamma(m_\pi)$ must be applied only to the static part of the kernel $\mathcal{K}_2^{1\pi}$ for reasons of consistency [107].

The diagrams (f) and (g) produce a pion mass shift. In particular, the contact term in the diagram (g) relevant for our discussion is the l_3-term in the Lagrangian $\mathcal{L}^{(4)}_{\pi\pi}$. These diagrams generate the contribution in eq. (C.8).

The remaining diagrams (h-j) renormalize the nucleon mass and imply corrections to the pion-nucleon sigma term (5.33) because of their dependence on the pion mass. The relevant contact interactions in the diagram (j) are the two c_1-contact terms in Lagrangian (3.47). After summing all contributions, the sigma term takes the form:

$$\frac{\sigma_N}{m_\pi^2} = -4c_1 - \frac{9g_A^2 m_\pi}{64\pi f_\pi^2} + \frac{3\,c_1 m_\pi^2}{2\pi^2 f_\pi^2}\,\ln\frac{m_\pi}{\lambda} + \frac{9g_A^2}{(4\pi f_\pi)^2} \times\left\{\Delta\,\ln\frac{m_\pi}{2\Delta} + \sqrt{\Delta^2-m_\pi^2}\,\ln\frac{\Delta+\sqrt{\Delta^2-m_\pi^2}}{m_\pi}\right\}\,. \tag{5.43}$$

5.5.2 Iterated 1π-Exchange and Anomalous Term

The m_π^2-derivatives of the iterated 1π-exchange contribution and of the anomalous term do not present particular complications and are derived as shown in eqs. (C.9) and (C.10).

5.5.3 Irreducible 2π-Exchange

The calculation of the m_π^2-derivative of the three-body kernels is straightforward.

A different treatment is instead used for the two-body kernel. The latter is given in eq. (B.7) by a dispersion relation collecting the potentials of the irreducible 2π-exchange with only nucleons and with intermediate Δ-isobar excitation. Moreover, the dispersion relation is twice-subtracted and the two corresponding subtraction constants are subsumed into the B_3- and B_5-contact terms.

Concerning the m_π^2-derivative, the strategy is to evaluate the 2π-exchange with only nucleons and with intermediate Δ-excitation.

In eq. (C.12) one finds the m_π^2-derivative of the irreducible 2π-exchange with only nucleons, using the kernel eq. (8) in Ref. [80].

The two-body term from 2π-exchange with intermediate Δ-isobar divides into two classes: a dominant term scaling with Δ^{-1} and the remaining ones with a more complicated dependence on Δ. The dominant term eq. (C.16) is evaluated from the one-loop NN scattering amplitudes proportional to Δ^{-1} in Ref. [52]. The remaining two-body terms are worked out by means of the dispersion relation technique. The derivative of eq. (B.7) takes the form:

$$\frac{\partial\,\mathcal{K}_2^{\Delta F'}(p_1,p_2)}{\partial m_\pi^2} = -\frac{1}{m_\pi}\,f(p_1,p_2,\mu=2m_\pi,m_\pi) + \int_{2m_\pi}^{\infty}\mathrm{d}\mu\,\frac{\partial f(p_1,p_2,\mu,m_\pi)}{\partial m_\pi^2}\,, \tag{5.44}$$

where $f(p_1,p_2,\mu,m_\pi)$ is the integrand of the spectral integral in eq. (B.7). The first term comes from the m_π-dependence of the interval of integration and it vanishes once we exclude the terms proportional to Δ^{-1}, eqs. (B.17) and (B.20), and those coming from the diagrams with only nucleons, eqs. (B.12) and (B.13). This cancelation furnishes a further motivation to treat them separately. The resulting contribution is reported in eq. (C.18). Note that its spectral function is now stabilized at high momenta by only one subtraction, which gives rise to a subtraction constant linear in the density with a quark-mass dependence. Its m_π^2-derivative is given in eq. (C.19).

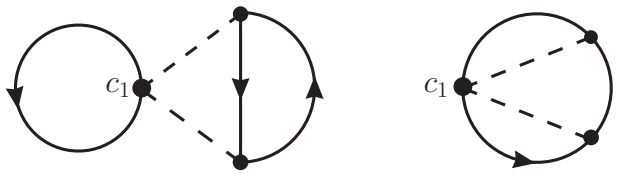

Figure 5.2: 2π-exchange Hartree and Fock diagrams involving one $\pi\pi NN$-contact vertex, with combinatoric factors respectively 1/2 and 1. These diagrams are negligible for the calculation of the free energy of nuclear matter, because they belong to NNLO, but when taking the m_π^2-derivative they give a contribution of importance similar to the others.

5.5.4 $\pi\pi NN$-contact vertex

One of the two c_1-terms in the Lagrangian (3.47) generates a $\pi\pi NN$-contact interaction, that on one hand modifies the sigma term through a pion-loop correction to the 1π-exchange scattering (as discussed in Sec. 5.5.1), and on the other hand gives rise to additional 2π-exchange diagrams, shown in Fig. 5.2. Their contribution to the free energy density is negligible, being at NNLO, but becomes sizable when taking its m_π^2-derivative.

5.5.5 Short-distance interaction

In Sec. 3.5.3 we have explained how the unresolved short-distance interaction in isospin-symmetric nuclear matter is encoded in three contact terms with coefficients proportional to B_3, B_5 and ζ. The B_3- and B_5-contact terms include also the two subtraction constants that appear in the dispersion relation (B.7). The quark mass dependence of the latter has been discussed in Sec. 5.5.3. Concerning the residual short-distance physics encoded in the contact terms, we refer to recent lattice QCD results [108, 109], where a negligibly small quark-mass dependence of the short-distance NN interaction, compared to the intermediate- and long-range attraction, has been found [107].

5.5.6 Parameters in the Chiral Limit

The input parameters of the calculation are taken in the chiral limit.
The chiral limit of the pion decay constant is extracted through the relation:

$$f_{\pi,\mathrm{phys}} = f_\pi \left[1 + \bar{l}_4 \left(\frac{m_\pi}{4\pi f_\pi}\right)^2\right] = 92.4 \text{ MeV} , \tag{5.45}$$

where $\bar{l}_4$ is a low-energy constant present in $\mathcal{L}_{\pi\pi}^{(4)}$ [110]. Using the central value of $\bar{l}_4 = 4.4 \pm 0.2$ in Ref. [111], one gets $f_\pi = 86.5$ MeV.

From the chiral extrapolation of lattice data in Ref. [112], we take $g_A = 1.224$ in the chiral limit; in a similar analysis [113], $M_N = 882$ MeV and $c_1 = -0.93$ GeV^{-1} have been found.

The parameter γ that appears in eq. (5.41) and accounts for the Goldberger-Treiman discrepancy is determined through eq. (5.42). Using $g_{\pi N}/M_N|_{\mathrm{phys}} = 13.2/939$ MeV^{-1}, we obtain $\gamma = -1.505$ at the renormalization scale $\lambda = M_N$.

The pion-loop correction to the pion mass is given by [111]:

$$m_{\pi,\mathrm{phys}} = m_\pi \left[1 - \frac{\bar{l}_3}{2}\left(\frac{m_\pi}{4\pi f_\pi}\right)^2\right] , \tag{5.46}$$

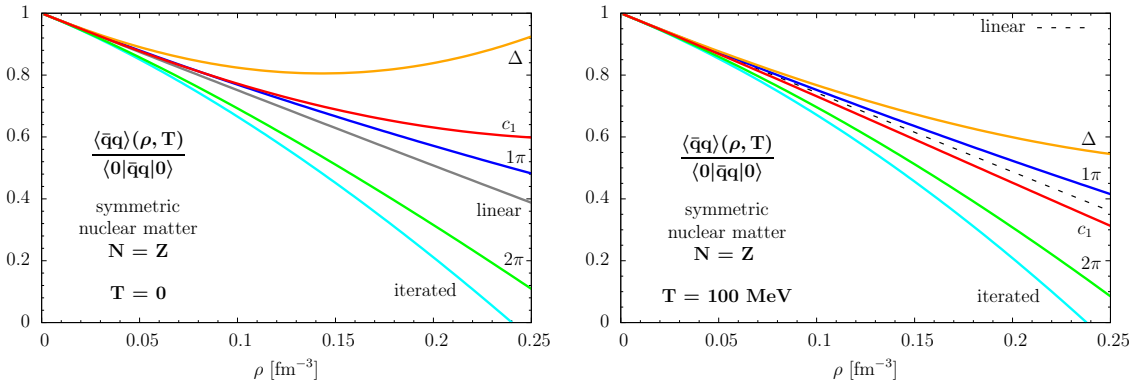

(a) $T = 0$. (b) $T = 100$ MeV.

Figure 5.3: Interaction contributions to the ratio between the in-medium chiral condensate and the vacuum condensate at $T = 0$ (left plot) and at $T = 100$ MeV (right plot). Stepwise the following contributions are added to the linear density term: 1π-exchange, iterated 1π-exchange, 2π-exchange with only nucleons, 2π-exchange with Δ-excitation, c_1-contact term.

with $m_\pi \equiv 2B_0 m_q$ (eq. (5.30)) and $\bar{l}_3 \simeq 3$. Because the difference between $m_{\pi,\text{phys}}$ and m_π is much smaller then the mass splitting between the charged and the neutral pion, we neglect it and use $m_\pi = 135$ MeV in the calculation.

With this set of parameters inserted in eq. (5.43), we obtain $\sigma_N = 44.3$ MeV at the physical pion mass. We recall that the empirical sigma term is $\sigma_N = (45 \pm 8)$ MeV [104]. Small differences may result from some residual dependence on the renormalization scale λ not balanced by the parameters $l_3^r(\lambda)$ in eq. (C.8) and $\gamma(\lambda)$. However, a large variation of the scale λ produces relatively small changes on the chiral condensate at the density ρ_0 of normal nuclear matter [107], anyway smaller than those induced by the large uncertainty of the empirical σ_N, and so we rely on the choice $\lambda = 882$ MeV.

5.6 In-Medium Chiral Condensate

We are now able to evaluate numerically the in-medium chiral condensate at finite temperature. We explore the range of densities $0 \leq \rho \lesssim 2\rho_0$ for temperatures $T \lesssim 100$ MeV [103].

First of all, we study the relative importance of the different interaction contributions to the condensate ratio $\langle \bar{q}q \rangle (\rho, T) / \langle \bar{q}q \rangle_0$ between the in-medium chiral condensate and its vacuum value. In Fig. 5.3, the interaction contributions are displayed stepwise for the case of temperature zero (on the left) and for the limit of large temperature $T = 100$ MeV (on the right). Starting from the linear density approximation, i.e. the contribution of the non-interacting Fermi gas, the interaction effects coming from pion-exchange dynamics are added in the following order: 1π-exchange, iterated 1π-exchange, irreducible 2π-exchange with only nucleons, irreducible 2π-exchange with Δ-excitation, 2π-exchange with c_1-contact term. At $T = 0$ one notes immediately the fundamental role played by the Δ-isobar degree of freedom. If we had taken into account only 1π-exchange and 2π-exchange dynamics without Δ-excitation, the condensate would melt rapidly, already at densities $\rho \lesssim 2\rho_0$, in the nuclear matter terrain of the QCD phase diagram. The inclusion of the Δ-isobar as an explicit degree of freedom has the consequence of largely counteracting the decrease of the condensate, actually delaying its melting significantly and stabilizing it. With the increase of temperature, the effect of the interactions weakens gradually. In particular, the

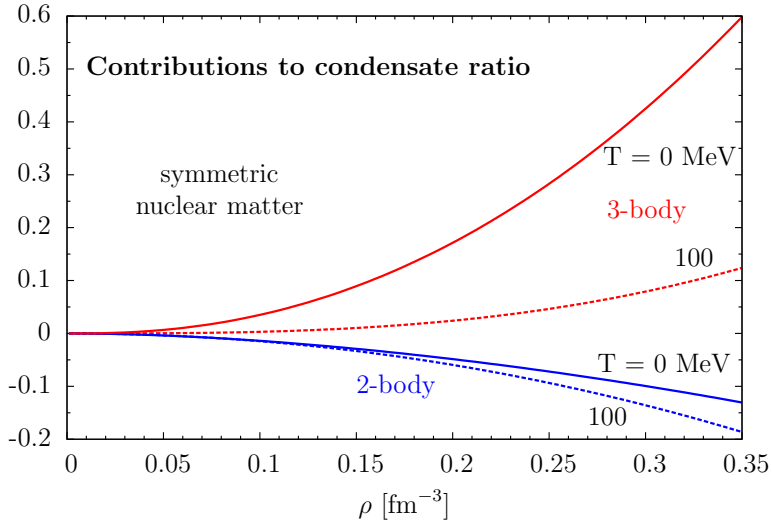

Figure 5.4: Two-body and three-body interaction contributions to the condensate ratio for the limit cases of $T = 0$ and $T = 100$ MeV. Three-body contributions are strongly dependent on temperature.

Δ-isobar contribution appears to have a strong dependence on temperature. At $T = 100$ MeV, the amplitude of the corresponding curve is visibly reduced and the linear behaviour characteristic of a Fermi gas tends to be restored.

Such behaviour of the interactions with temperature is better observed if we group the interaction contributions into a two-body part, that we indicate shortly as $\mathcal{K}_2$, and a three-body part, labeled with $\mathcal{K}_3$, as it has been done in Fig. 5.4. One notes that the $\mathcal{K}_3$ curve (red line) has the opposite behaviour of that of $\mathcal{K}_2$ (blue line). While $\mathcal{K}_2$ works in favour of the decrease of the condensate, $\mathcal{K}_3$ counteracts instead its reduction. At $T = 0$ the three-body contribution is large and grows rapidly with density. Comparing with the curve at $T = 100$ MeV one deduces that the three-body medium-effects are strongly dependent on temperature. On the other hand, temperature has a weak influence on the two-body term. At $T = 100$ MeV the three-body contribution is largely reduced such that it almost balances with $\mathcal{K}_2$. As a result, the non-interacting Fermi gas governs the behaviour of the condensate.

Fig. 5.5 shows systematically the variation of the condensate ratio with nucleon density and temperature up to $T = 100$ MeV [103]. The considerations previously made apply to the situation depicted by this figure. At low temperature, because of the action of the Δ-isobar, the condensate becomes stable at large density. With increasing temperature, the linear density behaviour of the non-interacting Fermi gas is tendentially restored. The numerical calculation shows that such curves do not cross the zero below a density of $2\rho_0$. This has to be regarded as a rough estimate. Once the condensate becomes too small, the fundamental condition that justifies the chiral effective field theory approach, i.e. the spontaneous chiral symmetry breaking, becomes obsolete. For this reason we restrict the plot to the range of density $0 \leq \rho \leq 1.6\,\rho_0$, inside of which the results are reliable. Other calculations [53, 114], that do not include 2π-exchange dynamics with explicit Δ-isobar excitation, do not show a trend of stabilization, emphasizing the importance of the Δ-isobar for a proper description of the chiral condensate.

The chiral condensate exhibits yet another important feature. The Maxwell construction prescribes a linear behaviour of the condensate at a given temperature when the liquid-gas

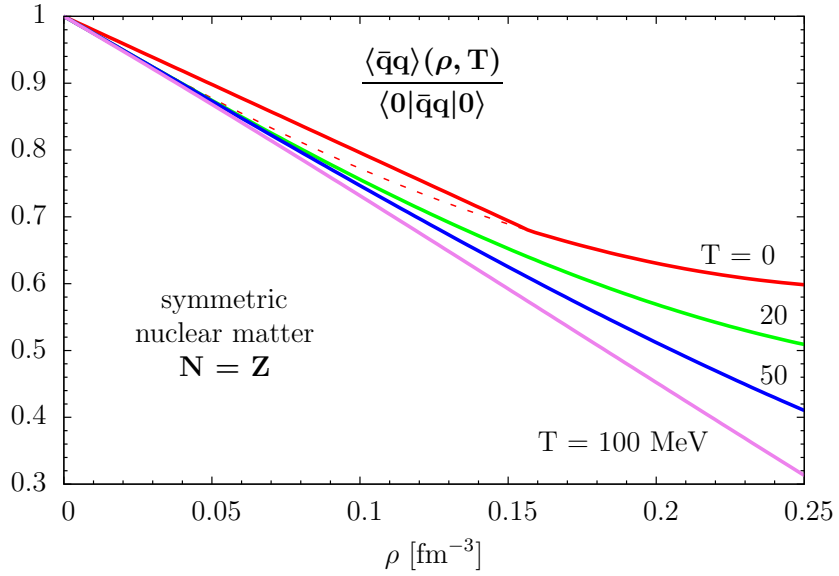

Figure 5.5: Condensate ratio as a function of the baryon density for different values of temperature [103]. The trace of the first-order liquid-gas phase transition is visible on the red line, corresponding to $T = 0$. The dashed-line indicates the non-physical behaviour of the condensate in the liquid-gas coexistence region. The physical condensate (linear solid line) is obtained using the Maxwell construction.

phase transition occurs in nuclear matter, as it can be seen in the curve at $T = 0$ (red line) of Fig. 5.5. The dashed line represents the non-physical behaviour of the condensate in the liquid-gas coexistence region. While the liquid-gas phase transition shows itself in the straight linear behaviour of the ratio $\langle\bar{q}q\rangle(\rho,T)/\langle\bar{q}q\rangle_0$ at low temperature ($T \lesssim 15$ MeV) when plotted as a function of the baryon density, the occurrence of a first-order phase transition becomes manifest if one investigates the condensate as a function of the baryon chemical potential, as in Fig. 5.6. The discontinuity of the condensate ratio in the chemical potential μ is characteristic of the first-order liquid-gas phase transition. In a finite system the sharp discontinuity would be replaced by a smoother crossover.

Last we incorporate the effects of thermal pions. They give rise to a further reduction of the condensate depending on temperature. The modifications of the $\pi\pi$ interaction at finite temperature to the chiral condensate have been calculated at two-loop order in ChPT, where only factorizable diagrams have been taken into account [115]. The resulting shift of the condensate ratio reads:

$$\frac{\delta\langle\bar{q}q\rangle(T)}{\langle\bar{q}q\rangle_0} = -\frac{3m_\pi^2}{(2\pi f_\pi)^2}\,h_3\Big(\frac{m_\pi}{T}\Big)\left\{1+\frac{m_\pi^2}{8\pi^2 f_\pi^2}\left[h_3\Big(\frac{m_\pi}{T}\Big)-h_1\Big(\frac{m_\pi}{T}\Big)+\frac{2-3\,\bar{l}_3}{8}\right]\right\}\,, \quad (5.47)$$

with the functions $h_1(y)$ and $h_3(y)$ defined by integrals over the Bose distribution function:

$$h_1(y) = \int_y^\infty \frac{\mathrm{d}x}{\sqrt{x^2-y^2}(e^x-1)}\,, \qquad h_3(y) = \frac{1}{y^2}\int_y^\infty \mathrm{d}x\,\frac{\sqrt{x^2-y^2}}{e^x-1}\,. \quad (5.48)$$

In Fig. 5.7 we show the temperature dependence of the Gell-Mann-Oakes-Renner relation, eq. (5.31), at zero baryon density. The ratio between the chiral condensate of the pionic heat bath to its $T = 0$ value $\langle\bar{q}q\rangle(T)/\langle\bar{q}q\rangle_0$ is plotted as a function of temperature for different values of the pion mass. This ratio reflects the corresponding behaviour of the product $m_\pi^2 f_\pi^2$ in the thermal pionic environment. In the chiral limit ($m_\pi = 0$) the decrease

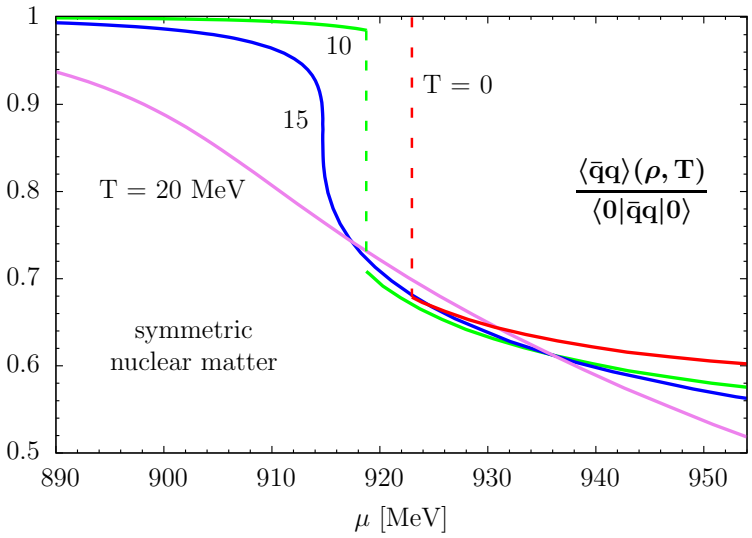

Figure 5.6: Ratio of the condensate to its vacuum value plotted as a function of the baryon chemical potential [103]. The gap at low temperature is characteristic of the liquid-gas coexistence first-order phase transition.

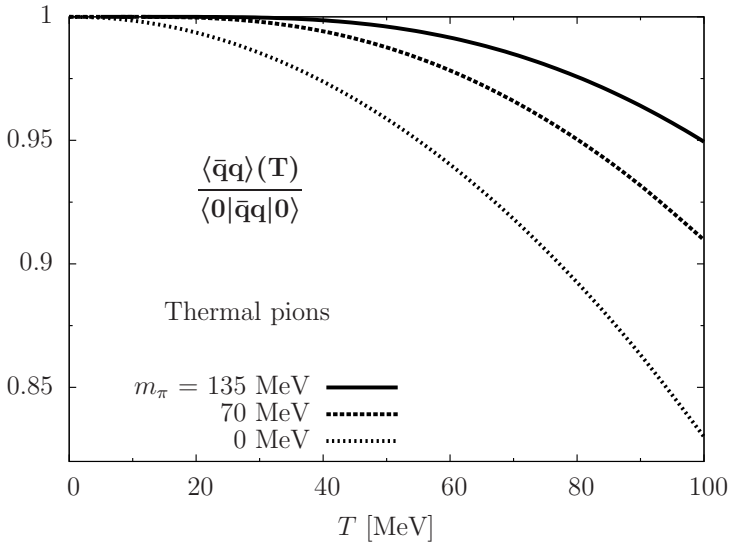

Figure 5.7: Temperature dependence of the Gell-Mann-Oakes-Renner relation in eq. (5.31). The ratio between the condensate of the thermal pionic bath to its $T = 0$ value is plotted as a function of temperature. The pion mass dependence is also investigated. In the chiral limit the condensate decreases faster than at the physical pion mass $m_\pi = 135$ MeV.

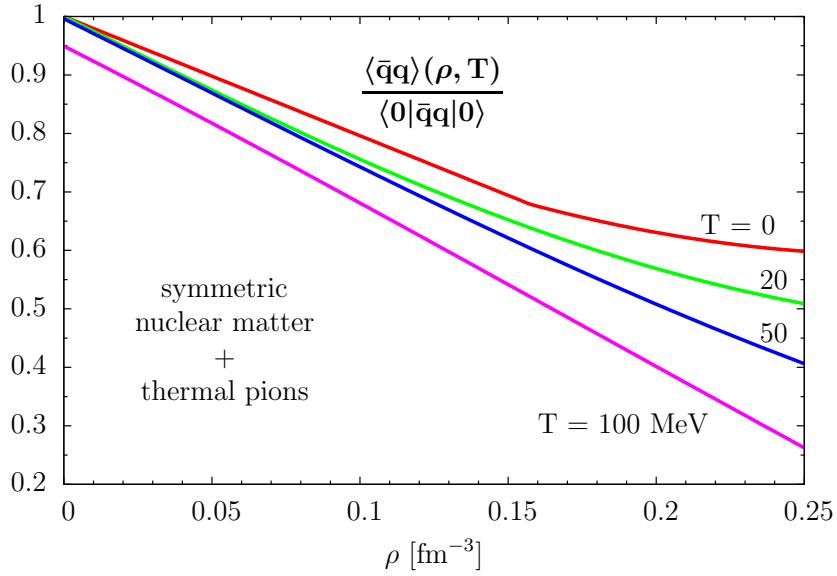

Figure 5.8: Ratio of the chiral condensate to its vacuum value with the inclusion of the thermal pions as a function of baryon density at different temperatures [103]. The plot excludes the chiral symmetry restoration in the nuclear matter sector of the QCD phase diagram.

of the condensate proceeds considerably faster with temperature than at physical pion mass. The explicit chiral symmetry breaking delays the melting of the condensate.

Finally, in Fig. 5.8 we add the contribution of the pionic heat bath, eq. (5.47), to the chiral condensate in symmetric nuclear matter, eq. (5.40). The condensate at zero density begins to deviate appreciably from its vacuum value at high temperature ($T \gtrsim 80$ MeV). We conclude that there is no indication of a first-order chiral phase transition for densities $0 \leq \rho \lesssim 2\rho_0$ and at temperature $T \lesssim 100$ MeV. This result sets important constraints for the location of the chiral transition in the QCD phase diagram.

Before closing the present section, we mention that a calculation of the chiral condensate in pure neutron matter in the framework of in-medium chiral perturbation theory has also been performed [116]. Due to the reduced isospin factors of 2π-exchange dynamics, only small deviations from the linear decrease of the in-medium condensate have been found.

5.7 In-Medium Quark Condensate in the Chiral Limit

Because the pion mass m_π appears as an explicit parameter in the calculation, we are able to investigate the chiral limit of the in-medium condensate. The scenario suggested by the condensate in the chiral limit is very different from the real world.

As one can see in Fig. 5.9, the Δ-isobar plays no special role in determining the behaviour of the condensate in this limit. Its counteraction to the dropping of the condensate is small at zero temperature and, paradoxically, it turns out to considerably reduce the condensate at large temperature. We conclude that the action of the Δ-isobar on the condensate is substantially dependent on the pion mass.

In a similar way, the interplay between two-body and three-body interaction contributions changes in the chiral limit. In Fig. 5.10, at low temperature, $\mathcal{K}_2$ and $\mathcal{K}_3$ are very large with a slight predominance of the former. They both reduce with temperature, but the relative importance of $\mathcal{K}_2$ compared to $\mathcal{K}_3$ grows as T increases. So we deduce that medium

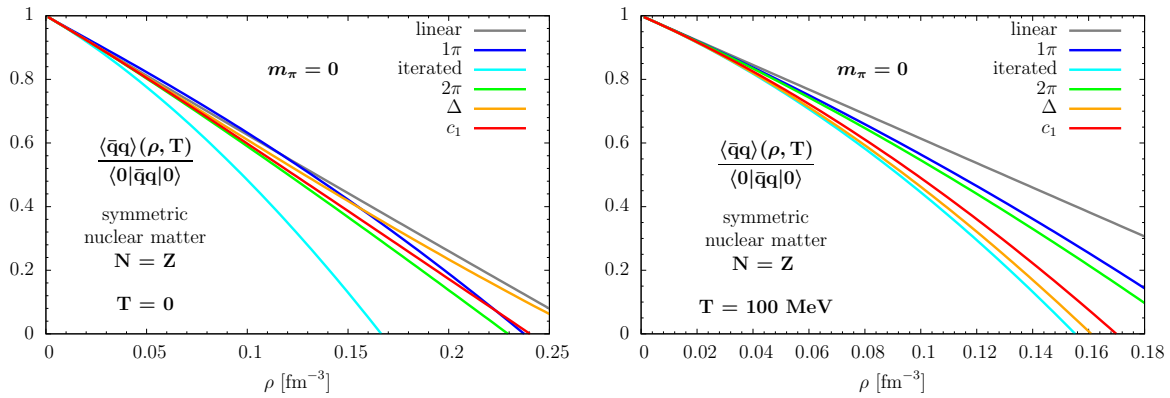

(a) $T = 0$. (b) $T = 100$ MeV.

Figure 5.9: Chiral limit: interaction contributions to the ratio between the in-medium chiral condensate and the vacuum condensate at $T = 0$ (left plot) and at $T = 100$ MeV (right plot). Stepwise the different contributions are added in the order displayed in the legend.

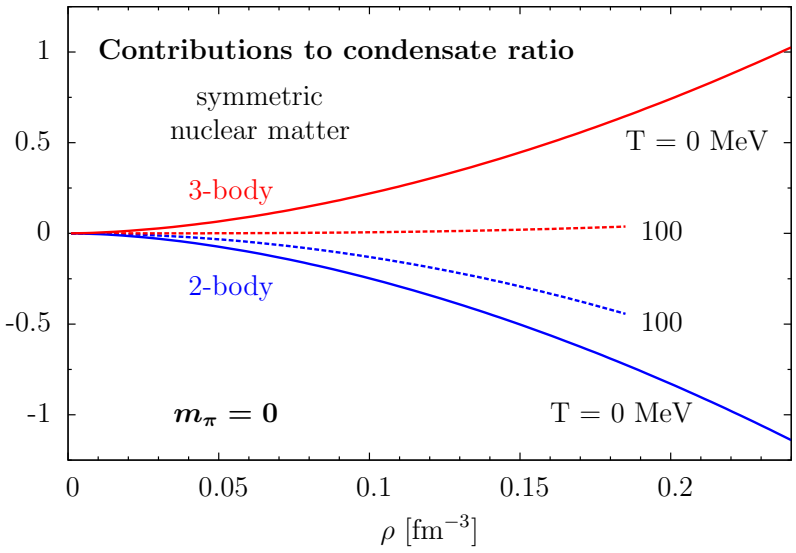

Figure 5.10: Chiral limit: Two-body and three-body interaction contributions to the condensate ratio for cases of $T = 0$ and $T = 100$ MeV.

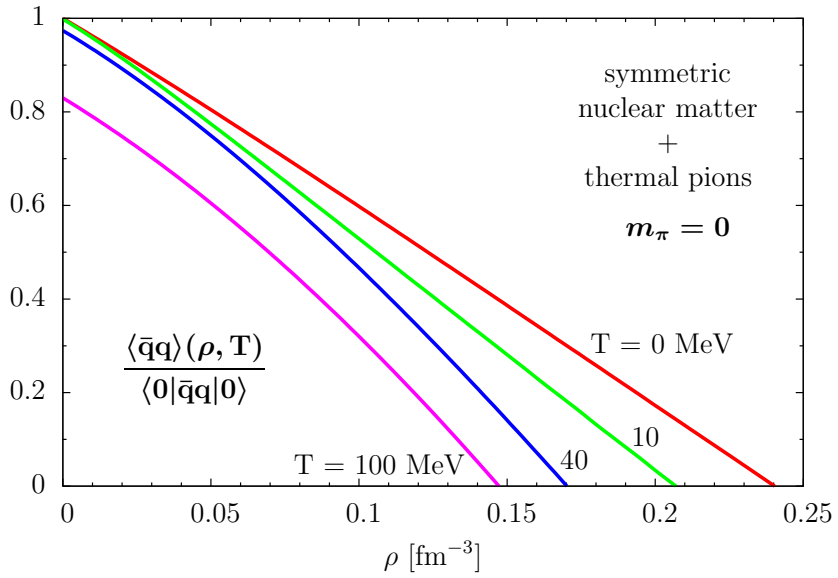

Figure 5.11: Chiral limit: ratio of the chiral condensate to its vacuum value with the inclusion of thermal pions as a function of baryon density at different temperatures.

effects are enhanced by the finiteness of the pion mass.

Consequently, the emerging scenario in the chiral limit with $m_\pi = 0$, after summing all contributions, is drastically different from that in Fig. 5.8 at the physical pion mass. In Fig. 5.11 the condensate drops to zero quickly and melts already at a density of $1.5\,\rho_0$ at $T = 0$. At high temperature the chiral transition takes place around the normal saturation density ρ_0.

As previously pointed out for the pionic thermal bath, the explicit chiral symmetry breaking delays the transition to the restoration of chiral symmetry in its Wigner-Weyl mode, shifting it beyond at least twice the saturation density of normal nuclear matter. Medium effects and the role played by the Δ-isobar excitation depend crucially on explicit chiral symmetry breaking.

Chapter 6

In-Medium Resummations

The equation of state of nuclear matter obtained using in-medium ChPT has a well-known problem at low densities, $\rho \lesssim 0.05\,\mathrm{fm}^{-3}$, which becomes more prominent in neutron rich matter. The neutron-neutron scattering is the simplest example of a process with a large scattering length, $a \simeq 19$ fm. The large magnitude of a, compared with the typical range of the interaction, invalidates the usual expansion in powers of the soft momenta of the $\mathcal{T}$-matrix. This problem is treated by a resummation to all orders of the S-wave contact interaction. The resummation is now extended to the nuclear medium using the in-medium nucleon propagator defined in section 3.5.

The spin-triplet (isospin-singlet) channel of NN scattering has a scattering length $a_t \simeq -5.42$ fm. The spin-singlet consists of three states with isospin $I = 1$. If we neglect the isospin-breaking effects - such as the mass difference between proton and neutron and the electromagnetic interaction - NN interaction is isospin invariant and the three states with $I = 1$ have the same scattering length. According to recent measurements [117, 118], the neutron-neutron scattering length is $a_{nn} = (18.95 \pm 0.40)$ fm. We take this result as representative of the scattering length of the spin-singlet states: $a_s \simeq 19$ fm.

6.1 Unitary Fermi Systems

The scattering of two particles at low energy is determined by its S-wave scattering length a. Low energy means that the corresponding de-Broglie wavelength is much larger than the range of the interaction. In this situation the scattering properties depend primarily on a.

To define in a rigorous way the limit just described, we introduce the concept of naturalness of a scale. The pion-exchange in the NN scattering sets the characteristic distance scale of the interaction, $r \sim 1/m_\pi \sim 1.5$ fm. This is also called *natural* low-energy *length scale*. If the scattering length a is of the same order of magnitude as r, i.e. $|a| \sim r$, then a is said to have *natural size*. On the contrary, if a is much larger than r, i.e. $|a| \gg r$, it is said to be *unnaturally large*.

If we consider the low-energy regime of NN scattering corresponding to momenta much smaller than the pion mass, i.e. $p \ll m_\pi \simeq 135$ MeV, the pionic degrees of freedom are integrated out and the pion exchange reduces to a contact interaction.

If the system under consideration is dilute, i.e. the mean interparticle separation is much larger than the range of the interaction r, then the system becomes insensitive to the particular form of the short-range interaction and is called *universal*. Its properties are determined just by the scattering length a.

It may happen that the scattering length of a universal system is unnaturally large, $|a| \gg r$, and therefore, is integrated out of the problem. Such a system is called *unitary*. In a Fermi system, the only scale we are left with to characterize the problem is the Fermi

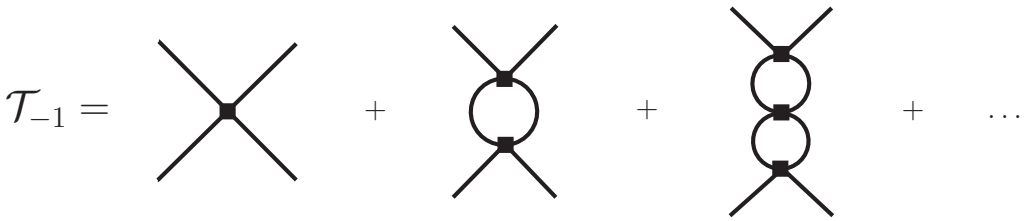

Figure 6.1: The bubble-chain resummation is able to reproduce the term of order $\mathcal{O}(p^{-1})$ in the non-perturbative expansion of the $\mathcal{T}$-matrix when the scattering length a is large.

momentum k_F. Observables, such as the energy per particle, will depend in this limit only on k_F:

$$\bar{E}(k_F) = \xi \, \frac{3\, k_F^2}{10\, M} \ , \tag{6.1}$$

with ξ the Bertsch parameter. Because the scattering length of the spin-singlet state of a two-nucleon system is large, $a_s \simeq 19\,\mathrm{fm} \gg r \sim 1.5$ fm, it is expected that neutron matter at low density, $\rho \lesssim 0.05\,\mathrm{fm}^{-3}$, resembles the behaviour of the unitary Fermi gas.

6.2 Momentum Expansion of the $\mathcal{T}$-Matrix and Resummation

The large scattering length a_s is at the origin of the breakdown of the $\mathcal{T}$-matrix perturbative expansion in NN scattering at low energy, where the S-wave contribution dominates. This $\mathcal{T}$-matrix is:

$$\mathcal{T} = \frac{4\pi}{M_N} \frac{1}{p \cot\delta - ip} \ , \tag{6.2}$$

with p the particle momentum in the center-of-mass frame and δ the S-wave phase shift.

Usually, $p\cot\delta$ is expanded in powers of p/m_π, with $p \ll m_\pi$:

$$p\cot\delta = a^{-1} + \frac{1}{2}\, m_\pi^2 \sum_{n=0}^{\infty} r_n \left(\frac{p^2}{m_\pi^2}\right)^{n+1} \ . \tag{6.3}$$

At order p^2, this expansion defines the scattering length a and the effective range r_0:

$$p\cot\delta = \frac{1}{a} + \frac{1}{2}\, r_0\, p^2 + \ldots \tag{6.4}$$

The coefficients $|r_n|$ have generally a natural size so that they are bounded from above by the range of the interaction. Instead, a can assume any value.

We discuss now the momentum expansion of the $\mathcal{T}$-matrix in the two limiting cases for the size of a. First consider the familiar case of naturalness of a, i.e. $a \sim 1/m_\pi$. The $\mathcal{T}$-matrix can then be expanded in powers of p/m_π:

$$\mathcal{T} = \frac{4\pi a}{M_N} \left[1 + iap - \left(\frac{ar_0}{2} + a^2\right) p^2 + \mathcal{O}\left(\frac{p^3}{m_\pi^3}\right)\right] . \tag{6.5}$$

This expansion is well defined because $ap \ll 1$, and it is convergent up to momenta $p \sim m_\pi$. In an EFT the expansion (6.5) corresponds to a perturbative sum of Feynman diagrams.

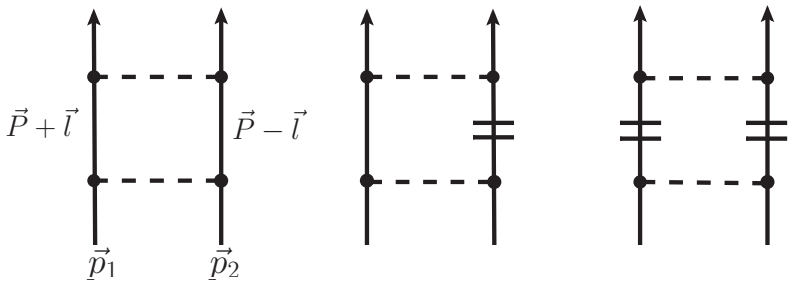

Figure 6.2: The in-medium loop integral consists of contributions with zero, one and two medium insertions, represented in the diagrams by the two lines transverse to the nucleon propagator. The particle momenta are inside the Fermi sphere, $|p_{1,2}| < k_F$. $\vec{P} = (\vec{p}_1 + \vec{p}_2)/2$ is the average momentum. Dashed lines represent contact interactions.

If a is unnaturally large, $|a| \gg 1/m_\pi$, the previous expansion breaks down for momenta $p \gtrsim 1/|a|$. This problem is overcome by keeping the large term ap to all orders in the expansion:

$$\mathcal{T} = \frac{4\pi}{M_N}\frac{1}{a^{-1}-ip}\left\{1 - \frac{r_0}{2}\frac{1}{(a^{-1}-ip)^2}\,p^2 + \left[\left(\frac{r_0}{2}\right)^2\frac{1}{(a^{-1}-ip)^2} - \frac{r_1}{2m_\pi^2}\frac{1}{a^{-1}-ip}\right]p^4 + \mathcal{O}(p^6)\right\} \ . \quad (6.6)$$

We note that the leading term in $\mathcal{T}$ is of order $\mathcal{O}(p^{-1})$ and arises from the resummation of the non-perturbative effects induced by the large size of the product ap. A leading term of such a form can be reproduced in an EFT of low-energy NN interaction by summing the leading four-nucleon contact term proportional to C_S in eq. (3.42) to all orders, as shown in Fig. 6.1. As a result of the resummation, the constant C_S turns out to be scale-dependent and can be matched with the scattering length a. This important feature has been pointed out in Ref. [50].

6.3 In-Medium Resummation of Ring Diagrams

The resummation of the S-wave NN contact interaction is now performed in neutron matter using the formalism developed in section 3.5. The inclusion of the non-perturbative short-range effects is expected to improve the behaviour of the equation of state, especially at low density $\rho \lesssim 0.05\,\mathrm{fm}^{-3}$. The technique for the ring diagram resummation in neutron matter has been developed in Ref. [57] that we follow here.

We use the in-medium nucleon propagator eq. (3.56) and take from the beginning the non-relativistic limit:

$$S_N(p_0,\vec{p}) = \frac{i}{p_0 - \vec{p}^{\,2}/(2M_N) + i\epsilon} - 2\pi\,\delta\left(p_0 - \frac{\vec{p}^{\,2}}{2M_N}\right)\theta(k_F - |\vec{p}|) \ . \quad (6.7)$$

Consider the chain of ladder diagrams describing the NN scattering. For a contact interaction the loop integrals factorize. A ladder diagram with n loops is equivalent to the $n-1$-th iteration of the basic loop integral.
At tree-level the NN transition amplitude is trivially $4\pi a/M_N$.

At the successive order we have to evaluate the one-loop diagram in Fig. 6.2. We introduce the average momentum $\vec{P} = (\vec{p}_1 + \vec{p}_2)/2$ and the difference $\vec{q} = (\vec{p}_1 - \vec{p}_2)/2$ for

convenience. Normalized to the tree-level amplitude, the loop integral to evaluate is:

$$L = \frac{4\pi a\, i}{M_N} \int \frac{\mathrm{d}^4 l}{(2\pi)^4} \left[\frac{i}{\frac{E}{2} + l_0 - \frac{(\vec{P}+\vec{l})^2}{2M_N} + i\epsilon} - 2\pi\, \delta\!\left(\frac{E}{2} + l_0 - \frac{(\vec{P}+\vec{l})^2}{2M_N} \right) \theta(k_F - |\vec{P}+\vec{l}|) \right] \cdot \left[\frac{i}{\frac{E}{2} - l_0 - \frac{(\vec{P}-\vec{l})^2}{2M_N} + i\epsilon} - 2\pi\, \delta\!\left(\frac{E}{2} - l_0 - \frac{(\vec{P}-\vec{l})^2}{2M_N} \right) \theta(k_F - |\vec{P}-\vec{l}|) \right] , \quad (6.8)$$

where $E = (\vec{p}_1^{\,2} + \vec{p}_2^{\,2})/(2M_N)$ is the energy of the system. The in-medium loop integral consists of contributions with zero, one and two medium insertion, as showed in Fig. 6.2.

6.3.1 Vacuum Diagram

The contribution of the diagram with no medium insertion is:

$$\begin{aligned} L_0 &= \frac{4\pi a\, i}{M_N} \int \frac{\mathrm{d}^4 l}{(2\pi)^4} \frac{i}{\frac{E}{2} + l_0 - \frac{(\vec{P}+\vec{l})^2}{2M_N} + i\epsilon} \frac{i}{\frac{E}{2} - l_0 - \frac{(\vec{P}-\vec{l})^2}{2M_N} + i\epsilon} \\ &= 4\pi a \int \frac{\mathrm{d}^3 l}{(2\pi)^3} \frac{1}{\vec{l}^{\,2} - \vec{q}^{\,2} - i\epsilon} = \frac{2\pi}{a} \int_0^\infty \mathrm{d}l\, \frac{l^2}{l^2 - q^2 - i\epsilon} \\ &= \frac{2a}{\pi} \int_0^\infty \mathrm{d}l \left[1 + \frac{q^2}{l^2 - q^2 - i\epsilon} \right] = iaq \, , \end{aligned} \quad (6.9)$$

with $q = |\vec{q}|$. We have performed the integration in $\mathrm{d}l_0$ by the residue theorem and used the property $\int \mathrm{d}l\, 1 = 0$ in dimensional regularization; finally, the residue theorem is again used to carry out the integration in $\mathrm{d}l$.

The result is imaginary. The resummation to all orders of L_0 generates a power series in iaq corresponding to the momentum expansion in eq. (6.6).

6.3.2 One Medium Insertion

After the integration in $\mathrm{d}l_0$ one gets rid of the delta function and finds:

$$\begin{aligned} L_1 &= -4\pi a \int \frac{\mathrm{d}^3 l}{(2\pi)^3} \frac{1}{\vec{l}^{\,2} - \vec{q}^{\,2} - i\epsilon} \left[\theta(k_F - |\vec{P}-\vec{l}|) + \theta(k_F - |\vec{P}+\vec{l}|) \right] \\ &= -8\pi a \int \frac{\mathrm{d}^3 l}{(2\pi)^3} \frac{1}{\vec{l}^{\,2} - \vec{q}^{\,2} - i\epsilon} \theta(k_F - |\vec{P}-\vec{l}|) \\ &= -\frac{a}{\pi} \int_{-1}^{1} \mathrm{d}\cos\theta \int_0^{l_{\mathrm{up}}} \mathrm{d}l\, \frac{l^2}{l^2 - q^2 - i\epsilon} \, . \end{aligned} \quad (6.10)$$

The integration in $\mathrm{d}^3 l$ is carried out in spherical coordinates. In Fig. 6.3 one can see the integration region in momentum space. Applying simple trigonometric rules, we find the upper integration limit l_{up}:

$$l_{\mathrm{up}} = Py + \sqrt{k_F^2 - P^2(1-y^2)} \, , \qquad y = \cos\theta \, , \qquad P = |\vec{P}\,| \, . \quad (6.11)$$

The real part of the loop integral L_1 is:

$$\mathrm{Re}\, L_1 = -\frac{a k_F}{\pi} R(s,k) \, , \quad (6.12)$$

$$R(s,k) = 2 + \frac{1}{2s} \left\{ \left[1 - (s+k)^2 \right] \ln \frac{1+s+k}{|1-s-k|} + \frac{1}{2s} \left[1 - (s-k)^2 \right] \ln \frac{1+s-k}{1-s+k} \right\} \, , \quad (6.13)$$

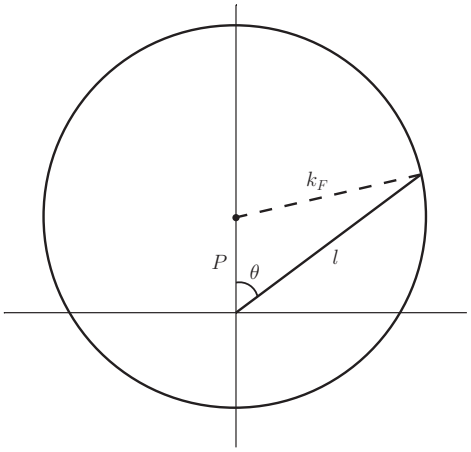

Figure 6.3: Region of integration of the real part of the loop integral with one medium insertion eq. (6.10).

with

$$s = \frac{|\vec{P}|}{k_F} \,, \qquad k = \frac{|\vec{q}|}{k_F} \,, \qquad 0 \leqslant s, k \leqslant 1 \,, \qquad s^2 + k^2 \leqslant 1 \,. \tag{6.14}$$

6.3.3 Imaginary Part

The imaginary part of the loop integral (6.8) can be evaluated with the help of the optical theorem in Quantum Field Theory. The imaginary part of a Feynman diagram is related to its discontinuity by a factor $1/(2\,i)$. According to the optical theorem, one derives the discontinuity of the Feynman diagram replacing the (vacuum) propagator with a delta function:

$$\frac{1}{p_0 - \vec{p}^{\,2}/(2M_N) + i\epsilon} \longrightarrow -2\pi i\,\delta\!\left(p_0 - \frac{\vec{p}^{\,2}}{2M_N}\right) \,. \tag{6.15}$$

After performing this substitution in eq. (6.8), we find:

$$\begin{aligned} \mathrm{Im}\, L = \frac{2\pi a}{M_N} \int \frac{\mathrm{d}l^4}{(2\pi)^4}\, (2\pi)^2\, \delta\left(\frac{E}{2} + l_0 - \frac{(\vec{P}+\vec{l}\,)^2}{2M_N}\right) \delta\left(\frac{E}{2} - l_0 - \frac{(\vec{P}-\vec{l}\,)^2}{2M_N}\right) \\ \Big\{\Big[1 - \theta(k_F - |\vec{P}+\vec{l}\,|)\Big]\,\Big[1 - \theta(k_F - |\vec{P}-\vec{l}\,|)\Big] \\ + \theta(k_F - |\vec{P}+\vec{l}\,|)\,\theta(k_F - |\vec{P}-\vec{l}\,|)\Big\} \,. \end{aligned} \tag{6.16}$$

We carry out the integration in $\mathrm{d}l_0$:

$$\begin{aligned} \mathrm{Im}\, L = 4\pi^2 a \int \frac{\mathrm{d}l^3}{(2\pi)^3}\, \delta(\vec{l}^{\,2} - \vec{q}^{\,2})\, \Big\{\Big[1 - \theta(k_F - |\vec{P}+\vec{l}\,|)\Big]\,\Big[1 - \theta(k_F - |\vec{P}-\vec{l}\,|)\Big] \\ + \theta(k_F - |\vec{P}+\vec{l}\,|)\,\theta(k_F - |\vec{P}-\vec{l}\,|)\Big\} \,. \end{aligned} \tag{6.17}$$

The first term with the product $[1-\theta][1-\theta]$ vanishes because it is Pauli-blocked due to the impossibility of satisfying simultaneously the three conditions:

$$\left\{\begin{array}{l} k_F^2 < |\vec{P}+\vec{l}\,|^2 \\ k_F^2 < |\vec{P}-\vec{l}\,|^2 \\ \vec{l}^{\,2} - \vec{q}^{\,2} = 0 \end{array}\right. \implies 2k_F^2 < |\vec{P}+\vec{l}\,|^2 + |\vec{P}-\vec{l}\,|^2 = \vec{p}_1^{\,2} + \vec{p}_2^{\,2} + 2(\vec{l}^{\,2} - \vec{q}^{\,2}) < 2k_F^2 \,. \tag{6.18}$$

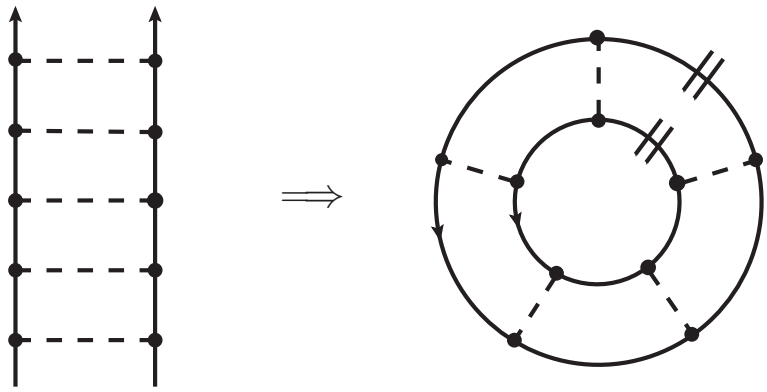

Figure 6.4: The closing of the ladder diagrams gives rise to the bubble ring diagrams and implies a double integration over the Fermi sea of the two incoming nucleons. The Hartree diagrams have a factor 4 from spin degeneracy and the Fock diagrams a factor 2. All diagrams have a 1/2 symmetry factor coming from the interchange of the nucleon lines.

It restricts the scattering of on-shell particles to states below the Fermi surface because of the conservation of energy. The integral simplifies:

$$\mathrm{Im}\, L = 4\pi^2 a \int \frac{\mathrm{d}l^3}{(2\pi)^3}\, \delta(\vec{l}^{\,2} - \vec{q}^{\,2})\, \theta(k_F - |\vec{P} + \vec{l}\,|)\, \theta(k_F - |\vec{P} - \vec{l}\,|)\ . \tag{6.19}$$

The result of the integral is given by the intersection between the spherical surface with radius $q = |\vec{q}\,|$ and center at the origin and the two Fermi spheres whose centers are displaced by $2P$ ($P = |\vec{P}\,|$), as shown in Fig. D.1. The calculation of the integral can be found in Appendix D.1. The outcome is:

$$\mathrm{Im}\, L = a k_F\, I(s,k)\ , \tag{6.20}$$

$$I(s,k) = \begin{cases} k & 0 \leqslant k \leqslant 1-s \\ \dfrac{1}{2s}(1 - s^2 - k^2) & 1 - s < k \leqslant \sqrt{1-s^2} \end{cases}\ . \tag{6.21}$$

Note that the loop integral with two medium insertions is imaginary. The only real component of the loop integral is eq. (6.12). Summing the real and the imaginary parts, we finally obtain:

$$L_0 + L_1 = -\frac{a k_F}{\pi}\left\{R(s,k) + i\pi I(s,k)\right\}\ , \qquad L_2 = 2ia k_F I(s,k)\ , \tag{6.22}$$

$$L = -\frac{a k_F}{\pi}\left\{R(s,k) - i\pi I(s,k)\right\}\ . \tag{6.23}$$

The inclusion/exclusion of the diagram with two medium insertion implies just a change of sign of the imaginary part of the loop integral.

6.3.4 The Energy per Particle

The energy per particle is constructed at any order a^n from the sum of the ladder diagrams up to that order. The closing of the legs simply implies a double integration over the Fermi sea of the two nucleons, $|k_{1,2}| < k_F$, and is symbolized in Fig. 6.4 by a double medium insertion in the resulting rings. The Hartree diagrams get a factor 4 from spin degeneracy, while the Fock diagrams receive a factor 2. All diagrams have a 1/2 symmetry

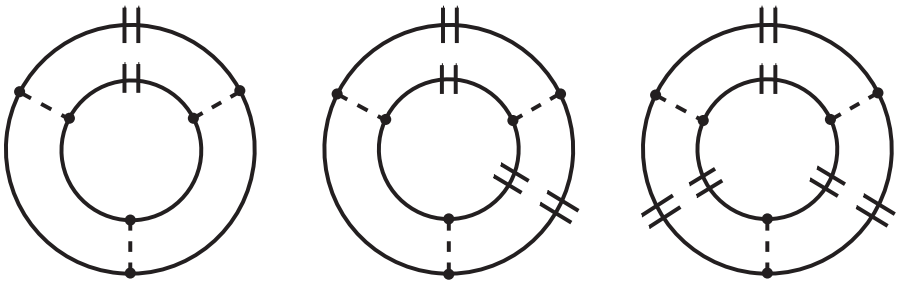

Figure 6.5: Ring diagrams arising from the class of ladder diagrams with $n = 3$. The binomial expansion does not account for the $1/3$ symmetry factor of the diagram with three double medium insertions. At order a^3, the contribution of the sum is $\mathcal{L}_3 = (R + i\pi I)^2 + (R + i\pi I)(-2\pi i I) + (-2i\pi I)^2/3 = R^2 - (\pi I)^2/3$.

factor coming from the exchange of the two nucleonic ring lines. The overall factor is then $(4 - 2)/2 = 1$.

Consider the class of ladder diagrams with n contact terms and $n-1$ loops. A naive line of argument would suggest to associate with it the $n-1$-th power of the loop integral $(R - i\pi I)^{n-1} = [(R + i\pi I) - 2i\pi I]^{n-1}$. However, the energy would then have an imaginary part. A more detailed examination reveals that the combinatorial factors of the ring diagrams are different from the coefficients given by the binomial expansion. For instance, Fig. 6.5 shows the class of ring diagrams resulting from $n = 3$. It is convenient to adopt an organizational scheme that splits the loop contribution into $L_0 + L_1 = R + i\pi I$ and $L_2 = -2\pi i I$. In the figure, a loop with no medium insertions is associated with the term $R + i\pi I$, while a loop with double medium insertion corresponds to the term $-2\pi i I$. This scheme is justified by the fact that different diagrams with the same number/power of L_0 and L_1 have the same combinatorial factor. It is evident that the third diagram in the figure has a symmetry factor of $1/3$ for which the binomial expansion does not account. One finds that the j-th power of the two medium insertion $-2i\pi I$ has to be reweighted by the symmetry factor $1/(j + 1)$. The sum of the diagrams with a given n is:

$$\begin{aligned}
\mathcal{L}_n &= \sum_{j=0}^{n-1} \frac{1}{j+1} \binom{n-1}{j} (R + i\pi I)^{n-1-j} (-2i\pi I)^j \\
&= \sum_{j=0}^{n-1} \frac{1}{n} \binom{n}{j+1} (R + i\pi I)^{n-1-j} (-2i\pi I)^j \\
&= \frac{1}{2\pi i\, I\, n} \left\{ (R + i\pi I)^n - (R - i\pi I)^n \right\} \ . \qquad (6.24)
\end{aligned}$$

The binomial coefficient, as it is rewritten in the second line, offers a clear interpretation. It is the number of all possible ways of arranging the $j + 1$ double medium insertions in a ring diagram with n loops and is divided by the number n of rotations that transform the ring diagram into itself. $\mathcal{L}_n$ is always real for any n. The first terms of the series are:

$$\mathcal{L}_1 = 1 \ , \qquad \mathcal{L}_2 = R \ , \qquad \mathcal{L}_3 = R^2 - \frac{(\pi I)^2}{3} \ , \qquad \mathcal{L}_4 = R(R^2 - \pi^2 I^2) \ . \qquad (6.25)$$

Finally, we carry out the resummation to all orders of $\mathcal{L}_n$:

$$\sum_{n=1}^{\infty} \left(-\frac{a k_F}{\pi} \right)^n \mathcal{L}_n = -\frac{1}{\pi I} \arctan \frac{a k_F I}{1 + \frac{a k_F}{\pi} R} \ . \qquad (6.26)$$

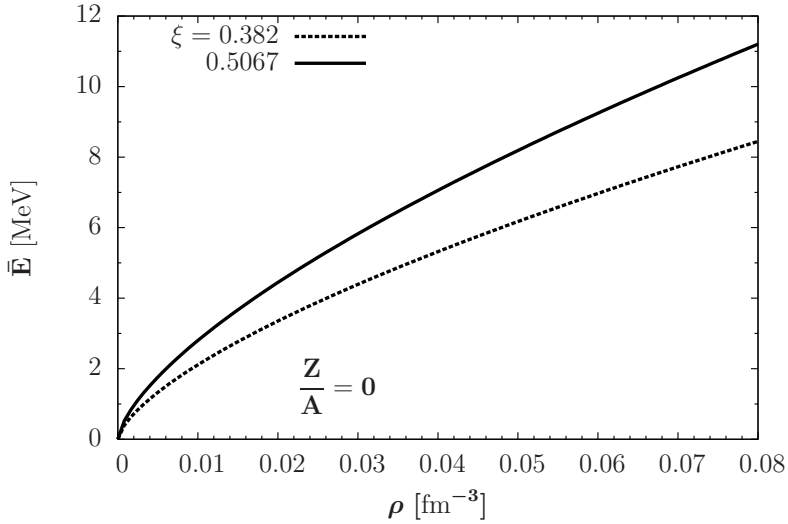

Figure 6.6: Energy per particle of the unitary Fermi system as a function of the neutron density for two different values of the Bertsch parameter ξ. The solid line corresponds to the value obtained in eq. (6.30), the dotted line to the Bertsch parameter resulting from a quantum Monte Carlo simulation in Ref. [121].

The integration over the Fermi seas of $\vec{p}_1$ and $\vec{p}_2$ can be changed to an integration over s and k with the following master formula as demonstrated in Appendix E:

$$\int\limits_{|\vec{p}_{1,2}|<k_F} \frac{\mathrm{d}^3p_1\,\mathrm{d}^3p_2}{(2\pi)^6} f(s,k) = \frac{2k_F^6}{\pi^4}\int_0^1 \mathrm{d}s\, s^2 \int_0^{\sqrt{1-s^2}} \mathrm{d}k\, k\, I(s,k)\, f(s,k)\ . \tag{6.27}$$

The energy per particle after the resummation to all orders becomes:

$$\bar{E}(k_F) = \frac{k_F^2}{2M_N}\left\{\frac{3}{5} - \frac{48}{\pi}\int_0^1 \mathrm{d}s\, s^2 \int_0^{\sqrt{1-s^2}} \mathrm{d}k\, k \arctan\frac{ak_F I(s,k)}{1+\frac{ak_F}{\pi}R(s,k)}\right\}\ . \tag{6.28}$$

The firsts terms of the expansion in powers of ak_F are:

$$\bar{E}(k_F) = \frac{k_F^2}{2M_N}\left\{\frac{3}{5} - \frac{2}{3\pi}ak_F + \frac{4}{35\pi^2}(11-2\ln 2)(ak_F)^2 \right.$$
$$\left. -0.0755733\,(ak_F)^3 + 0.0524813\,(ak_F)^4 + \mathcal{O}(k_F^5)\right\}\ . \tag{6.29}$$

The energy density has been calculated up to several orders of ak_f in the particle-hole formalism and the present expansion is in good agreement with the existing calculations [119, 120].

We can consider the unitary limit $ak_F \to \infty$ and calculate the Bertsch parameter ξ:

$$\xi = 1 - \frac{80}{\pi}\int_0^1 \mathrm{d}s\, s^2 \int_0^{\sqrt{1-s^2}} \mathrm{d}k\, k \arctan\frac{\pi I(s,k)}{R(s,k)} \simeq 0.5067\ . \tag{6.30}$$

In comparison to the result obtained in a recent quantum Monte Carlo calculation $\xi = 0.382$ [121], the present value is somewhat larger. It is compatible with indications from a variety of sophisticated many-body calculations, giving $\xi \approx 0.5$ [122]. The quantum Monte Carlo simulation agrees also well with some experimental determinations, $\xi = 0.32 \pm 0.11$ in Ref. [123] and $\xi = 0.36 \pm 0.15$ in Ref. [124].

In Fig. 6.6 we plot the energy per particle as a function of the density in the unitary limit. The solid line shows the equation of state corresponding to the Bertsch parameter in eq. (6.30). The dotted line is produced using the Bertsch parameter in Ref. [121].

6.4 In-Medium Resummation with Isospin Asymmetry

The in-medium ladder diagram resummation technique has been generalized to systems with isospin asymmetry in collaboration with N. Kaiser. The discussion of the tree-level NN scattering enables to define a strategy for the resummation of the loop integrals.

The NN scattering can be characterized by the scattering length a_s if the two-nucleon state has isospin $I = 1$ (spin singlet) and by the scattering length a_t if the state has isospin $I = 0$ (spin triplet):

$$\langle I = 1 \,|\, \mathcal{T} \,|\, I = 1 \rangle = \frac{4\pi}{M_N}\, a_s \;, \qquad \langle I = 0 \,|\, \mathcal{T} \,|\, I = 0 \rangle = \frac{4\pi}{M_N}\, a_t \;. \tag{6.31}$$

We write the NN tree-level $\mathcal{T}$-matrix in a compact form using the isospin projection operators:

$$\mathcal{T}_{\rm tree} = \frac{4\pi}{M_N} \left[a_s \, \frac{3 + \boldsymbol{\tau}_1 \cdot \boldsymbol{\tau}_2}{4} + a_t \, \frac{1 - \boldsymbol{\tau}_1 \cdot \boldsymbol{\tau}_2}{4} \right] \;. \tag{6.32}$$

If we consider the physical scattering processes, the transition amplitude is a combination of a_s and a_t in the channels with non-defined isospin:

$$\begin{aligned} &p\,p \longrightarrow p\,p : \;\; a_s && n\,n \longrightarrow n\,n : \;\; a_s \\ &p\,n \longrightarrow p\,n : \;\; \frac{1}{2}(a_s + a_t) && n\,p \longrightarrow n\,p : \;\; \frac{1}{2}(a_s + a_t) \\ &p\,n \longrightarrow n\,p : \;\; \frac{1}{2}(a_s - a_t) && n\,p \longrightarrow p\,n : \;\; \frac{1}{2}(a_s - a_t) \end{aligned} \tag{6.33}$$

The problem is more easily treated using a matrix notation. We introduce the orthonormal basis with the physical scattering states $(|pp\rangle\,, |nn\rangle\,, |pn\rangle\,, |np\rangle)$. The different scattering processes can be arranged in a matrix of the form:

$$\mathcal{T} = \begin{array}{c} \\ pp \\ nn \\ pn \\ np \end{array} \begin{array}{c} \begin{array}{cccc} pp & nn & pn & np \end{array} \\ \begin{pmatrix} t_p & 0 & 0 & 0 \\ 0 & t_n & 0 & 0 \\ 0 & 0 & t_a & t_b \\ 0 & 0 & t_b & t_a \end{pmatrix} \end{array} . \tag{6.34}$$

Defining the coupling matrix

$$\sqrt{a} = \sqrt{\frac{4\pi}{M_N}} \begin{pmatrix} \sqrt{a_s} & 0 & 0 & 0 \\ 0 & \sqrt{a_s} & 0 & 0 \\ 0 & 0 & \frac{1}{2}(\sqrt{a_s} + \sqrt{a_t}) & \frac{1}{2}(\sqrt{a_s} - \sqrt{a_t}) \\ 0 & 0 & \frac{1}{2}(\sqrt{a_s} - \sqrt{a_t}) & \frac{1}{2}(\sqrt{a_s} + \sqrt{a_t}) \end{pmatrix} \;, \tag{6.35}$$

we can write $\mathcal{T}$ as:

$$\mathcal{T} = \sqrt{a}\, R \sqrt{a} = \sqrt{a} \begin{pmatrix} r_p & 0 & 0 & 0 \\ 0 & r_n & 0 & 0 \\ 0 & 0 & r_a & r_b \\ 0 & 0 & r_b & r_a \end{pmatrix} \sqrt{a} = \frac{4\pi}{M_N} \begin{pmatrix} a_s r_p & 0 & 0 & 0 \\ 0 & a_s r_n & 0 & 0 \\ 0 & 0 & s_a & s_b \\ 0 & 0 & s_b & s_a \end{pmatrix} \;, \tag{6.36}$$

with

$$s_a = \frac{a_s(r_a + r_b) + a_t(r_a - r_b)}{2} , \qquad s_b = \frac{a_s(r_a + r_b) - a_t(r_a - r_b)}{2} . \tag{6.37}$$

We reproduce $\mathcal{T}_{\text{tree}}$ when R is an identity matrix: $r_p = r_n = r_a = 1, r_b = 0$. At higher orders, the ladder diagrams generate corrections to the identity matrix through the loop integrals. Indicating with L the loop matrix, R can be expressed as a power series in L:

$$R = \mathbb{1} + \begin{pmatrix} L_p & 0 & 0 & 0 \\ 0 & L_n & 0 & 0 \\ 0 & 0 & L_a & L_b \\ 0 & 0 & L_b & L_a \end{pmatrix} + \cdots = \mathbb{1} + L + L^2 + \cdots = \sum_{n=0}^{\infty} L^n \tag{6.38}$$

It is impossible to carry out this series in powers of L in the basis of the physical states where the matrix R is not diagonal. The problem simplifies in the isospin basis defined as $(|1,1\rangle , |1,-1\rangle , |1,0\rangle , |0,0\rangle)$, because the $\mathcal{T}$-matrix becomes diagonal, with elements given by its eigenvalues (neglecting a factor $4\pi/M_N$ for simplicity):

$$t_p = a_s r_p , \quad t_n = a_s r_n , \quad t_a + t_b = a_s(r_a + r_b) , \quad t_a - t_b = a_t(r_a - r_b) . \tag{6.39}$$

The different channels decouple and the matrix R is easily calculated through the resummation of the eigenvalues of the loop matrix L:

$$r_p = \sum_n L_p^n , \quad r_n = \sum_n L_n^n , \quad r_a + r_b = \sum_n (L_a + L_b)^n , \quad r_a - r_b = \sum_n (L_a - L_b)^n . \tag{6.40}$$

6.4.1 The Loop Matrix

We proceed with the evaluation of the one-loop diagram arranging the contributions of the different scattering processes in the matrix L defined in eq. (6.38). We write L as the product:

$$L = i\sqrt{a} \begin{pmatrix} S_p S_p & 0 & 0 & 0 \\ 0 & S_n S_n & 0 & 0 \\ 0 & 0 & S_p S_n & 0 \\ 0 & 0 & 0 & S_p S_n \end{pmatrix} \sqrt{a} , \tag{6.41}$$

where the notations S_p and S_n indicate the in-medium proton and neutron propagators, respectively. With the introduction of the coupling matrix $\sqrt{a}$ that accounts for the off-diagonal elements, the action of the loop integral is reduced to that of a diagonal matrix whose elements are the products of the nucleon propagators associated with the loop. An integration over the loop momentum is implicit.

The calculation of L_p and L_n leads to expressions of the same form of eq. (6.23) but with the insertion of the proper Fermi momentum:

$$L_p = L(k_F \to k_p) , \qquad L_n = L(k_F \to k_n) , \tag{6.42}$$

with k_p and k_n the proton and neutron Fermi momenta, respectively.

L_a and L_b differ only for the coupling:

$$L_{a,b} = \frac{4\pi i}{M_N} \frac{a_s \pm a_t}{2} \int \frac{\mathrm{d}^4 l}{(2\pi)^4} S_p(P + l) S_n(P - l) . \tag{6.43}$$

Following the procedure developed in the previous section, the loop integral consists of real and imaginary parts. The real part is:

$$\mathrm{Re}\, L_{a,b} = -2\pi(a_s \pm a_t)\, \mathcal{P} \int \frac{\mathrm{d}^3 l}{(2\pi)^3} \frac{1}{\vec{l}^{\,2} - \vec{q}^{\,2} - i\epsilon} \left\{ \theta(k_p - |\vec{P} + \vec{l}\,|) + \theta(k_n - |\vec{P} - \vec{l}\,|) \right\} . \tag{6.44}$$

In contrast to the previous case with only a single Fermi sea, the two step functions are defined over different Fermi spheres and do not give the same contribution. We find:

$$\mathrm{Re}\, L_{a,b} = -\frac{a_s \pm a_t}{4\pi} (k_p R_p + k_n R_n) , \tag{6.45}$$

$$R_p \equiv R\left(\frac{P}{k_p}, \frac{q}{k_p}\right) , \qquad R_n \equiv R\left(\frac{P}{k_n}, \frac{q}{k_n}\right) , \tag{6.46}$$

where $R(s,k)$ is the function in eq. (6.13). We come now to the imaginary part. The corresponding integral is:

$$\mathrm{Im}\, L_{a,b} = 2\pi(a_s \pm a_t) \int \frac{\mathrm{d}^3 l}{(2\pi)^3}\, \delta(\vec{l}^{\,2} - \vec{q}^{\,2}) \left\{ \left[1 - \theta(k_p - |\vec{P} + \vec{l}\,|)\right] \left[1 - \theta(k_n - |\vec{P} - \vec{l}\,|)\right] + \theta(k_p - |\vec{P} + \vec{l}\,|)\, \theta(k_n - |\vec{P} - \vec{l}\,|) \right\} . \tag{6.47}$$

Even in this case the product $[1-\theta][1-\theta]$ vanishes:

$$\begin{cases} k_p^2 < |\vec{P} + \vec{l}\,|^2 \\ k_n^2 < |\vec{P} - \vec{l}\,|^2 \\ \vec{l}^{\,2} - \vec{q}^{\,2} = 0 \end{cases} \implies k_p^2 + k_n^2 < \vec{p}_1^{\,2} + \vec{p}_2^{\,2} < k_p^2 + k_n^2 . \tag{6.48}$$

The loop integral has a geometrical interpretation similar to the case of pure neutron matter. Its solution is the portion of the spherical surface with radius q and center at the origin in common with the intersection of the two Fermi spheres whose centers are displaced by $2P$. However, the Fermi spheres have now different radii, k_p and k_n, and this gives rise to a variety of possible configurations. The calculation of the integral is carried out in Appendix D.2. We report directly the outcome:

$$\mathrm{Im}\, L_{a,b} = \frac{1}{2}(a_s \pm a_t) I_{pn} , \tag{6.49}$$

$$I_{pn} = \begin{cases} 0 & q > k_p + P \\ q\, \theta(k_p - P) & q \leqslant |k_p - P| \\ \dfrac{k_p^2 - (P-q)^2}{4P} & |k_p - P| < q \leqslant |k_n - P| \\ \dfrac{k_p^2 + k_n^2 - 2(P^2 + q^2)}{4P} & |k_n - P| < q \leqslant \sqrt{\frac{k_p^2 + k_n^2}{2} - P^2} \end{cases} , \tag{6.50}$$

with $P = |\vec{P}|$ and $q = |\vec{q}|$. We rewrite the results in terms of the eigenvalues of the loop matrix L:

$$L_p = -\frac{a_s k_p}{\pi} (R_p - i\pi I_p) , \qquad L_n = -\frac{a_s k_n}{\pi} (R_n - i\pi I_n) , \tag{6.51}$$

$$L_a \pm L_b = -\frac{a_{s,t}}{\pi} \left(\frac{k_p}{2} R_p + \frac{k_n}{2} R_n - i\pi I_{pn} \right) . \tag{6.52}$$

The resummation of the ladder diagrams to all orders can be carried out using eq. (6.26). Combining eq. (6.39) and (6.40), one finds the eigenvalues of the $\mathcal{T}$-matrix:

$$t_{p,n} = \frac{1}{k_{p,n} I_{p,n}} \arctan \frac{a_s k_{p,n} I_{p,n}}{1 + \dfrac{a_s k_{p,n}}{\pi} R_{p,n}} , \tag{6.53}$$

$$t_a \pm t_b = \frac{1}{I_{pn}} \arctan \frac{a_{s,t} I_{pn}}{1 + \dfrac{a_{s,t}}{2\pi}(k_p R_p + k_n R_n)} . \tag{6.54}$$

6.4.2 The Energy per Particle

Once the ladder diagrams are resummed, we calculate the energy per particle by considering the corresponding ring diagrams. We sum over all processes in the $\mathcal{T}$-matrix (6.34) with the correct factors coming from symmetry and spin degeneracy. Note that the interaction described by the $\mathcal{T}$-matrix elements can exchange the incoming particles. The exchange processes give rise to off-diagonal elements in proton-neutron scattering, labeled with t_b. Concerning proton-neutron scattering, the diagonal elements t_a generate the Hartree ring diagrams, while the Fock diagrams arise from the exchange processes characterized by t_b. Using the same arguments of section 6.46, the Hartree diagrams have an overall factor $4 \cdot 1/2 = 2$. We indicate with the symbol θ_{NN} the generic NN scattering process in the $\mathcal{T}$-matrix. The contribution of the Hartree diagrams to the energy density is of the form:

$$\mathcal{T}_{\text{Hartree}} = 2[\theta_{pp}\, t_p + \theta_{nn}\, t_n + (\theta_{pn} + \theta_{np}) t_a] . \tag{6.55}$$

A similar discussion is valid for the Fock diagrams, whose overall factor is $2 \cdot 1/2 = 1$:

$$\mathcal{T}_{\text{Fock}} = -[\theta_{pp}\, t_p + \theta_{nn}\, t_n + (\theta_{pn} + \theta_{np}) t_b] . \tag{6.56}$$

Their sum is:

$$\begin{aligned} \mathcal{T}_{\text{Hartree}} + \mathcal{T}_{\text{Fock}} &= \theta_{pp}\, t_p + \theta_{nn}\, t_n + (\theta_{pn} + \theta_{np})(2t_a - t_b) \\ &= \theta_{pp}\, t_p + \theta_{nn}\, t_n + \theta_{pn}[(t_a + t_b) + 3(t_a - t_b)] . \end{aligned} \tag{6.57}$$

With the outcome written in terms of the eigenvalues of the $\mathcal{T}$-matrix, the calculation of the energy per particle is now straightforward. The integration over the Fermi seas of the two particle species gives:

$$\begin{aligned} \rho \bar{E}(k_p, k_n) = \frac{k_p^5 + k_n^5}{10\pi^2 M_N} - \frac{4\pi}{M_N} \Bigg\{ & \int_{|\vec{p}_{1,2}|<k_p} \frac{\mathrm{d}^3 p_1 \mathrm{d}^3 p_2}{(2\pi)^6}\, t_p + \int_{|\vec{p}_{1,2}|<k_n} \frac{\mathrm{d}^3 p_1 \mathrm{d}^3 p_2}{(2\pi)^6}\, t_n \\ & + \int_{|\vec{p}_{1,2}|<k_{p,n}} \frac{\mathrm{d}^3 p_1 \mathrm{d}^3 p_2}{(2\pi)^6} [(t_a + t_b) + 3(t_a - t_b)] \Bigg\} . \end{aligned} \tag{6.58}$$

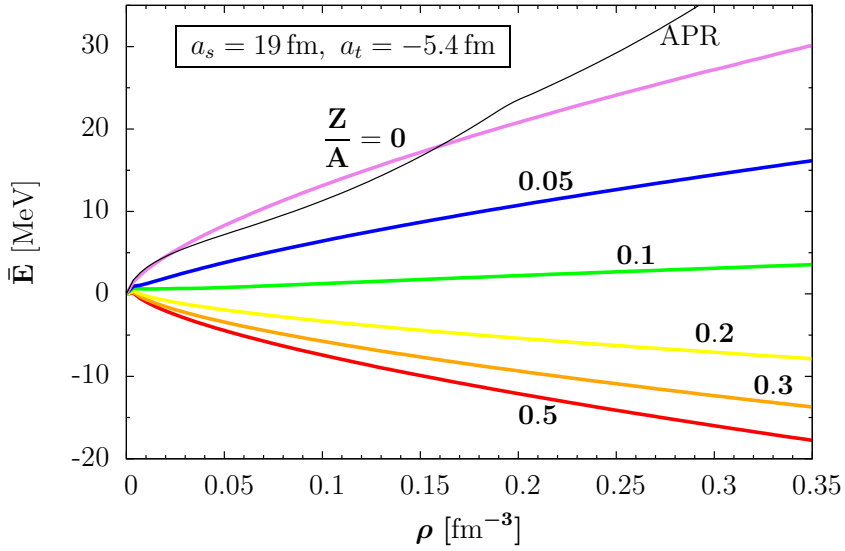

Figure 6.7: Energy per particle as a function of the nucleon density resulting from the in-medium ring diagram resummation. The curves display the energy for different values of the proton fraction $x_p = Z/A$. One can compare the violet curve corresponding to $x_p = 0$ with the Akmal-Pandharipande-Ravenhall equation of state of pure neutron matter (black line) [25].

Using eqs. (6.53) and (6.54), we finally obtain:

$$\begin{aligned}\bar{E}(k_p,k_n) = \frac{3}{M_N(k_p^3+k_n^3)}\Bigg\{ &\frac{k_p^5+k_n^5}{10} - \frac{8k_p^5}{\pi}\int_0^1 \mathrm{d}s\, s^2 \int_0^{\sqrt{1-s^2}} \mathrm{d}k\, k \arctan\frac{a k_p\, I(s,k)}{1+\frac{a k_p}{\pi}R(s,k)} \\ &- \frac{8k_n^5}{\pi}\int_0^1 \mathrm{d}s\, s^2 \int_0^{\sqrt{1-s^2}} \mathrm{d}k\, k \arctan\frac{a k_n\, I(s,k)}{1+\frac{a k_n}{\pi}R(s,k)} \\ &- \frac{1}{2\pi}\int_0^{k_p}\mathrm{d}p_1\, p_1^2 \int_0^{k_n}\mathrm{d}p_2\, p_2^2 \int_{-1}^{1}\mathrm{d}x\, \frac{1}{I_{pn}}\Bigg[\arctan\frac{a_s I_{pn}}{1+\frac{a_s}{2\pi}(k_pR_p+k_nR_n)} \\ &+3\arctan\frac{a_t I_{pn}}{1+\frac{a_t}{2\pi}(k_pR_p+k_nR_n)}\Bigg]\Bigg\}\ , \end{aligned} \tag{6.59}$$

with $a_s = 19$ fm and $a_t = -5.4$ fm and R_p and R_n defined in eq. (6.46). The first term is the kinetic energy of protons and neutrons. The other terms are, in this order, the contributions of pp and nn scattering and that of np scattering in the isospin triplet ($I = 1, I_3 = 0$) and singlet ($I = 0, I_3 = 0$) states. The variables P and q in the functions R_p and R_n are related to p_1 and p_2 by $P, q = (\sqrt{p_1^2+p_2^2 \pm 2\,x\,p_1p_2})/2$.

We have employed the master formula (6.27) to change the integration variable to s and k in the pp and nn terms. A similar master formula is valid also for the terms with different

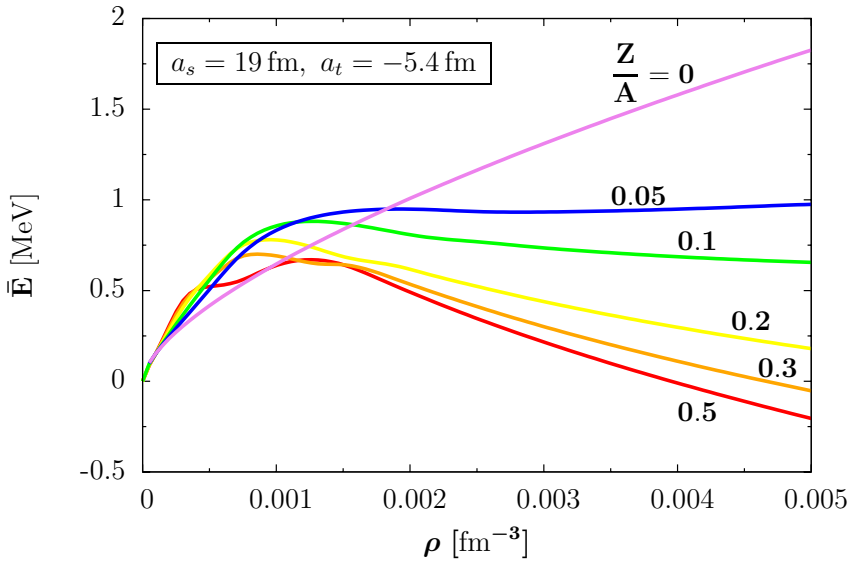

Figure 6.8: Energy per particle as a function of the nucleon density at very low density $\rho \lesssim 0.005\,\mathrm{fm}^{-3}$. A sort of double-hump behaviour develops with increasing proton fraction x_p and is governed by the spin-triplet term of eq. (6.59).

Fermi seas:

$$\int_0^{k_p} \mathrm{d}p_1\, p_1^2 \int_0^{k_n} \mathrm{d}p_2\, p_2^2 \int_{-1}^{1} \mathrm{d}x\, f(P,q) = 16 \int_0^{\frac{k_p+k_2}{2}} \mathrm{d}P\, P^2 \int_{q_{\min}}^{q_{\max}} \mathrm{d}q\, q\, I_{pn}\, f(P,q)\ , \tag{6.60}$$

$$q_{\min} = \max(0, P - k_p)\ , \qquad q_{\max} = \min\left(k_p + P, \sqrt{\frac{k_p^2 + k_n^2}{2} - P^2}\right)\ . \tag{6.61}$$

The formula is constructed by analogy with eq. (6.27) and with the use of the plot D.3a showing the domain of the function I_{pn}. The validity of the master formula for the calculation of the energy per particle has been checked numerically.

6.5 Energy of Nuclear Matter from Ring Diagram Resummation

In Fig. 6.7 we investigate systematically the contributions of resummed contact terms, based on the scattering lengths a_s and a_t, to the energy per particle, and their dependence on the isospin-asymmetry. Starting from symmetric nuclear matter, indicated by the red line, the figure shows the evolution of the energy per particle as a function of the density for increasing isospin asymmetry up to the case of pure neutron matter (violet line). At the scale of density displayed in the plot the energy appears to have a regular and systematic behaviour. However, a zoom in the density scale reveals a more complicated behaviour at very low density.

In Fig. (6.8) we observe for $\rho \lesssim 0.003\,\mathrm{fm}^{-3}$ a sort of double-hump behaviour. It is related to the appearance of the protons in matter because the effect is maximally prominent for symmetric nuclear matter and absent in pure neutron matter. The effect presumably originates from one of or both the pn scattering terms of eq. (6.59).

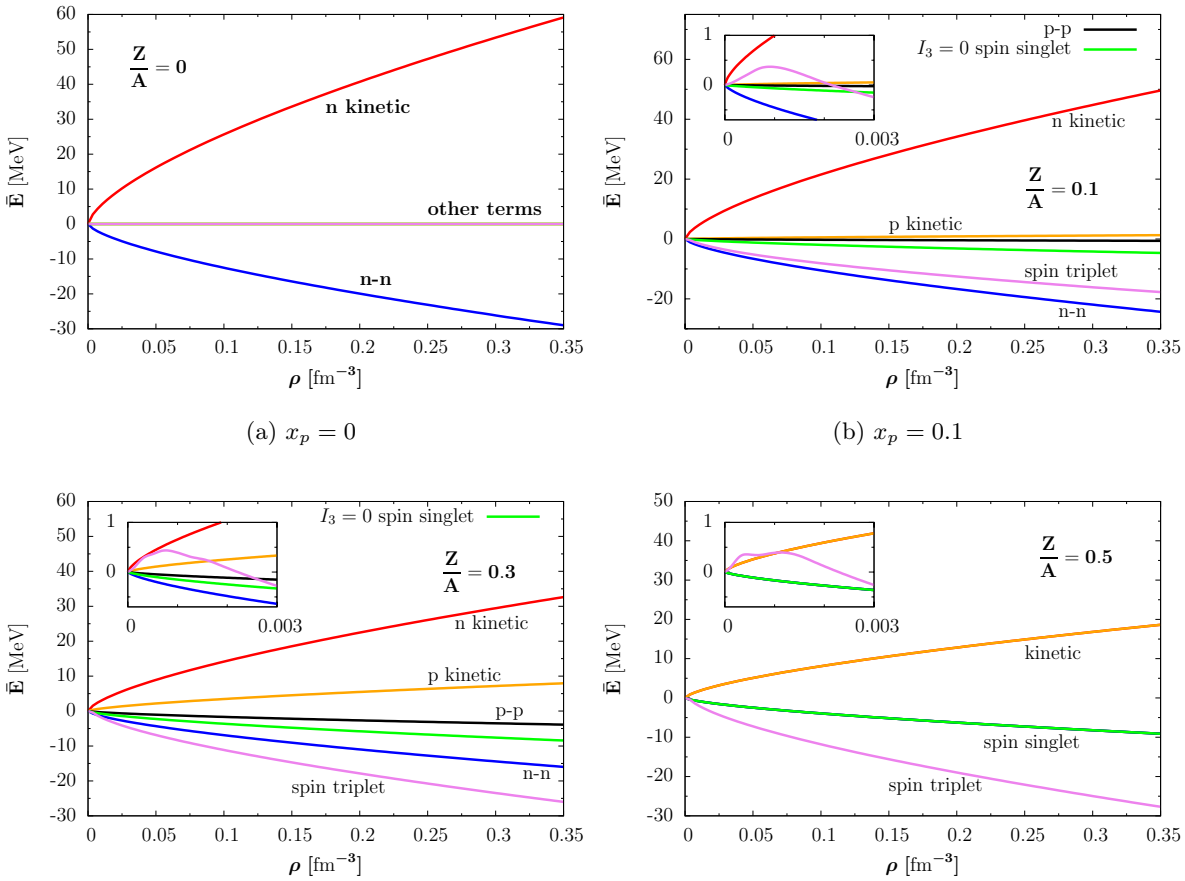

(a) $x_p = 0$ (b) $x_p = 0.1$

(c) $x_p = 0.3$ (d) $x_p = 0.5$

Figure 6.9: The plots show the different terms of eq. (6.59) contributing to the energy per particle of nuclear matter for increasing proton fraction. The contributions include the proton and neutron kinetic energies, the spin-singlet (nn, pp and $I_3 = 0$) and the spin-triplet ($I = 0$) terms. The insets zoom in the curves at low density ($\rho \lesssim 0.003$ fm^{-3}) revealing that the spin triplet term changes sign because of the negative value of a_t.

Fig. 6.9 clarifies this point. The plots show the contribution of the single terms of eq. (6.59) to the energy per particle for several proton fractions x_p. The first plot relates to pure neutron matter: only the neutron kinetic energy and the nn scattering term are present. With increasing x_p the other terms involving protons appear and become gradually larger while the nn terms decrease. In particular, note how the spin-triplet term changes the sign at very low density from positive to negative and develops the double-hump behaviour as x_p approaches the value 0.5. This feature is explained by the negative scattering length a_t entering the spin-triplet term. Because of the negative value of a_t, the denominator of the fraction in the arctangent function, in contrast to the spin-singlet term, change sign when $|a_t|(k_p R_p + k_n R_n) > 2\pi$, causing in this way the behaviour observed in the plots. Of course, in the actual physics situation these particular low-density features are overruled by a most important effect not considered here, namely the formation of nuclear clusters.

Fig. 6.10 shows how the interaction changes with the scattering length. The energy per particle of neutron matter divided by the kinetic energy $\bar{E}(k_F)/E_{\rm kin}(k_F)$ is plotted as a function of the adimensional quantity ak_F. For positive ak_F the interaction energy is negative and attractive. The negative branch of ak_F presents a more involved behaviour. For small values of $|ak_F|$ the energy per particle has a peak and the interaction is repulsive.

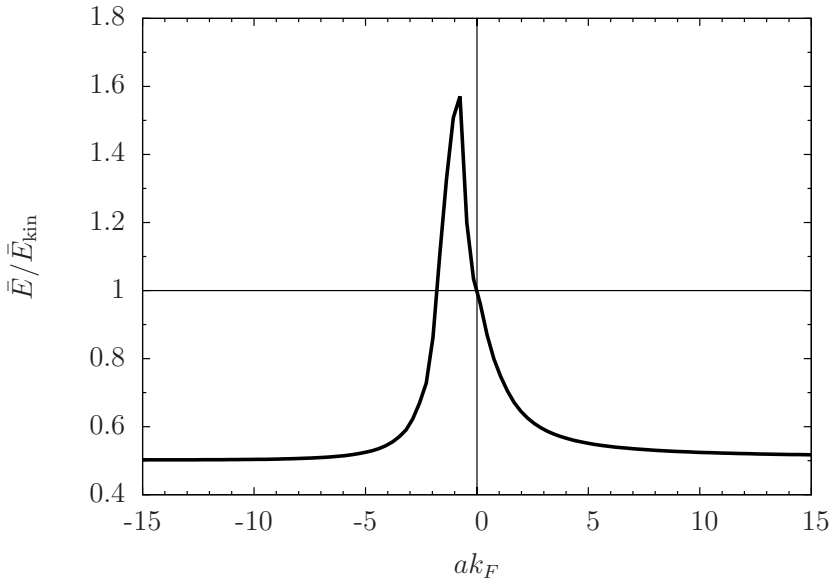

Figure 6.10: Energy per particle of neutron matter normalized to the kinetic energy as a function of the adimensional variable ak_F. In the resonant limit $ak_F \to \pm\infty$ the system tends to a unitary behaviour. For positive ak_F the interaction energy is attractive. For $ak_F < 0$, the interaction energy is at first repulsive at small values of the parameter, then becomes again attractive with growing $|ak_F|$.

With increasing $|ak_F|$ the interaction energy originating from nn scattering in the medium changes sign and becomes again negative and attractive. Note that both branches tend to the unitary limit for $ak_F \to \pm\infty$. Although the plot refers - strictly speaking - to the nn scattering term, it also explains qualitatively the behaviour of the spin-triplet energy term in Fig. 6.9.

Chapter 7

Summary and Outlook

In this thesis we have used in-medium Chiral Perturbation Theory (ChPT) to investigate the thermodynamic properties of nuclear matter. As this approach and the underlying Chiral Effective Field Theory establish the interface between low-energy QCD and nuclear physics, this is presumably the appropriate framework to set important nuclear physics constraints for the construction of the QCD phase diagram at low temperature and finite baryon densities.

ChPT is recognized as a powerful tool for attacking the nuclear many-body problem in consideration of the fact that pion-exchange dynamics plays an essential role for reproducing the empirical features of nuclear matter - such as the saturation density, the binding energy and the liquid-gas phase transition. Moreover, the typical scales that one encounters in the description of nuclear matter - the pion mass m_π, the Fermi momentum at the saturation point $k_F \simeq 2m_\pi$, and the Δ-isobar - nucleon mass splitting $\Delta \simeq 293$ MeV - are all well below the spontaneous symmetry breaking scale of the theory, $\Lambda \sim 1$ GeV. Our approach is based on a separation of scales between the long- and intermediate-range correlations and the short-distance physics. The former corresponds to 1π- and 2π-exchange dynamics and is treated explicitly up to three-loop order with inclusion of the Δ-isobar excitation. In this way, the attractive part of the nucleon-nucleon interaction is basically reproduced. The short-range interaction is unresolved in the scales of momenta involved and is accounted for by means of a few S-wave contact terms fixed to reproduce some selected known properties of nuclear matter.

The basic ingredient to perform calculations at finite density is the in-medium nucleon propagator. We follow an organizational scheme in the number of medium insertion in the Feynman diagrams. Two-body and three-body forces (where the latter include genuine three-body forces and the Pauli-blocking on two-body terms) are systematically taken into account. The free energy density of nuclear matter is given by a sum of convolution integrals describing the many-body effects according to the number of integrations over the nucleon momentum distributions. The free energy per particle is evaluated numerically.

We have presented a detailed study of the equation of state of nuclear matter as a function of the nucleon density and the temperature. Furthermore, the isospin-dependence of the corresponding phase diagram has been investigated with the help of the Maxwell construction. Starting from isospin-symmetric nuclear matter, pressure isotherms display clearly a first-order liquid-gas phase transition with a behaviour similar to that of the well-known van-der-Waals equation of state. By imposing only that the energy minimum of the curve at $T = 0$ is -16 MeV per nucleon, the model predicts a saturation density $\rho_0 \simeq 0.157\,\mathrm{fm}^{-3}$, remarkably close to the empirical value, and a compression modulus $K(\rho_0) \simeq 300$ MeV. The critical point is located at $T_c \simeq 15.1$ MeV and $\rho_c \simeq \rho_0/3$. We emphasize that the liquid-gas phase transition is the result of the subtle balance between the long- and intermediate range interaction described primarily by pion-exchange dynamics

and the unresolved short-distance physics encoded in the contact terms. With increasing isospin-asymmetry the liquid-gas coexistence region gradually shrinks and disappears at the proton fraction $x_p \simeq 0.05$. Neutron-rich matter cannot undergo any phase transition. In a similar way, for decreasing proton fraction, the binding energy of nuclear matter is reduced. Below $x_p \simeq 0.12$ neutron-rich matter is unbound at any density and temperature.

The chiral condensate is the order parameter of the chiral phase transition and is related to the derivative with respect to the pion mass of the free energy per particle. This derivative can be carried out within our scheme because the pion mass appears as an explicit parameter in the interacting energy. We have investigated the dependence on the nucleon density and the temperature of the chiral quark condensate of symmetric nuclear matter, normalized to its vacuum value, in the density range $0 \leq \rho \lesssim 2\,\rho_0$ and for $T \lesssim 100$ MeV. The main source of uncertainty in the calculation is represented by the sigma term which guides the dropping of the leading contribution linear in the density. At low temperature, the Δ-isobar degree of freedom plays a fundamental role in retarding the decrease of the condensate and, actually, stabilizes it at large density. Its inclusion is essential to determine the behaviour of the chiral condensate. The thermodynamics of the chiral condensate is the result of the interplay between attractive two-body interactions and repulsive three-body in-medium correlations. At low T these latter are dominant and counteract the reduction of the condensate relative to its vacuum value. At $T = 100$ MeV, their contribution is balanced by the two-body term and the linear behaviour of the sigma term is practically restored. In the liquid-gas coexistence region present for $T \lesssim 15$ MeV, the condensate drops linearly. Finally, the contribution of the pionic heat bath is included and gives a further temperature-dependent reduction of the condensate. We find no indication of a first-order chiral phase transition in the density range $0 \leq \rho \lesssim 2\,\rho_0$ and at temperatures $T \lesssim 100$ MeV.

In neutron-rich matter, the large neutron-neutron scattering length, $a_{nn} \simeq 19$ fm, invalidates the perturbative expansion of the $\mathcal{T}$-matrix in powers of p. A resummation to all orders of the S-wave contact interaction is required. The in-medium propagator enables to implement the resummation at finite density. It gives rise to loop integrals with zero, one and two medium insertions. The multi-loop vacuum ring diagrams are powers of the basic loop integral with the proper combinatorial and symmetry factors and are summed to all orders. The resummation is then extended to isospin-asymmetric nuclear matter. The loop contributions to the different scattering processes are arranged in a 4×4 matrix. Once the matrix is diagonalized moving to the isospin basis, the resummation is easily carried out as sum of the eigenvalues.

We have studied the isospin-dependence of the energy per particle as a function of the nucleon density. The resulting curves display an oscillating behaviour at very low density, $\rho \lesssim 0.005\,\mathrm{fm}^{-3}$, emerging for increasing proton fraction in matter. The study of the single contributions to the energy per particle reveals that it arises from the spin-triplet term and its negative scattering length, $a_t \simeq -5.42$ fm, entering the corresponding function.

As an outlook for future issues and projects to be carried out, we end with a list of topics for further developments:

- The convergence of the expansion at three-loop order is ensured as long as four-body correlations are not predominant. Preliminary calculations give encouraging results. Contributions of four-nucleon forces to the binding energy of ^{4}He have been estimated to have a magnitude somewhat smaller than 1 MeV in ChPT [73]. In Ref. [76], the contributions of two chiral four-nucleon diagrams to the equation of state stay below 0.1 MeV in the density range of interest and are thus negligible. However, one expects more significant effects with the inclusion of the Δ-isobar. The issue of the magnitude of four-body correlations in nuclear matter is still open.

- The formalism for carrying out an in-medium resummation to all orders of the ring

diagrams with S-wave contact interaction has been developed. The next possible steps are, on one hand, the inclusion of the effective range r_0 through a (S-wave) q^2-dependent contact interaction and of P-wave scattering. On the other hand, the equation of state resulting from in-medium resummations has to be combined with the chiral equation of state at three-loop order. This requires a separation between the contribution of the S-wave contact terms and that of pion-exchange dynamics to the nucleon-nucleon scattering length, because only the former has to be resummed. Specifically, one can write, e.g. for the scattering lengths, $a_{\rm phys} = a_0 + a_\pi$, and only a_0 is inserted in the resummation formulae. The corresponding energy can then be added to the chiral equation of state and the contact terms B_3 and B_5 retuned to encode the residual short-distance physics.

- There have been very important astrophysical achievements in the last few years. A most important result is the discovery of a two-solar-mass neutron star. Its mass, $M = (1.97 \pm 0.04) M_\odot$ [3], is determined very accurately and sets decisive constraints on the equation of state of dense matter. In order to support the pressure to stabilize such a massive object against gravitation, the equation of state of neutron star matter must be sufficiently stiff. In particular, soft scenarios with meson condensation or quark matter would be ruled out. It is an interesting point to establish whether our equation of state can sustain a two-solar-mass neutron star. Extrapolations to large supranuclear densities are possible following the analysis in Ref. [4].

Appendix A

In-Medium Fermion Propagator

In this appendix we derive the fermion propagator in the presence of a medium at $T = 0$ and at finite temperature using the formalism of Thermal Field Theory.

A.1 In-Medium Fermion Propagator at $T = 0$

First we remind the result for the vacuum. The fermion field $\Psi(x)$, solution of the Dirac-equation, reads [125]:

$$\Psi(x) = \int \frac{\mathrm{d}^3 p}{(2\pi)^3} \frac{1}{\sqrt{2E_{\vec{p}}}} \sum_{s=1,2} \left[a^s_{\vec{p}}\, u_s(p) e^{-ipx} + b^{\dagger s}_{\vec{p}}\, v_s(p) e^{ipx} \right] , \tag{A.1}$$

where $\Psi(x)$, $u_s(p)$ and $v_s(p)$ are four-spinors and s is the polarization index. The conjugate field is $\bar{\Psi}(x) = \Psi^\dagger(x)\,\gamma^0$. The operator $a^s_{\vec{p}}$ annihilates a particle of momentum $\vec{p}$ and polarization s; $a^{\dagger s}_{\vec{p}}$ creates instead a particle with momentum $\vec{p}$ and polarization s. The operator $b^s_{\vec{p}}/b^{\dagger s}_{\vec{p}}$ annihilates/creates an antiparticle. These operators satisfy the following anticommutation rules:

$$\{a^r_{\vec{p}}, a^{\dagger s}_{\vec{q}}\} = \{b^r_{\vec{p}}, b^{\dagger s}_{\vec{q}}\} = (2\pi)^3 \delta(\vec{p} - \vec{q})\, \delta^{rs} . \tag{A.2}$$

The vacuum state $|0\rangle$ is defined such that

$$a^s_{\vec{p}}|0\rangle = 0 , \qquad b^s_{\vec{p}}|0\rangle = 0 . \tag{A.3}$$

The vacuum propagator is the time-ordered expectation value of the product $\Psi(x)\bar{\Psi}(y)$ in the vacuum:

$$\begin{aligned} S_{F0}(x-y) &= \langle 0|\, T[\Psi(x)\bar{\Psi}(y)]\, |0\rangle \\ &= \langle 0|\, \Psi(x)\bar{\Psi}(y)\, |0\rangle\, \theta(x^0 - y^0) - \langle 0|\, \bar{\Psi}(y)\Psi(x)\, |0\rangle\, \theta(y^0 - x^0) . \end{aligned} \tag{A.4}$$

In the presence of a medium (at $T = 0$), the definition is slightly modified. The ground state of the system is no longer the vacuum but the filled Fermi sea $|\phi_0\rangle$. The action of annihilation and creation operators on it changes according to their momenta. Indicating with k_F the Fermi momentum of the fermionic system, we have:

- $|\vec{p}| > k_F$ — annihilation: $a^s_{\vec{p}}$, creation: $a^{\dagger s}_{\vec{p}}$ } particle, $b^s_{\vec{p}}$, $b^{\dagger s}_{\vec{p}}$ } antiparticle, $a^s_{\vec{p}}|\phi_0\rangle = b^s_{\vec{p}}|\phi_0\rangle = 0$, (A.5)
- $|\vec{p}| < k_F$ — creation: $a^s_{\vec{p}}$, annihilation: $a^{\dagger s}_{\vec{p}}$ } hole, $b^s_{\vec{p}}$, $b^{\dagger s}_{\vec{p}}$ } antihole, $a^{\dagger s}_{\vec{p}}\,|\phi_0\rangle = b^{\dagger s}_{\vec{p}}\,|\phi_0\rangle = 0$. (A.6)

In the fermion field we split the nodes above k_F from the nodes below k_F:

$$\Psi(x) = \int \frac{\mathrm{d}^3p}{(2\pi)^3}\frac{1}{\sqrt{2E_{\vec{p}}}}\sum_{s=1,2}\left[a^s_{\vec{p}}\,u_s(p)e^{-ipx} + b^{\dagger s}_{\vec{p}}\,v_s(p)e^{ipx}\right]\left[\theta(|\vec{p}|-k_F)+\theta(k_F-|\vec{p}|)\right] , \tag{A.7}$$

$$\bar{\Psi}(y) = \int \frac{\mathrm{d}^3p}{(2\pi)^3}\frac{1}{\sqrt{2E_{\vec{p}}}}\sum_{r=1,2}\left[a^{\dagger r}_{\vec{p}}\,\bar{u}_r(p)e^{ipy} + b^{r}_{\vec{p}}\,\bar{v}_r(p)e^{-ipy}\right]\left[\theta(|\vec{p}|-k_F)+\theta(k_F-|\vec{p}|)\right] . \tag{A.8}$$

The in-medium propagator is defined as

$$S_F(x-y) = \langle\phi_0|\,T[\Psi(x)\bar{\Psi}(y)]\,|\phi_0\rangle \ . \tag{A.9}$$

After replacing eqs. (A.7) and (A.8) in (A.9), using the anticommutation relations (A.2) and the completeness relations

$$\sum_{s=1,2} u_s(p)\bar{u}_s(p) = \Lambda^+(p) = \not{p} + m \ , \tag{A.10}$$

$$\sum_{s=1,2} v_s(p)\bar{v}_s(p) = -\Lambda^-(p) = \not{p} - m \ , \tag{A.11}$$

we find:

$$\begin{aligned} S_F(x-y) = \int \frac{\mathrm{d}^3p}{(2\pi)^3}\frac{1}{2E_{\vec{p}}}\cdot \\ \Big\{\theta(|\vec{p}|-k_F)\left[(\not{p}+m)e^{-ip(x-y)}\theta(x^0-y^0) - (\not{p}-m)e^{ip(x-y)}\theta(y^0-x^0)\right] \\ +\theta(k_F-|\vec{p}|)\left[(\not{p}-m)e^{ip(x-y)}\theta(x^0-y^0) - (\not{p}+m)e^{-ip(x-y)}\theta(y^0-x^0)\right]\Big\} \ . \end{aligned} \tag{A.12}$$

We use in the equation the integral representation of the step function:

$$\theta(x^0-y^0) = \int_{-\infty}^{\infty}\frac{\mathrm{d}\omega}{2\pi i}\frac{e^{i\omega(x^0-y^0)}}{\omega - i\epsilon} \ . \tag{A.13}$$

We perform a change of variable: $p_0 = E_{\vec{p}} \to p_0 = E_{\vec{p}} - \omega$ in the first and second terms, and $p_0 = E_{\vec{p}} \to p_0 = E_{\vec{p}} + \omega$ in the third and fourth terms. We obtain:

$$\begin{aligned} S_F(x-y) = \int \frac{\mathrm{d}^4p}{(2\pi)^4}\frac{1}{2E_{\vec{p}}\,i}\Bigg\{\theta(|\vec{p}|-k_F)\left[(\not{p}+m)\frac{e^{-ip(x-y)}}{E_{\vec{p}}-p_0-i\epsilon} - (\not{p}-m)\frac{e^{ip(x-y)}}{E_{\vec{p}}-p_0-i\epsilon}\right] \\ +\theta(k_F-|\vec{p}|)\left[(\not{p}-m)\frac{e^{ip(x-y)}}{p_0-E_{\vec{p}}-i\epsilon} - (\not{p}+m)\frac{e^{-ip(x-y)}}{p_0-E_{\vec{p}}-i\epsilon}\right]\Bigg\} \ . \end{aligned} \tag{A.14}$$

We change $p \to -p$ in the second and third terms and, after some manipulations, we find

$$\begin{aligned} S_F(x-y) &= \int \frac{\mathrm{d}^4p}{(2\pi)^4}e^{-ip(x-y)}\,i(\not{p}+m)\left\{\frac{\theta(|\vec{p}|-k_F)}{p^2-m^2+i\epsilon} + \frac{\theta(k_F-|\vec{p}|)}{p^2-m^2-i\epsilon}\right\} \\ &= \int \frac{\mathrm{d}^4p}{(2\pi)^4}e^{-ip(x-y)}\,i(\not{p}+m)\Bigg\{\frac{1}{p^2-m^2+i\epsilon} \\ &\qquad +\theta(k_F-|\vec{p}|)\left[\frac{1}{p^2-m^2-i\epsilon} - \frac{1}{p^2-m^2+i\epsilon}\right]\Bigg\} \ . \end{aligned} \tag{A.15}$$

We use the formulae

$$\frac{1}{x \pm i\epsilon} = \frac{1}{x} \mp i\pi\delta(x) \tag{A.16}$$

to finally write:

$$S_F(x-y) = \int \frac{\mathrm{d}^4p}{(2\pi)^4} e^{-ip(x-y)} \, (\not{p} + m) \left[\frac{i}{p^2 - m^2 + i\epsilon} - 2\pi\delta(p^2 - m^2)\theta(k_F - |\vec{p}|)\theta(p_0) \right] . \tag{A.17}$$

The in-medium propagator consists of two terms. The first term is identical to the vacuum propagator, the second one takes into account the presence of the medium, confining its action to momenta $|\vec{p}| < k_F$, and is called medium insertion. In it, the delta of Dirac sets the fermion on the mass shell; $\theta(p_0)$ is added to ensure that $p_0 > 0$ according to our convention.

A.2 In-Medium Fermion Propagator at Finite Temperature

At finite temperature T the thermal expectation value of an operator $\hat{A}$ is defined as:

$$\langle \hat{A} \rangle_\beta = \frac{1}{Z(\beta)} \mathrm{Tr}\Big\{ e^{-\beta(\hat{H} - \mu\hat{N})} \hat{A} \Big\} \ , \tag{A.18}$$

with $Z(\beta) = \mathrm{Tr}\{e^{-\beta(\hat{H}-\mu\hat{N})}\}$ the grand-canonical partition function. $\hat{H}$ is the Hamiltonian operator of the system, $\hat{N}$ the particle number operator, μ the chemical potential and $\beta = 1/T$. In the following we neglect the hut in the operators for simplicity.

First we consider the case $\mu = 0$. The results can then be generalize to finite μ. We define the fermion propagator as:

$$S^F_\beta(x-y) = \langle\, T[\psi(x)\bar{\psi}(y)] \,\rangle_\beta \tag{A.19}$$

$$= \theta(x_0 - y_0)\, S^>_\beta(x-y) + \theta(y_0 - x_0)\, S^<_\beta(x-y) \ , \tag{A.20}$$

where the advanced and retarded propagators are

$$S^>_\beta(x-y) = \langle \psi(x)\bar{\psi}(y) \rangle_\beta \ , \qquad S^<_\beta(x-y) = -\langle \bar{\psi}(y)\psi(y) \rangle_\beta \ . \tag{A.21}$$

Combining the Fourier transform definition

$$S^F_\beta(p) = \int \mathrm{d}^4x \, e^{-ipx} S^F_\beta(x) \tag{A.22}$$

and the Kubo-Martin-Schwinger (KMS) relation

$$S^>_\beta(x_0, \vec{x}; y_0, \vec{y}) = -S^<_\beta(x_0 + i\beta, \vec{x}; y_0, \vec{y}) \ , \tag{A.23}$$

it is possible to find a relation between advanced and retarded propagator:

$$S^<_\beta(p) = -e^{-\beta p_0} S^>_\beta(p) \ . \tag{A.24}$$

The spectral function is defined as:

$$\rho(p) = S^>_\beta(p) - S^<_\beta(p) \ . \tag{A.25}$$

Substituting Eq. (A.24) in it, we find:

$$S^<_\beta(p) = -n_F(p_0)\rho(p) \ , \qquad S^>_\beta(p) = [1 - n_F(p_0)]\rho(p) \ , \tag{A.26}$$

where $n_F(p_0) = [e^{\beta p_0} + 1]^{-1}$ is the Fermi distribution function.

We can now obtain the spectral representation of the fermion propagator. Consider the fermion propagator in momentum space:

$$S^F_\beta(p) = \int \mathrm{d}^4x\, e^{ipx} \left[\theta(x_0) S^>_\beta(x) + \theta(-x_0) S^<_\beta(x)\right] \ . \tag{A.27}$$

Using Eq. (A.13), the definition (A.22) and the relations (A.26), we get:

$$S^F_\beta(p) = i \int \frac{\mathrm{d}p'_0}{2\pi} \frac{\rho(p'_0, \vec{p})}{p_0 - p'_0 + i\epsilon} - n_F(p_0)\, \rho(p) \ . \tag{A.28}$$

At this point we need the spectral function $\rho(p)$. This can be calculated using the imaginary-time (Matsubara) propagator and performing an analytic continuation to continuous values of the Matsubara frequencies.

In the imaginary-time formalism, after the substitution $x_0 \to -i\tilde{x}_0$, the propagator takes the form:

$$\begin{aligned} S^F_\beta[-i(\tilde{x}_0 - \tilde{y}_0), \vec{x} - \vec{y}] = \theta(\tilde{x}_0 - \tilde{y}_0)\ S^>_\beta[-i(\tilde{x}_0 - \tilde{y}_0), \vec{x} - \vec{y}] \\ + \theta(\tilde{y}_0 - \tilde{x}_0)\ S^<_\beta[-i(\tilde{x}_0 - \tilde{y}_0), \vec{x} - \vec{y}] \ . \end{aligned} \tag{A.29}$$

Let us define

$$\Delta_\beta(\tilde{x}_0, \vec{x}) = S_\beta(-i\tilde{x}_0, \vec{x}) \ . \tag{A.30}$$

The Matsubara propagator is defined in the interval $0 \le \tilde{x}_0 \le \beta$ and is antiperiodic:

$$\Delta_\beta(\tilde{x}_0, \vec{x}) = -\Delta_\beta(\tilde{x}_0 - \beta, \vec{x}) \ . \tag{A.31}$$

We define the Fourier transform

$$\Delta(i\omega_n, \vec{p}) = \int_0^\beta \mathrm{d}\tilde{x}_0 \int \mathrm{d}^3x\ e^{i\omega_n \tilde{x}_0} e^{-i\vec{p}\cdot\vec{x}}\, \Delta(\tilde{x}_0, \vec{x}) \tag{A.32}$$

and its inverse

$$\Delta(\tilde{x}_0, \vec{x}) = \frac{1}{\beta} \sum_n \int \mathrm{d}^3p\ e^{-i\omega_n \tilde{x}_0} e^{i\vec{p}\cdot\vec{x}}\, \Delta(i\omega_n, \vec{p}) \ . \tag{A.33}$$

Due to the antiperiodicity and the finite interval $[0, \beta]$, the frequencies take discrete values:

$$\omega_n = \frac{(2n+1)\pi}{\beta} \ . \tag{A.34}$$

Consider

$$\Delta(\tilde{x}_0, \vec{x}) = S^>_\beta(-i\tilde{x}_0, \vec{x}) = \int_{-\infty}^{\infty} \frac{\mathrm{d}p_0}{2\pi}\, e^{-p_0\tilde{x}_0} \int \frac{\mathrm{d}^3p}{(2\pi)^3}\, e^{i\vec{p}\cdot\vec{x}}\, S^>_\beta(p_0, \vec{p}) \ . \tag{A.35}$$

Using eqs. (A.35) and (A.26), the spectral representation of the Matsubara propagator (A.32) results:

$$\Delta(i\omega_n, \vec{p}) = \int_{-\infty}^{\infty} \frac{\mathrm{d}p_0}{2\pi} \frac{\rho(p_0, \vec{p})}{p_0 - i\omega_n} \ . \tag{A.36}$$

To invert the relation and determine $\rho(p)$, we extend $\Delta(i\omega_n, \vec{p})$ to a continuous function $\Delta(p_0, \vec{p})$:

$$\rho(p) = \Delta(p_0 + i\epsilon, \vec{p}) - \Delta(p_0 - i\epsilon, \vec{p}) \ . \tag{A.37}$$

Comparing with Eq. (A.25), we note that the Matsubara propagator returns the advanced and retarded real-time propagator with the replacement $i\omega_n \to p_0 \pm i\epsilon$.

The explicit form of the Matsubara propagator can be obtained Fourier-transforming the kernel of the Dirac equation in imaginary time:

$$(i\partial\!\!\!/ - m)\Delta_\beta(\tilde{x}_0, \vec{x}) = i\delta(\tilde{x}_0)\delta^3(\vec{x}) \ . \tag{A.38}$$

One finds:

$$\Delta_\beta(i\omega_n, \vec{p}) = \frac{i}{i\omega_n\gamma_0 - \vec{p}\cdot\vec{\gamma} - m} \ . \tag{A.39}$$

The spectral function results:

$$\begin{aligned}\rho(p) &= i(p\!\!\!/ + m)\left[\frac{1}{p^2 - m^2 + i\epsilon\,\mathrm{sgn}(p_0)} - \frac{1}{p^2 - m^2 - i\epsilon\,\mathrm{sgn}(p_0)}\right] \\ &= 2\pi\,\mathrm{sgn}(p_0)\,(p\!\!\!/ + m)\,\delta(p^2 - m^2) \ .\end{aligned} \tag{A.40}$$

After replacing in Eq. (A.28), we obtain the fermion propagator in real-time formalism [126]:

$$S_\beta(p) = (p\!\!\!/ + m)\left[\frac{i}{p^2 - m^2 + i\epsilon} - 2\pi\, n_F(p_0)\,\delta(p^2 - m^2)\right] \ . \tag{A.41}$$

We can naively generalize the fermion propagator to the case $\mu \neq 0$ on the basis of simple considerations.

In the creation/destruction-operator formalism, the operator $K = H - \mu N$ is:

$$K = \int \frac{\mathrm{d}^3 p}{(2\pi)^3} \sum_{s=1,2} (p'_0 - \mu)\left[a^{\dagger s}_{\vec{p}}\, a^s_{\vec{p}} + b^{\dagger s}_{\vec{p}}\, b^s_{\vec{p}}\right] \ . \tag{A.42}$$

It implies for the real-time formalism the replacement:

$$p_0 \longrightarrow p'_0 - \mu \ . \tag{A.43}$$

Note that p_0 is associated to the operator $-i\partial/\partial x_0$, which becomes $\partial/\partial\tilde{x}_0$ in the imaginary-time formalism and $-i\omega_n$ in momentum space. Therefore, $i\omega_n \longrightarrow i\omega'_n + \mu$. The fermion propagator in real time becomes [127, 128]:

$$S_\beta(p') = (p\!\!\!/' + m)\left[\frac{i}{p'^2 - m^2 + i\epsilon} - 2\pi\, n_F(p'_0 - \mu)\,\delta(p'^2 - m^2)\right] \ , \tag{A.44}$$

with $p' \equiv (p'_0 = p_0 + \mu, \vec{p})$. The delta of Dirac states that $p'_0 = E = \sqrt{\vec{p}^2 + m^2}$.

As a remarkable result, the propagator is split in a zero-temperature and in a temperature-dependent part.

Appendix B

Contributions to the Free Energy Density

In this appendix we summarize the diagrammatic contributions to the free energy density by reporting the explicit expressions of the kernels for the convolution integrals Eq. (4.20). For further details and explanations see Refs. [55, 76, 80].

B.1 Isospin-Symmetric Nuclear Matter

One-body kernel

$$\mathcal{K}_1(p) = \mu_0 - \frac{p^2}{3M_N} - \frac{p^4}{8M_N^3} \ , \tag{B.1}$$

where μ_0 is the effective one-body chemical potential and $M_N = 939$ MeV is the free nucleon mass.

Two-body kernels

- Contact terms:

$$\mathcal{K}_2^{(ct)}(p_1,p_2) = 24\pi^2 B_3 \frac{p_1\,p_2}{M_N^2} + 20\pi^2 B_5 \frac{p_1\,p_2}{M_N^4}(p_1^2+p_2^2) \ , \tag{B.2}$$

  with $B_3 = -7.99$ and $B_5 = 0$.

- 1π-exchange Fock-diagram:

$$\mathcal{K}_2^{(1\pi)}(p_1,p_2) = \frac{3\,g_A^2}{16 f_\pi^2}\left\{8\,p_1\,p_2 - 2\,m_\pi^2 \ln\frac{f_+(p_1,p_2)}{f_-(p_1,p_2)} + \frac{1}{M_N^2}\left[-4\,p_1\,p_2(p_1^2+p_2^2)\right.\right.$$
$$\left.\left. + m_\pi^2(p_1^2+p_2^2)\ln\frac{f_+(p_1,p_2)}{f_-(p_1,p_2)} - \frac{2\,m_\pi^2\,p_1\,p_2(p_1^2-p_2^2)^2}{f_+(p_1,p_2)\,f_-(p_1,p_2)}\right]\right\} \ , \tag{B.3}$$

  with

$$f_+(p_1,p_2) = m_\pi^2 + (p_1+p_2)^2 \ , \qquad f_-(p_1,p_2) = m_\pi^2 + (p_1-p_2)^2 \ . \tag{B.4}$$

- Iterated 1π-exchange Hartree-diagram:

$$\mathcal{K}_2^{(\mathrm{it}H)}(p_1,p_2) = \frac{3\,g_A^4 M_N m_\pi^2}{8\pi f_\pi^4}\left\{(p_1+p_2)\arctan\frac{p_1+p_2}{m_\pi}\right.$$
$$\left. + (p_2-p_1)\arctan\frac{p_1-p_2}{m_\pi} - \frac{5}{8}m_\pi \ln\frac{f_+(p_1,p_2)}{f_-(p_1,p_2)}\right\} \ . \tag{B.5}$$

- Iterated 1π-exchange Fock-diagram:

$$\mathcal{K}_2^{(\mathrm{it}F)}(p_1,p_2) = \frac{3\,g_A^4 M_N m_\pi}{32\pi f_\pi^4}\left\{2\,p_1\,p_2 + m_\pi^2\int_{\frac{|p_1-p_2|}{2m_\pi}}^{\frac{p_1+p_2}{2m_\pi}}\frac{\mathrm{d}x}{1+2x^2}\left[(1+8x^2+8x^4)\arctan x - (1+4x^2)\arctan 2x\right]\right\}\ . \quad \text{(B.6)}$$

- Irreducible 2π-exchange Fock-diagram:

$$\mathcal{K}_2^{(\mathrm{irr}F)}(p_1,p_2) = \frac{1}{\pi}\int_{2m_\pi}^{\infty}\mathrm{d}\mu\,\mathrm{Im}(V_C+3W_C+2\mu^2V_T+6\mu^2W_T) \times\left\{\mu\ln\frac{f_+(p_1,p_2)}{f_-(p_1,p_2)} - \frac{4\,p_1\,p_2}{\mu} + \frac{4\,p_1\,p_2}{\mu^3}(p_1^2+p_2^2)\right\}\ , \quad \text{(B.7)}$$

where $\mathrm{Im}V_C, \mathrm{Im}W_C, \mathrm{Im}V_T, \mathrm{Im}W_T$ are the spectral functions of the isoscalar and isovector central and tensor NN-amplitudes [52]. They are given by:

$$\mathrm{Im}V_C(\mu) = \frac{1}{\pi}(V_{Cb1}+V_{Cb2})\ , \quad \text{(B.8)}$$

$$\mathrm{Im}W_C(\mu) = \frac{1}{\pi}(W_{Cir}+W_{Ctr}+W_{Cb1}+W_{Cb2})\ , \quad \text{(B.9)}$$

$$\mathrm{Im}V_T(\mu) = \frac{1}{\pi}(V_{Tir}+V_{Tb1}+V_{Tb2})\ , \quad \text{(B.10)}$$

$$\mathrm{Im}W_T(\mu) = \frac{1}{\pi}(W_{Tb1}+W_{Tb2})\ , \quad \text{(B.11)}$$

where the contributions from the different diagrams are separated:

  - From irreducible 2π-exchange:

$$W_{Cir}(\mu) = \frac{1}{3\mu(4f_\pi)^4}\left\{\left[4\,m_\pi^2(1+4g_A^2-5g_A^4)+\mu^2(23g_A^4-10g_A^2-1)\right] \times\sqrt{\mu^2-4m_\pi^2} + \frac{48m_\pi^4g_A^4}{\sqrt{\mu^2-4m_\pi^2}}\right\}\ , \quad \text{(B.12)}$$

$$V_{Tir}(\mu) = -6\left(\frac{g_A}{4f_\pi}\right)^4\frac{\sqrt{\mu^2-4m_\pi^2}}{\mu}\ . \quad \text{(B.13)}$$

  - From the Δ triangle diagram:

$$L_q = -\frac{\sqrt{\mu^2-4m_\pi^2}}{2\mu}\ , \qquad D_q = \frac{1}{2\mu\Delta}\arctan\frac{\sqrt{\mu^2-4m_\pi^2}}{2\Delta}\ , \quad \text{(B.14)}$$

$$\sigma = 2m_\pi^2-\mu^2-2\Delta^2\ , \qquad W_2 = 4m_\pi^2-\mu^2\ , \quad \text{(B.15)}$$

$$W_{Ctr}(\mu) = \frac{g_A^2}{192f_\pi^4}\left\{[6\,\sigma-W_2]\,L_q + 12\,\Delta^2\,\sigma D_q\right\}\ . \quad \text{(B.16)}$$

  - From the single-Δ box diagram:

$$V_{Cb1}(\mu) = \frac{3\,g_A^4}{32f_\pi^4\Delta}(2\,m_\pi^2-\mu^2)^2\frac{\pi}{4\mu}\ , \quad \text{(B.17)}$$

$$W_{Cb1}(\mu) = \frac{g_A^4}{192f_\pi^4}\left[(12\Delta^2-20\,m_\pi^2+11\mu^2)L_q + 6\,\sigma^2 D_q\right]\ , \quad \text{(B.18)}$$

$$V_{Tb1}(\mu) = \frac{3\,g_A^4}{128f_\pi^4}\left\{-2\,L_q + \left[W_2-4\Delta^2\right]D_q\right\}\ , \quad \text{(B.19)}$$

$$W_{Tb1}(\mu) = \frac{g_A^4}{128f_\pi^4\Delta}W_2\frac{\pi}{4\mu}\ . \quad \text{(B.20)}$$

– From the double-Δ box diagram:

$$H_q = 2\,\frac{\sigma\,L_q}{W_2-4\Delta^2}\ , \tag{B.21}$$

$$V_{Cb2}(\mu) = \frac{3\,g_A^4}{64 f_\pi^4}\left\{-4\Delta^2 L_q + \sigma\left[H_q + \left(\sigma+8\Delta^2\right)D_q\right]\right\}\ , \tag{B.22}$$

$$W_{Cb2}(\mu) = \frac{g_A^4}{384 f_\pi^4}\left\{\left[12\,\sigma - W_2\right]L_q + 3\,\sigma\left[H_q + \left(8\Delta^2-\sigma\right)D_q\right]\right\}\ , \tag{B.23}$$

$$V_{Tb2}(\mu) = \frac{3\,g_A^4}{512 f_\pi^4}\left\{6\,L_q + \left[12\Delta^2 - W_2\right]D_q\right\}\ , \tag{B.24}$$

$$W_{Tb2}(\mu) = \frac{g_A^4}{1024 f_\pi^4}\left\{2\,L_q + \left[4\Delta^2 + W_2\right]D_q\right\}\ . \tag{B.25}$$

Three-body kernels

- Iterated 1π-exchange Hartree-diagram:

$$\mathcal{K}_3^{(\mathrm{it}H)}(p_1,p_2,p_3) = \frac{3\,g_A^4 M_N}{4 f_\pi^4}\int\limits_{|p_1-p_2|}^{p_1+p_2}\mathrm{d}q\,\frac{q^4}{(m_\pi^2+q^2)^2}\ln\frac{|p_1^2-p_2^2+q^2+2\,p_3 q|}{|p_1^2-p_2^2+q^2-2\,p_3 q|}\ . \tag{B.26}$$

- Iterated 1π-exchange Fock-diagram:

$$\begin{aligned}\mathcal{K}_3^{(\mathrm{it}F)}(p_1,p_2,p_3) = \frac{3\,g_A^4 M_N}{16 f_\pi^4}\Bigg\{&\frac{1}{8\,p_3^3}\left[4\,p_1 p_3 + \left(p_3^2-p_1^2-m_\pi^2\right)\ln\frac{f_+(p_1,p_3)}{f_-(p_1,p_3)}\right]\\ &\times\left[4\,p_2\,p_3 + \left(p_3^2-p_2^2-m_\pi^2\right)\ln\frac{f_+(p_2,p_3)}{f_-(p_2,p_2)}\right]\\ +\int\limits_{|p_2-p_3|}^{p_2+p_3}&\mathrm{d}q\,\frac{q^2}{m_\pi^2+q^2}\left[\ln\frac{|p_1+h|}{|p_2-h|}+\frac{m_\pi^2}{R}\ln\frac{|p_1 R+(p_1^2-p_3^2-m_\pi^2)h|}{|p_1 R+(p_3^2+m_\pi^2-p_1^2)h|}\right]\Bigg\}\ ,\end{aligned} \tag{B.27}$$

$$h = \frac{1}{2q}\left(p_2^2-p_3^2-q^2\right)\ ,\qquad R = \sqrt{\left(m_\pi^2+p_1^2-p_3^2\right)^2+4m_\pi^2\left(p_3^2-h^2\right)}\ . \tag{B.28}$$

- 2π-exchange three-body Hartree-diagram with single Δ-isobar excitation:

$$\begin{aligned}\mathcal{K}_3^{(\Delta\,H)}(p_1,p_2,p_3) = \frac{3\,g_A^4\,p_3}{\Delta f_\pi^4}\Bigg\{&2\,p_1 p_2\,(1+\zeta) + \frac{2m_\pi^4\,p_1 p_2}{f_+(p_1,p_2)\,f_-(p_1,p_2)}\\ &-m_\pi^2\ln\frac{f_+(p_1,p_2)}{f_-(p_1,p_2)}\Bigg\}\ ,\end{aligned} \tag{B.29}$$

  including the contact term with $\zeta = -3/4$.

- 2π-exchange three-body Fock-diagram with single Δ-isobar excitation:

$$\mathcal{K}_3^{(\Delta\,F)}(p_1,p_2,p_3) = -\frac{g_A^4}{4\Delta f_\pi^4\,p_3}\left[2\,X(p_1,p_3)X(p_2,p_3)+Y(p_1,p_3)Y(p_2,p_3)\right]\ , \tag{B.30}$$

$$X(p_1,p_3) = 2\,p_1 p_3 - \frac{m_\pi^2}{2}\ln\frac{f_+(p_1,p_3)}{f_-(p_1,p_3)}\ , \tag{B.31}$$

$$Y(p_1,p_3) = \frac{p_1}{4\,p_3}\left(5\,p_3^2-3m_\pi^2-3\,p_1^2\right)+\frac{3\,(p_1^2-p_3^2+m_\pi^2)^2+4m_\pi^2\,p_3^2}{16\,p_3^2}\ln\frac{f_+(p_1,p_3)}{f_-(p_1,p_3)}\ . \tag{B.32}$$

Anomalous contribution

$$\rho\bar{\mathcal{A}}(\rho,T) = -\frac{\left[\Omega'_{1\pi}(\rho,T)\right]^2}{2\Omega''_0(\rho,T)} + \frac{9\,g_A^4}{8f_\pi^4 T}\int_0^\infty \mathrm{d}p_1 \int_0^\infty \mathrm{d}p_2 \int_0^\infty \mathrm{d}p_3\, d(p_1)\, d(p_2)\left[2\pi^2 d(p_2) - p_2\right] d(p_3) \times \left[p_1 - \frac{m_\pi^2}{4\,p_2}\ln\frac{f_+(p_1,p_2)}{f_-(p_1,p_2)}\right]\left[p_3 - \frac{m_\pi^2}{4\,p_2}\ln\frac{f_+(p_3,p_2))^2}{f_-(p_3,p_2)}\right] , \quad \text{(B.33)}$$

with

$$\Omega'_{1\pi}(\rho,T) = \frac{3\,g_A^2 M_N}{2f_\pi^2}\int_0^\infty \mathrm{d}p_1 \int_0^\infty \mathrm{d}p_2\, d(p_1)\frac{d(p_2)}{p_2}\left[\frac{(p_1+p_2)^3}{f_+(p_1,p_2)} + \frac{(p_1-p_2)^3}{f_-(p_1,p_2)}\right] , \quad \text{(B.34)}$$

$$\Omega''_0(\rho,T) = -4M_N\int_0^\infty \mathrm{d}p\,\frac{d(p)}{p} = \sqrt{2T}\left(\frac{M}{\pi}\right)^{3/2}\mathrm{Li}_{1/2}(-e^{\mu_0/T}) . \quad \text{(B.35)}$$

B.2 Isospin-Asymmetric Nuclear Matter

In isospin-asymmetric nuclear matter the Fermi momenta and the "one-body" chemical potentials of protons and neutrons are different. As a consequence, Eq. (4.20) has to be modified, by taking into account that

- for each closed diagram we sum over all possible combinations of protons and neutrons, each combination multiplied by its own isospin factor;
- the densities of states $d_p(q)$ and $d_n(q)$ are different due to different μ_{0p} and μ_{0n}. Note that the momenta to be integrated over are now denoted by the symbol q instead of p.

One-body kernel

The integration over the proton and neutron distributions have to be performed separately, resulting in the following replacement in Eqs. (4.20) and (B.1):

$$4\int_0^\infty \mathrm{d}q\, q\,\mathcal{K}_1(q)d(q) \longrightarrow 2\int_0^\infty \mathrm{d}q\, q\left[\mathcal{K}_1^{(p)}(q)d_p(q) + \mathcal{K}_1^{(n)}(q)d_n(q)\right] , \quad \text{(B.36)}$$

where $\mathcal{K}_1^{(p,n)}(q) = \mu_{0p,n} - \dfrac{q^2}{3M_N} - \dfrac{q^4}{8M_N^3}$.

Two-body kernels

- 1π-exchange Fock-diagram.
  Using $\mathcal{K}_2^{(1\pi)}$ of Eq. (B.3) the product $d(q_1)d(q_2)$ for isospin-symmetric nuclear matter is replaced by:

$$d(q_1)d(q_2) \longrightarrow \frac{1}{6}\left[d_p(q_1)d_p(q_2) + d_n(q_1)d_n(q_2) + 4\,d_p(q_1)d_n(q_2)\right] . \quad \text{(B.37)}$$

- Iterated 1π-exchange Hartree-diagram.
  Using $\mathcal{K}_2^{(\mathrm{it}H)}$ from Eq. (B.5), replace in the corresponding integral:

$$d(q_1)\,d(q_2) \longrightarrow \frac{1}{12}\left[d_p(q_1)\,d_p(q_2) + d_n(q_1)\,d_n(q_2) + 10\,d_p(q_1)\,d_n(q_2)\right] . \quad \text{(B.38)}$$

- Iterated 1π-exchange Fock-diagram.
  Using $\mathcal{K}_2^{(\mathrm{it}F)}$ from Eq. (B.6), replace in the corresponding integral:

$$d(q_1)\,d(q_2) \longrightarrow \frac{1}{6}\left[8\,d_p(q_1)\,d_n(q_2) - d_p(q_1)\,d_p(q_2) - d_n(q_2)\,d_n(q_2)\right] . \tag{B.39}$$

- Irreducible 2π-exchange.
  For isoscalar amplitude $V_{C,T}$ in Eq. (B.7), replace:

$$d(q_1)\,d(q_2) \longrightarrow \frac{1}{2}\left[d_p(q_1)\,d_p(q_2) + d_n(q_1)\,d_n(q_2)\right] . \tag{B.40}$$

  For isovector amplitude $W_{C,T}$ in Eq. (B.7), replace:

$$d(q_1)\,d(q_2) \longrightarrow \frac{1}{6}\left[d_p(q_1)\,d_p(q_2) + d_n(q_1)\,d_n(q_2) + 4\,d_p(q_1)d_n(q_2)\right] . \tag{B.41}$$

- Contact terms.
  Expressions for symmetric nuclear matter using $\mathcal{K}_2^{(ct)}$ of Eq. (B.2) are replaced as follows:

$$B_3\,d(q_1)\,d(q_2) \longrightarrow (B_3 - B_{n,3})\,d_p(q_1)\,d_n(q_2) + \frac{1}{2}B_{n,3}\Big[d_p(q_1)\,d_p(q_2) + d_n(q_1)\,d_n(q_2)\Big] , \tag{B.42}$$

$$B_5\,d(q_1)\,d(q_2) \longrightarrow (B_5 - B_{n,5})\,d_p(q_1)\,d_n(q_2) + \frac{1}{2}B_{n,5}\Big[d_p(q_1)\,d_p(q_2) + d_n(q_1)\,d_n(q_2)\Big] , \tag{B.43}$$

  with $B_{n,3} = -0.95$, $B_{n,5} = -3.58$.

Three-body kernels

- Iterated 1π-exchange Hartree-diagram.
  Using $\mathcal{K}_3^{(\mathrm{it}H)}$ from Eq. (B.26), replace in the corresponding integral:

$$d(q_1)\,d(q_2)\,d(q_3) \longrightarrow \frac{1}{12}\Big[d_p(q_1)\,d_p(q_2)\,d_p(q_3) + d_n(q_1)\,d_n(q_2)\,d_n(q_3) + d_p(q_1)\,d_p(q_2)\,d_n(q_3) + d_n(q_1)\,d_n(q_2)\,d_p(q_3) + 4\,d_n(q_1)\,d_p(q_2)\,d_n(q_3) + 4\,d_p(q_1)\,d_n(q_2)\,d_p(q_3)\Big] . \tag{B.44}$$

- Iterated 1π-exchange Fock-diagram.
  Using $\mathcal{K}_3^{(\mathrm{it}F)}$ from Eq. (B.27) , replace in the corresponding integral:

$$d(q_1)\,d(q_2)\,d(q_3) \longrightarrow \frac{1}{6}\Big[2\,d_p(q_1)\,d_n(q_2)\,d_p(q_3) + 2\,d_p(q_1)\,d_n(q_2)\,d_n(q_3) - d_p(q_1)\,d_p(q_2)\,d_p(q_3) + 2\,d_n(q_1)\,d_p(q_2)\,d_p(q_3) + 2\,d_n(q_1)\,d_p(q_2)\,d_n(q_3) - d_n(q_1)\,d_n(q_2)\,d_n(q_3)\Big] . \tag{B.45}$$

- Irreducible 2π-exchange Hartree-diagram with single Δ-isobar excitation.
  Using $\mathcal{K}_3^{(\Delta\,H)}$ from Eq. (B.29), replace in the corresponding integral:

$$d(q_1)\,d(q_2)\,d(q_3) \longrightarrow \frac{1}{12}\Big[d_p(q_3) + d_n(q_3)\Big]\Big[d_p(q_1)\,d_p(q_2) + d_n(q_1)\,d_n(q_2) + 4\,d_p(q_1)\,d_n(q_2)\Big] , \tag{B.46}$$

  The three-body contact term proportional to ζ is excluded from this formula, because it transforms differently:

$$\zeta\,d(q_1)\,d(q_2)\,d(q_3) \longrightarrow \zeta\,\frac{1}{2}d_p(q_1)\,d_n(q_2)[d_p(q_3) + d_n(q_3)] . \tag{B.47}$$

- Irreducible 2π-exchange Fock-diagram with single Δ-isobar excitation.
  Expressions for symmetric nuclear matter using $\mathcal{K}_3^{(\Delta\, F)}$ of Eq. (B.30) are replaced as follows:

$$
\begin{aligned}
&2\,X(q_1,q_3)X(q_2,q_3)\,d(q_1)\,d(q_2)\,d(q_3) \longrightarrow \frac{1}{6}X(q_1,q_3)X(q_2,q_3)\times\\
&\Big[d_p(q_1)\,d_p(q_2)\,d_p(q_3)+d_p(q_1)\,d_n(q_2)\,d_p(q_3)+d_n(q_1)\,d_p(q_2)\,d_p(q_3)+3\,d_n(q_1)\,d_n(q_2)\,d_p(q_3)\\
&+d_n(q_1)\,d_n(q_2)\,d_n(q_3)+d_n(q_1)\,d_p(q_2)\,d_n(q_3)+d_p(q_1)\,d_n(q_2)\,d_n(q_3)+3\,d_p(q_1)\,d_p(q_2)\,d_n(q_3)\Big]\,,
\end{aligned}
$$

$$
\begin{aligned}
&Y(q_1,q_3)Y(q_2,q_3)\,d(q_1)\,d(q_2)\,d(q_3) \longrightarrow \frac{1}{6}Y(q_1,q_3)Y(q_2,q_3)\times\\
&\Big[2\,d_p(q_1)\,d_p(q_2)\,d_p(q_3)-d_p(q_1)\,d_n(q_2)\,d_p(q_3)-d_n(q_1)\,d_p(q_2)\,d_p(q_3)-3\,d_n(q_1)\,d_n(q_2)\,d_p(q_3)\\
&+2\,d_n(q_1)\,d_n(q_2)\,d_n(q_3)-d_n(q_1)\,d_p(q_2)\,d_n(q_3)-d_p(q_1)\,d_n(q_2)\,d_n(q_3)+3\,d_p(q_1)\,d_p(q_2)\,d_n(q_3)\Big]\,,
\end{aligned}
\tag{B.48}
$$

  where $X(q_1,q_3)$ and $Y(q_1,q_3)$ are given in Eq. (B.31) and (B.32).

Anomalous term

The anomalous term is given by the sum of two terms transforming in a different way.

- Replace in the triple integral in Eq. (B.33):

$$
\begin{aligned}
&d(q_1)\,d(q_2)\left[2\pi^2 d(q_2)-q_2\right]d(q_3)\longrightarrow\\
&\quad\frac{1}{18}\Big\{d_p(q_1)\,d_p(q_3)\big\{d_p(q_2)[2\pi^2 d_p(q_2)-q_2]+4\,d_n(q_2)[2\pi^2 d_n(q_2)-q_2]\big\}\\
&\qquad+d_n(q_1)\,d_n(q_3)\big\{d_n(q_2)[2\pi^2 d_n(q_2)-q_2]+4\,d_p(q_2)[2\pi^2 d_p(q_2)-q_2]\big\}\\
&\qquad+4\,d_p(q_1)\,d_n(q_3)\big\{d_p(q_2)[2\pi^2 d_p(q_2)-q_2]+d_n(q_2)[2\pi^2 d_n(q_2)-q_2]\big\}\Big\}\,.
\end{aligned}
\tag{B.49}
$$

- The subtraction term in Eq. (B.33) transforms as:

$$
-\frac{[\Omega'_{1\pi}(\rho,T)]^2}{2\,\Omega''_0(\rho,T)}\longrightarrow-\frac{\left[\Omega'_{1\pi p}(\rho_p,\rho_n,T)\right]^2}{2\,\Omega''_{0p}(\rho_p,T)}-\frac{[\Omega'_{1\pi n}(\rho_p,\rho_n,T)]^2}{2\,\Omega''_{0n}(\rho_n,T)}
\tag{B.50}
$$

  with $\rho=\rho_p+\rho_n$ and

$$
\Omega''_{0p,n}(\rho_{p,n},T)=-2M_N\int_0^\infty \mathrm{d}q\,\frac{d_{p,n}(q)}{q}\,.
\tag{B.51}
$$

  Using $\Omega'_{1\pi}(\rho,T)$ defined in Eq. (B.34), $\Omega'_{1\pi p}$ is obtained replacing in the integral:

$$
d(q_1)\,d(q_2)\longrightarrow\frac{1}{6}\big[d_p(q_1)\,d_p(q_2)+2\,d_n(q_1)\,d_p(q_2)\big]\,.
\tag{B.52}
$$

  Using $\Omega'_{1\pi}(\rho,T)$ defined in Eq. (B.34), $\Omega'_{1\pi n}$ is obtained replacing in the integral:

$$
d(q_1)\,d(q_2)\longrightarrow\frac{1}{6}\big[d_n(q_1)\,d_n(q_2)+2\,d_p(q_1)\,d_n(q_2)\big]\,.
\tag{B.53}
$$

Appendix C

Contributions to the In-Medium Chiral Condensate

In this appendix we summarize the diagrammatic contributions to the chiral condensate of isospin-symmetric nuclear matter. We report the explicit expressions of the m_π^2-derivatives of the kernels of the convolution integrals in Appendix B.1. The dot denotes the derivative $\partial/\partial m_\pi^2$.

One-body kernel

From the one-body term eq. (B.1) with the addition of the nucleon mass M_N, we get:

$$\dot{K}_1(p) = \frac{\sigma_N}{m_\pi^2}\left[1 + \frac{3\rho}{2M_N\Omega_0''} + \frac{p^2}{3M_N^2} + \frac{3p^4}{8M_N^4}\right] , \tag{C.1}$$

We use:

$$\frac{\partial M_N}{\partial m_\pi^2} = \frac{\sigma_N}{m_\pi^2}, \qquad \frac{\partial \mu_0}{\partial m_\pi^2} = \frac{\sigma_N}{m_\pi^2}\frac{\partial \mu_0}{\partial M_N} . \tag{C.2}$$

The derivative $\partial\mu_0/\partial M_N$ is calculated using the condition $\rho = \text{const}$ against variations of any of its variables. Applying the variational principle to eq. (4.22), one finds:

$$\frac{\partial \mu_0}{\partial M_N} = -\frac{3\,T}{2M_N}\frac{\mathrm{Li}_{3/2}(-e^{\mu_0/T})}{\mathrm{Li}_{1/2}(-e^{\mu_0/T})} = \frac{3\rho}{2M_N\Omega_0''} , \tag{C.3}$$

with Ω_0'' given by eq. (B.35).

Two-body kernels

- 1π-exchange Fock-diagram.
  From eq. (B.3), one obtains:

$$\begin{aligned}\dot{K}_2^{(1\pi)}(p1,p2) = \frac{3g_A^2}{8f_\pi^2}\Bigg\{&\left[\frac{m_\pi^2}{f_-(p_1,p_2)} - \frac{m_\pi^2}{f_+(p_1,p_2)} - \ln\frac{f^+(p_1,p_2)}{f^-(p_1,p_2)}\right]\Gamma(m_\pi) \\ &+ \left[4p_1p_2 - m_\pi^2\,\ln\frac{f_+(p_1,p_2)}{f_-(p_1,p_2)}\right]\dot{\Gamma}(m_\pi) + \frac{1}{2M_N^2}\Bigg[(p_1^2+p_2^2)\,\ln\frac{f_+(p_1,p_2)}{f_-(p_1,p_2)} \\ &+ m_\pi^2(p_1^2+p_2^2)\left(\frac{1}{f_+(p_1,p_2)} - \frac{1}{f_-(p_1,p_2)}\right) + \frac{(p_1+p_2)^4(p_1-p_2)^2}{2\,f_+^2(p_1,p_2)} \\ &- \frac{(p_1-p_2)^4(p_1+p_2)^2}{2\,f_-^2(p_1,p_2)}\Bigg]\Bigg\} ,\end{aligned} \tag{C.4}$$

with

$$f_+(p_1,p_2) = m_\pi^2 + (p_1+p_2)^2 \ , \qquad f_-(p_1,p_2) = m_\pi^2 + (p_1-p_2)^2 \ . \tag{C.5}$$

The renormalization factor $\Gamma(m_\pi)$ is

$$\begin{aligned}\Gamma(m_\pi) = 1 &+ \frac{g_A^2 m_\pi^2}{(2\pi f_\pi)^2}\left[4\gamma + 1 - 2\,\ln\frac{m_\pi}{\lambda}\right] + \frac{g_A^2}{3\pi^2 f_\pi^2}\left\{\frac{\pi m_\pi^3}{\Delta} - \frac{m_\pi^2}{2}\right. \\ &\left. + (3m_\pi^2 - 2\Delta^2)\ln\frac{m_\pi}{2\Delta} - \frac{2}{\Delta}(\Delta^2 - m_\pi^2)^{\frac{3}{2}}\,\ln\frac{\Delta + \sqrt{\Delta^2 - m_\pi^2}}{m_\pi}\right\} \\ &+ \frac{9\,g_A^2}{(4\pi f_\pi)^2}\left\{m_\pi^2 + (4\Delta^2 - 2m_\pi^2)\,\ln\frac{m_\pi}{2\Delta} + 4\Delta\sqrt{\Delta^2 - m_\pi^2}\,\ln\frac{\Delta + \sqrt{\Delta^2 - m_\pi^2}}{m_\pi}\right\} \ ,\end{aligned} \tag{C.6}$$

and its derivative is given by

$$\begin{aligned}\dot\Gamma(m_\pi) = \frac{g_A^2}{(\pi f_\pi)^2}\left\{\gamma - \frac{1}{2}\ln\frac{m_\pi}{\lambda} + \frac{\pi m_\pi}{2\Delta} - \frac{1}{8}\,\ln\frac{m_\pi}{2\Delta} + \right. \\ \left. \left[\frac{\sqrt{\Delta^2 - m_\pi^2}}{\Delta} - \frac{9}{8}\frac{\Delta}{\sqrt{\Delta^2 - m_\pi^2}}\right]\ln\frac{\Delta + \sqrt{\Delta^2 - m_\pi^2}}{m_\pi}\right\} \ ,\end{aligned} \tag{C.7}$$

with $\gamma = -1.505$ at the regularization scale $\lambda = M_N = 882$ MeV.

- Pion self-energy and l_3-contact term.
  From the diagrams (f) and (g) of Fig. 5.1, we obtain:

$$\begin{aligned}\dot{\mathcal{K}}_2^{(\mathrm{self})}(p_1,p_2) = \frac{3g_A^2 m_\pi^2}{(8\pi)^2 f_\pi^4}\left\{\left(32\pi^2 l_3^r + \ln\frac{m_\pi}{\lambda}\right)\left[\frac{m_\pi^4}{2}\left(\frac{1}{f_+^2(p_1,p_2)} - \frac{1}{f_-^2(p_1,p_2)}\right)\right.\right. \\ \left. + 2m_\pi^2\left(\frac{1}{f_-(p_1,p_2)} - \frac{1}{f_+(p_1,p_2)}\right) - \ln\frac{f_+(p_1,p_2)}{f_-(p_1,p_2)}\right] \\ \left. - \frac{1}{4}\,\ln\frac{f_+(p_1,p_2)}{f_-(p_1,p_2)} + \frac{m_\pi^2}{4}\left[\frac{1}{f_-(p_1,p_2)} - \frac{1}{f_+(p_1,p_2)}\right]\right\} \ ,\end{aligned} \tag{C.8}$$

  with the low-energy constant l_3^r determined through the relation $\bar{l}_3 = -64\pi^2 l_3^r - 2\ln(m_\pi/\lambda) \simeq 3$ [111].

- Iterated 1π-exchange Hartree-diagram.
  From eq. (B.5), one obtains:

$$\begin{aligned}\dot{\mathcal{K}}_2^{(\mathrm{it}H)}(p_1,p_2) = \frac{3g_A^4 M_N}{8\pi f_\pi^4}\left\{(p_1+p_2)\arctan\frac{p_1+p_2}{m_\pi} + (p_2-p_1)\arctan\frac{p_1-p_2}{m_\pi}\right. \\ \left. - \frac{15}{16}m_\pi\ln\frac{f_+(p_1,p_2)}{f_-(p_1,p_2)} + \frac{m_\pi^3}{8}\left[\frac{1}{f_-(p_1,p_2)} - \frac{1}{f_+(p_1,p_2)}\right]\right\} \ .\end{aligned} \tag{C.9}$$

- Iterated 1π-exchange Fock-diagram.
  From eq. (B.6), one obtains:

$$\begin{aligned}\dot{\mathcal{K}}_2^{(\mathrm{it}F)} = \frac{3g_A^4 M_N}{64\pi f_\pi^4}\left\{\frac{2}{m_\pi}\,p_1 p_2 + 3m_\pi\int_{\frac{p_1-p_2}{2m_\pi}}^{\frac{p_1+p_2}{2m_\pi}}\mathrm{d}x\, f(x)\right. \\ \left. - \frac{1}{2}(p_1+p_2)\ f\left(\frac{p_1+p_2}{2m_\pi}\right) + \frac{1}{2}(p_1-p_2)\ f\left(\frac{p_1-p_2}{2m_\pi}\right)\right\} \ ,\end{aligned} \tag{C.10}$$

with

$$f(x) = \frac{1}{1+2x^2}\left[(1+8x^2+8x^4)\arctan x - (1+4x^2)\arctan 2x\right] \ . \tag{C.11}$$

- Irreducible 2π-exchange with only nucleon intermediate states.
From eq. (8) in Ref. [80], one obtains:

$$\dot{\mathcal{K}}_2^{2\pi}(p_1,p_2) = \frac{3m_\pi^2}{64\pi^2 f_\pi^4}\left\{I\left(\frac{p_1+p_2}{2m_\pi}\right) - I\left(\frac{p_1-p_2}{2m_\pi}\right)\right\} \ , \tag{C.12}$$

with

$$\begin{aligned} I(x) = {} & (11g_A^4 - 2g_A^2 - 1)\,\ln^2(x+\sqrt{1+x^2}) \\ & + 2x\left[(7g_A^4 - 6g_A^2 - 1)\sqrt{1+x^2} - \frac{2g_A^4}{\sqrt{1+x^2}}\right]\ln(x+\sqrt{1+x^2}) \\ & + 2x^2\left[1 + 4g_A^2 - 3g_A^4 + (15g_A^4 - 6g_A^2 - 1)\ln\frac{m_\pi}{\lambda}\right] \ . \end{aligned} \tag{C.13}$$

- Irreducible 2π-exchange Fock-diagram with virtual Δ-excitation.
We separate the leading contribution proportional to Δ^{-1} from the others. Using the potentials [52] (q is the momentum transfer)

$$V_C(q) = \frac{3g_A^4}{32\pi f_\pi^4\Delta}\left\{\frac{(2m_\pi^2+q^2)^2}{2q}\arctan\frac{q}{2m_\pi} + m_\pi q^2 + 4m_\pi^3\right\} \ , \tag{C.14}$$

$$W_T(q) = \frac{g_A}{128\pi f_\pi^4\Delta}\left\{\frac{4m_\pi^2+q^2}{2q}\arctan\frac{q}{2m_\pi} + m_\pi\right\} \ , \tag{C.15}$$

the contribution of the dominant two-body term is written in a closed form:

$$\dot{\mathcal{K}}_2^{(\Delta F)}(p_1,p_2) = \frac{g_A^4 m_\pi^3}{32\pi f_\pi^4\Delta}\left\{\Phi\left(\frac{p_1+p_2}{2m_\pi}\right) - \Phi\left(\frac{p_1-p_2}{2m_\pi}\right)\right\} \ , \tag{C.16}$$

with

$$\Phi(x) = 8x(3+x^2)\arctan x - 11\,\ln(1+x^2) - 148x^2 \ , \tag{C.17}$$

The remaining contribution with a non-trivial Δ-dependence is evaluated employing the spectral-representation (B.7) with the exclusion of the irreducible 2π-exchange with only intermediate nucleons (B.12) and (B.13) and of the potentials proportional to Δ^{-1} (B.17) and (B.20), which has already taken into account in eqs. (C.12) and (C.16). Differentiating the imaginary part of eq. (B.7) with respect to m_π^2, one gets:

$$\begin{aligned} \dot{\mathcal{K}}_2^{(\Delta F')}(p_1,p_2) = {} & \frac{3g_A^2}{32\pi^2 f_\pi^4}\int_{2m_\pi}^\infty \mathrm{d}\mu\left[\mu\,\ln\frac{f_+(p_1,p_2)}{f_-(p_1,p_2)} - \frac{4}{\mu}p_1p_2\right]\cdot \\ & \left\{\left[\frac{2\Delta}{\mu} + \frac{g_A^2}{8\mu\Delta}(8\Delta^2 + 40m_\pi^2 - 13\mu^2)\right]\arctan\frac{\sqrt{\mu^2-4m_\pi^2}}{2\Delta} - \frac{g_A^2\mu\,m_\pi^2}{\Delta^2\sqrt{\mu^2-4m_\pi^2}}\right. \\ & \left. + \sqrt{\mu^2-4m_\pi^2}\left[\frac{3g_A^2\mu(m_\pi^2-\Delta^2)}{(\mu^2+4\Delta^2-4m_\pi^2)^2} - \frac{2+g_A^2}{2\mu} + \frac{2g_A^2\mu(m_\pi^2-\Delta^2)-\mu\Delta^2}{2\Delta^2(\mu^2+4\Delta^2-4m_\pi^2)}\right]\right\} \ . \end{aligned} \tag{C.18}$$

The spectral representation is only once subtracted and not twice as in eq. (B.7). The associated subtraction constant proportional to the density ρ has a non-analytical dependence on the quark mass that supplies an additional contribution linear in density:

$$\begin{aligned} \dot{\mathcal{K}}_2^{(dt)}(p_1,p_2) = {} & \frac{9g_A^2\,p_1p_2}{32\pi^2 f_\pi^4}\left\{\frac{4\Delta^2 - 5g_A^2(2\Delta^2+3m_\pi^2)}{2\Delta\sqrt{\Delta^2-m_\pi^2}}\,\ln\frac{\Delta+\sqrt{\Delta^2-m_\pi^2}}{m_\pi}\right. \\ & \left. + (2-5g_A^2)\,\ln\frac{m_\pi}{2\Delta}\right\} \ . \end{aligned} \tag{C.19}$$

- 2π-exchange diagrams with c_1-contact term.
  From the isoscalar central one-loop NN-scattering amplitude [51]

$$V_C(q) = \frac{3g_A^2 c_1 m_\pi^2}{4\pi f_\pi^4}\left\{\frac{2m_\pi^2+q^2}{2q}\arctan\frac{q}{2m_\pi}+m_\pi\right\}\,, \tag{C.20}$$

  we derive

$$\dot{\mathcal{K}}_2^{(c_1)}(p_1,p_2) = \frac{g_A^2 c_1 m_\pi^3}{8\pi f_\pi^4}\left\{H\left(\frac{p_1+p_2}{2m_\pi}\right)-H\left(\frac{p_1-p_2}{2m_\pi}\right)\right\}\,, \tag{C.21}$$

  with

$$H(x) = 8x(3+x^2)\arctan x - 5\,\ln(1+x^2) - 100x^2 \tag{C.22}$$

  and the contact term $c_1 = -0.93\,\mathrm{GeV}^{-1}$.

Three-body kernels

- Iterated 1π-exchange Hartree-diagram.
  From eq. (B.26) it follows:

$$\dot{\mathcal{K}}_3^{(\mathrm{it}H)}(p_1,p_2,p_3) = \frac{3g_A^4 M_N}{2f_\pi^4}\int\limits_{p_1-p_2}^{p_1+p_2}\mathrm{d}q\,\frac{q^4}{(m_\pi^2+q^2)^3}\,\ln\frac{|p_1^2-p_2^2+q^2-2\,p_3 q|}{|p_1^2-p_2^2+q^2+2\,p_3 q|}\,. \tag{C.23}$$

- Iterated 1π-exchange Fock-diagram.
  From eq. (B.27) it follows:

$$\begin{aligned}\dot{\mathcal{K}}_3^{(\mathrm{it}F)}(p_1,p_2,p_3) = \frac{3g_A^4 M_N}{8f_\pi^4}\Bigg\{&\frac{1}{8\,p_3^3}\left[4p_1p_3+(p_3^2-p_1^2-m_\pi^2)\,\ln\frac{f_+(p_1,p_3)}{f_-(p_1,p_3)}\right]\\ &\cdot\left[\frac{2p_3(p_2+p_3)}{f_+(p_2,p_3)}+\frac{2p_3(p_2-p_3)}{f_-(p_2,p_3)}-\ln\frac{f_+(p_2,p_3)}{f_-(p_2,p_3)}\right]\\ -\int\limits_{p_2-p_3}^{p_2+p_3}&\mathrm{d}q\,\frac{q^2}{(m_\pi^2+q^2)^2}\left[\ln\frac{|p_1+h|}{|p_1-h|}+\frac{m_\pi^2}{R}\,\ln\frac{|p_1R+(p_1^2-p_3^2-m_\pi^2)h|}{|p_1R+(p_3^2-p_1^2+m_\pi^2)h|}\right]\Bigg\}\,.\end{aligned} \tag{C.24}$$

- 2π-exchange Hartree-diagram with single Δ-isobar excitation.
  From eq. (B.29) it follows:

$$\begin{aligned}\dot{\mathcal{K}}_3^{(\Delta\,H)}(p_1,p_2,p_3) = \frac{3g_A^4\,p_3}{\Delta f_\pi^4}\Bigg\{&\frac{m_\pi^4}{2f_+^2(p_1,p_2)}-\frac{m_\pi^4}{2f_-^2(p_1,p_2)}\\ &-\frac{2m_\pi^2}{f_+(p_1,p_2)}+\frac{2m_\pi^2}{f_-(p_1,p_2)}-\ln\frac{f_+(p_1,p_2)}{f_-(p_1,p_2)}\Bigg\}\,.\end{aligned} \tag{C.25}$$

- 2π-exchange Fock-diagram with single Δ-isobar excitation: From eq. (B.30) it follows:

$$\begin{aligned}\dot{\mathcal{K}}_3^{(\Delta\,F)}(p_1,p_2,p_3) = -\frac{g_A^4}{4\Delta f_\pi^4\,p_3}\Bigg\{&\left[4\,p_1p_3-m_\pi^2\,\ln\frac{f_+(p_1,p_3)}{f_-(p_1,p_3)}\right]\\ &\cdot\left[\frac{m_\pi^2}{f_-(p_2,p_3)}-\frac{m_\pi^2}{f_+(p_2,p_3)}-\ln\frac{f_+(p_2,p_3)}{f_-(p_2,p_3)}\right]\\ +\Bigg[\frac{p_1}{4p_3}&(5p_3^2-3m_\pi^2-3p_1^2)+\frac{3(p_1^2-p_3^2+m_\pi^2)^2+4m_\pi^2p_3^2}{16p_3^2}\,\ln\frac{f_+(p_1,p_3)}{f_-(p_1,p_3)}\Bigg]\\ \cdot\Bigg[\frac{3m_\pi^2+3p_2^2-p_3^2}{4p_3^2}&\,\ln\frac{f_+(p_2,p_3)}{f_-(p_2,p_3)}+\frac{m_\pi^2}{f_-(p_2,p_3)}-\frac{m_\pi^2}{f_+(p_2,p_3)}-\frac{3p_2}{p_3}\Bigg]\Bigg\}\,.\end{aligned} \tag{C.26}$$

- 2π-exchange Hartree-diagram with c_1-contact term:

$$\dot{\mathcal{K}}_3^{(c_1 H)}(p_1,p_2,p_3) = \frac{6g_A^2 c_1 p_3}{f_\pi^4}\left\{\frac{m_\pi^4}{f_+^2(p_1,p_2)} - \frac{m_\pi^4}{f_-^2(p_1,p_2)} - \frac{3m_\pi^2}{f_+(p_1,p_2)} + \frac{3m_\pi^2}{f_-(p_1,p_2)} - \ln\frac{f_+(p_1,p_2)}{f_-(p_1,p_2)}\right\} . \quad \text{(C.27)}$$

- 2π-exchange Fock-diagram with c_1-contact term:

$$\dot{\mathcal{K}}_3^{(c_1 F)}(p_1,p_2,p_3) = \frac{3g_A^2 c_1}{f_\pi^4 p_3}\left[p_2 + \frac{p_3^2 - p_2^2 - m_\pi^2}{4p_3}\ln\frac{f_+(p_2,p_3)}{f_-(p_2,p_3)}\right] \cdot \left[p_1 + \frac{p_3^2 - p_1^2 - 3m_\pi^2}{4p_3}\ln\frac{f_+(p_1,p_3)}{f_-(p_1,p_3)} + \frac{m_\pi^2(p_1+p_3)}{f_+(p_1,p_3)} + \frac{m_\pi^2(p_1-p_3)}{f_-(p_1,p_3)}\right] . \quad \text{(C.28)}$$

Anomalous contribution

From eq. (B.33) it follows:

$$\rho\dot{\bar{A}}(\rho,T) = -\frac{\Omega'_{1\pi}\dot{\Omega}'_{1\pi}}{\Omega''_0} + \frac{9g_A^4}{16f_\pi^4 T}\int_0^\infty \mathrm{d}p_1 \int_0^\infty \mathrm{d}p_2 \int_0^\infty \mathrm{d}p_3\, d(p_1)d(p_2)[2\pi^2 d(p_2) - p_2]d(p_3) \cdot \frac{1}{p_2}\left[\frac{m_\pi^2}{f_-(p_1,p_2)} - \frac{m_\pi^2}{f_+(p_1,p_2)} - \ln\frac{f_+(p_1,p_2)}{f_-(p_1,p_2)}\right]\left[p_3 - \frac{m_\pi^2}{4p_2}\ln\frac{f_+(p_3,p_2)}{f_-(p_3,p_2)}\right] , \quad \text{(C.29)}$$

with

$$\dot{\Omega}'_1 = -\frac{3g_A^2 M_N}{2f_\pi^2}\int_0^\infty \mathrm{d}p_1 \int_0^\infty \mathrm{d}p_2\, d(p_1)\frac{d(p_2)}{p_2}\left\{\frac{(p_1+p_2)^3}{f_+^2(p_1,p_2)} + \frac{(p_1-p_2)^3}{f_-^2(p_1,p_2)}\right\} . \quad \text{(C.30)}$$

Appendix D

Loop Integrals with Two Medium Insertions

D.1 Case with Two Equal Fermi Spheres

Consider the integral

$$Q = \frac{a}{2\pi} \int \mathrm{d}^3 l \; \delta(l^2 - q^2)\, \theta(k_F - |\vec{P} + \vec{l}\,|)\, \theta(k_F - |\vec{P} - \vec{l}\,|) \tag{D.1}$$

The solution is given by that portion of the spherical surface of radius $q \equiv |\vec{q}\,|$ intersecting the two Fermi spheres of radius k_F whose centers are displaced by $2P \equiv 2|\vec{P}\,|$. As showed in Fig. D.1, two cases are possible according to the length of q with respect to k_F.

a) $0 < q < k_F - P$: the intersection is the whole spherical surface of radius q.

$$Q = \frac{a}{2\pi} \int \mathrm{d}^3 l \; \delta(l^2 - q^2) = 2a \int_0^\infty \mathrm{d}l \, \frac{l^2}{2q} \; \delta(l - q) = a\, q \; . \tag{D.2}$$

b) $k_F < q < \sqrt{k_F^2 - P^2}$: the solution is the area of the spherical zone of radius q and height y. We calculate y from the intersection between the Fermi sphere and the spherical surface:

$$\left\{ \begin{array}{l} x^2 + (y+P)^2 = k_F^2 \\ x^2 + y^2 = q^2 \end{array} \right. \implies y = \frac{k_F^2 - P^2 - q^2}{2P} \; . \tag{D.3}$$

The area is

$$Q = a \int_{-y/q}^{y/q} \mathrm{d}\cos\theta \int_0^\infty \frac{l^2}{2q} \; \delta(l - q) = a\, \frac{k_F^2 - P^2 - q^2}{2P} \; . \tag{D.4}$$

Introducing the variable $s = P/k_F$ and $k = q/k_F$, the solution can be written as:

$$Q = a k_F \, I(s,k), \qquad I(s,k) = \left\{ \begin{array}{ll} k & 0 < k \leqslant 1 - s \\ \dfrac{1 - s^2 - k^2}{2s} & 1 - s < k \leqslant \sqrt{1 - s^2} \end{array} \right. \; . \tag{D.5}$$

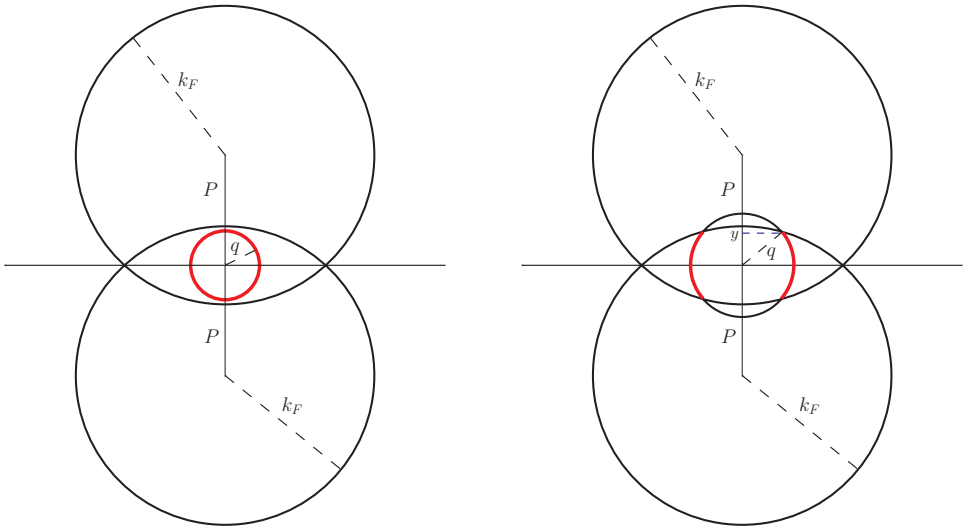

Figure D.1: Geometrical interpretation of the loop integral (D.1) with two medium insertions. The two Fermi spheres have radius k_F. The solution is given by their intersection with the spherical surface of radius q. Depending on the size of q with respect to k_F, two cases can take place.

D.2 Case with Two Different Fermi Spheres

Consider now the integration over two different Fermi spheres with radii k_p and k_n ($k_p < k_n$):

$$I_{pn} = \frac{1}{2\pi} \int \mathrm{d}^3 l \; \delta(l^2 - q^2)\, \theta(k_p - |\vec{P} + \vec{l}|)\, \theta(k_n - |\vec{P} - \vec{l}|) \; . \tag{D.6}$$

The integral has the same geometrical interpretation given for eq. (D.1). However, the two Fermi spheres have different sizes and give rise to a wider number of cases, as one can see in Fig. D.2.

a) If $q \leqslant |k_p - P|$ and $k_p \leqslant P$, there is no intersection:

$$I_{pn} = 0 \; . \tag{D.7}$$

b) If $q \leqslant |k_p - P|$ and $k_p > P$, the intersection is the whole spherical surface of radius q:

$$I_{pn} = \frac{1}{2\pi} \int \mathrm{d}^3 l \; \delta(l^2 - q^2) = q \; . \tag{D.8}$$

c) If $|k_p - P| < q \leqslant |k_n - P|$, the intersection is given by the surface of the spherical cup. The height of the cup is y:

$$\begin{cases} x^2 + (y+P)^2 = k_p^2 \\ x^2 + y^2 = q^2 \end{cases} \implies y = \frac{k_p^2 - P^2 - q^2}{2P} \; . \tag{D.9}$$

We calculate the integral:

$$I_{pn} = \int_{-1}^{y/q} \mathrm{d}\cos\theta \int_0^\infty \mathrm{d}l \; \frac{l^2}{2q} \; \delta(l - q) = \frac{k_p^2 - (P-q)^2}{4P} \; . \tag{D.10}$$

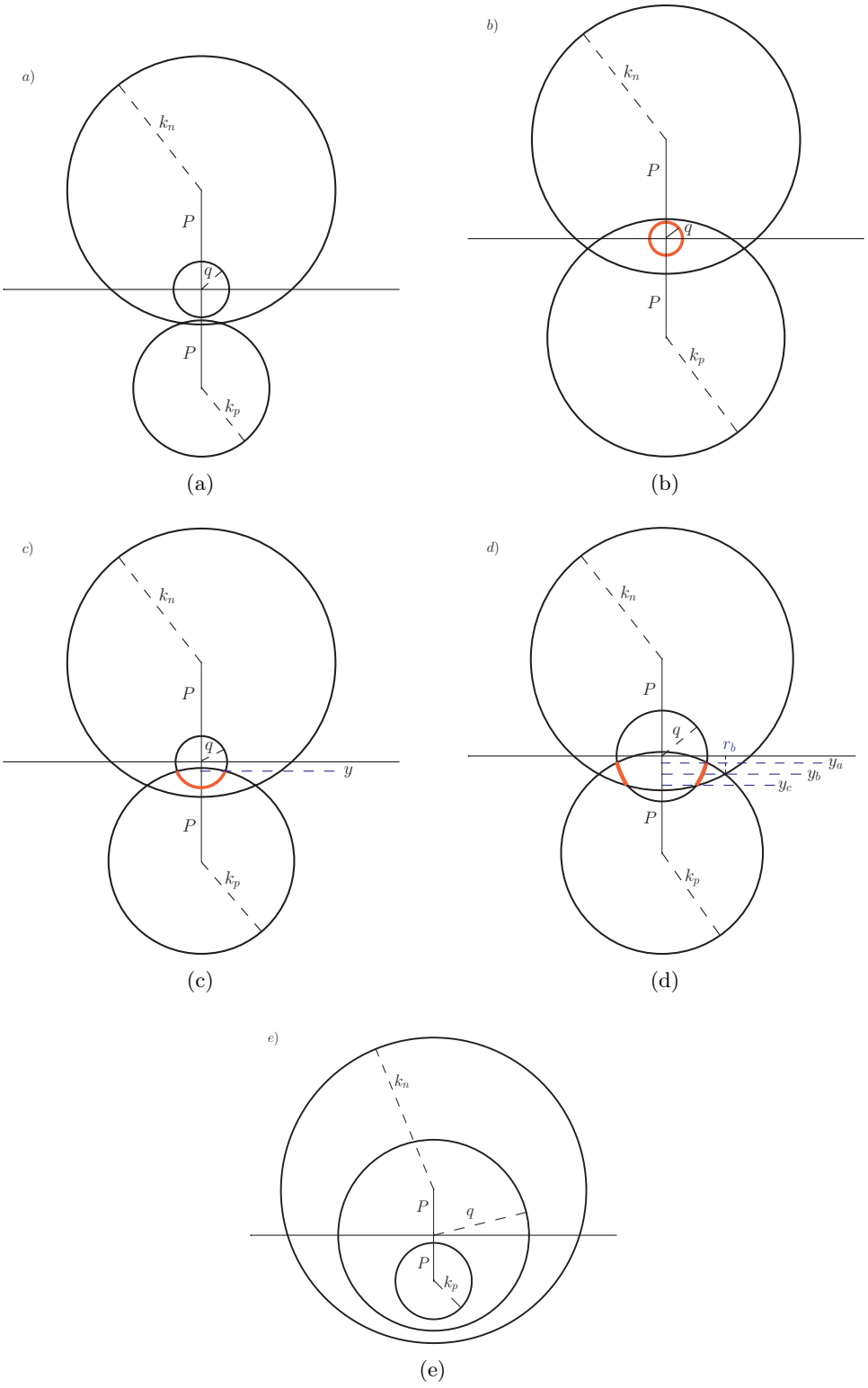

Figure D.2: Geometrical interpretation of the loop integral (D.6) with two medium insertions with two different Fermi spheres with radii k_p and k_n. All possible cases are displayed. In red we highlight the intersection between the two Fermi spheres and the spherical surface with radius q.

It becomes negative for $q > k_p + P$ loosing any physical meaning. We then exclude this region:

$$I_{pn} = 0 \quad \text{for} \quad q > k_p + P \ . \tag{D.11}$$

d) If $|k_n - P| < q \leqslant r_b$, the solution is the area of the spherical zone of radius q and height $|y_a - y_c|$. First, we calculate r_b from the intersection of the two Fermi spheres:

$$\begin{cases} x^2 + (y+P)^2 = k_p^2 \\ x^2 + (y-P)^2 = k_n^2 \end{cases} \implies r_b = \sqrt{x_b^2 + y_b^2} = \sqrt{\frac{k_p^2 + k_n^2}{2} - P^2} \ . \tag{D.12}$$

The ordinates y_a and y_c are:

$$y_a = \frac{k_p^2 - P^2 - q^2}{2P} \ , \qquad y_c = -\frac{k_n^2 - P^2 - q^2}{2P} \ . \tag{D.13}$$

Finally, we integrate:

$$I_{pn} = \int_{y_c/q}^{y_a/q} \mathrm{d}\cos\theta \int_0^\infty \mathrm{d}l \ \frac{l^2}{2q} \ \delta(l-q) = \frac{k_p^2 + k_n^2 - 2(P^2+q^2)}{4P} \ . \tag{D.14}$$

e) If $k_p + P \leqslant q < |k_n - P|$, there is no intersection:

$$I_{pn} = 0 \ . \tag{D.15}$$

We summarize the result:

$$I_{pn} = \begin{cases} 0 & q > k_p + P \\ q\,\theta(k_p - P) & q \leqslant |k_p - P| \\ \dfrac{k_p^2 - (P-q)^2}{4P} & |k_p - P| < q \leqslant |k_n - P| \\ \dfrac{k_p^2 + k_n^2 - 2(P^2+q^2)}{4P} & |k_n - P| < q \leqslant \sqrt{\frac{k_p^2+k_n^2}{2} - P^2} \end{cases} \ . \tag{D.16}$$

Fig. D.3a shows the domain of the function I_{pn} in the variables P and q. Being a piecewise function, its domain is subdivided in blocks on which it assumes a different behaviour. The alphabetical letters labeling the subdomains are in correspondence with the items of the list above and with the cases of the geometrical interpretation in Fig. D.2. Eventually, Fig. D.3b is the plot of I_{pn} corresponding to the choice of values $k_p = 7.5$ and $k_n = 16.5$.

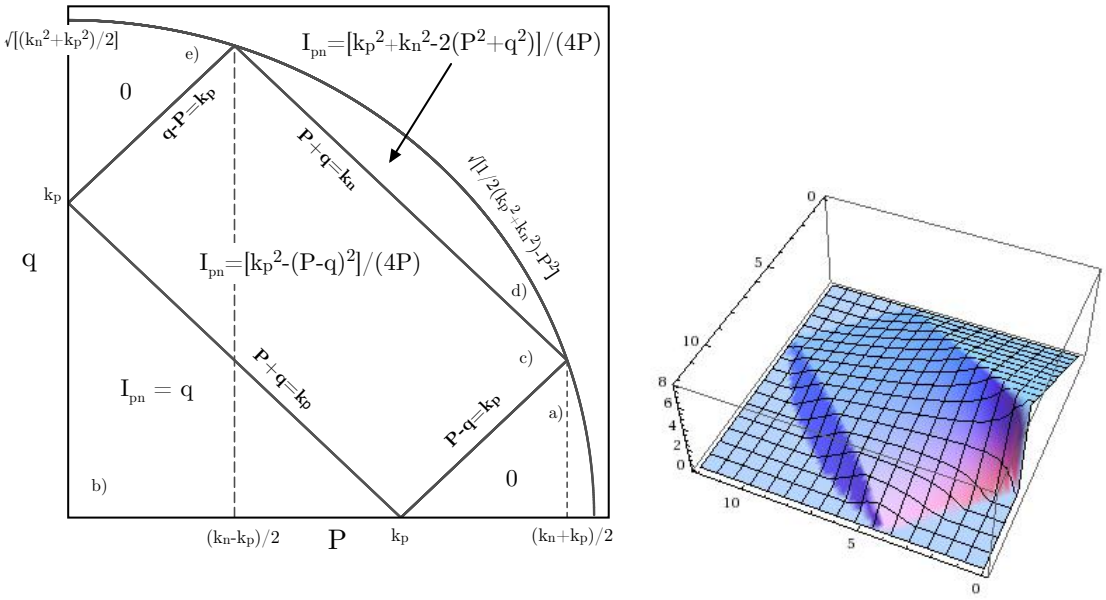

(a) (b)

Figure D.3: On the left: domain of the function I_{pn} in the variables P and q. On the right: plot of the function I_{pn} for the numerical choice $k_p = 7.5$ and $k_n = 16.5$.

Appendix E

Change of variables in the Integration over the Interior of Two Fermi Spheres

We prove the master formula (6.27) used to perform the integration over the interior of two Fermi spheres. We solve the integral

$$A = \int\limits_{|\vec{p}_{1,2}|<k_F} \frac{\mathrm{d}^3 p_1\, \mathrm{d}^3 p_2}{(2\pi)^6}\, f(s,k) = \frac{k_F^6}{8\pi^4} \int_0^1 \mathrm{d}x_1\, x_1^2 \int_0^1 \mathrm{d}x_2\, x_2^2 \int_{-1}^1 \mathrm{d}z\, f(s,k)\ , \tag{E.1}$$

with

$$s,k = \frac{1}{2}\sqrt{x_1^2 + x_2^2 \pm 2x_1 x_2 z}\ . \tag{E.2}$$

The integral A is symmetric under the exchange $x_1 \leftrightarrow x_2$. As one can see in Fig. E.1a, the domain of integration in x_1 and x_2 is defined over a square of unitary side. Due to the symmetry, A can be rewritten as twice an integration over one of the triangle delimited by the straight line $x_1 = x_2$:

$$A = \frac{k_F^6}{4\pi^4} \int_0^1 \mathrm{d}x_1\, x_1^2 \int_0^{x_1} \mathrm{d}x_2\, x_2^2 \int_{-1}^1 \mathrm{d}z\, f(s,k)\ . \tag{E.3}$$

We change the integration variable z in k using eq. (E.2). We obtain:

$$A = \frac{k_F^6}{\pi^4} \int_0^1 \mathrm{d}x_1\, x_1 \int_0^{x_1} \mathrm{d}x_2\, x_2 \int_{\frac{x_1-x_2}{2}}^{\frac{x_1+x_2}{2}} \mathrm{d}k\, k\, f(s,k)\ . \tag{E.4}$$

We exchange the order of integration between k and x_2 using Fig. E.1b to calculate the new integration intervals. The grey region is the domain of integration. The red band indicates the initial order of integration, the green band the final one after the exchange. This leads to:

$$A = \frac{k_F^6}{\pi^4} \int_0^1 \mathrm{d}x_1\, x_1 \int_0^{x_1} \mathrm{d}k\, k \int\limits_{|2k-x_1|}^{x_1} \mathrm{d}x_2\, x_2\, f(s,k)\ . \tag{E.5}$$

The next step is the replacement of the variable x_2 with s. Employing the relation

$$s^2 + k^2 = \frac{1}{2}\left(x_1^2 + x_2^2\right) \qquad \longrightarrow \qquad 2s\,\mathrm{d}s = x_2\,\mathrm{d}x_2\ , \tag{E.6}$$

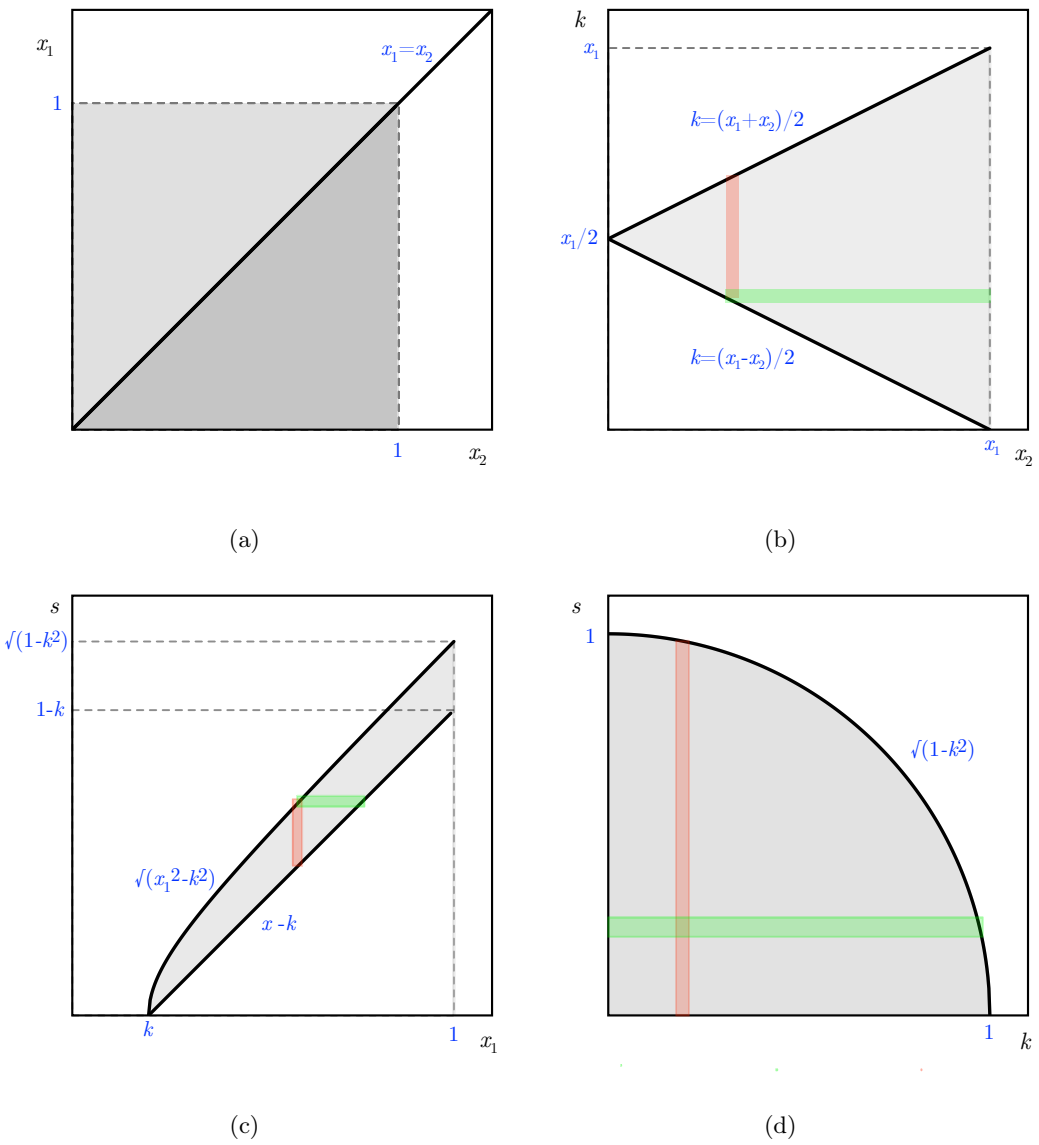

Figure E.1: The grey region shows the domain of integration of A in the variables labeling the axes. In the plot (a), A can be calculated as twice the integral over one of the triangles because of its symmetry under the exchange $x_1 \leftrightarrow x_2$. The other plots are used to change the order of integration in A. Initially A is first integrated over the vertical axis (red band) and then over the horizontal one. The exchange of the order implies to start with the integration over the horizontal axis (green band).

the integral becomes:

$$A = \frac{2k_F^6}{\pi^4} \int_0^1 \mathrm{d}x_1\, x_1 \int_0^{x_1} \mathrm{d}k\, k \int_{x_1-k}^{\sqrt{x_1^2-k^2}} \mathrm{d}s\, s\, f(s,k)$$
$$= \frac{2k_F^6}{\pi^4} \int_0^1 \mathrm{d}k\, k \int_k^1 \mathrm{d}x_1\, x_1 \int_{x_1-k}^{\sqrt{x_1^2-k^2}} \mathrm{d}s\, s\, f(s,k)\ . \tag{E.7}$$

In the second line we have exchanged the order of integration between x_1 and k. And now we exchange the order between s and x_1 with the help of Fig. E.1c:

$$A = \frac{2k_F^6}{\pi^4} \int_0^1 \mathrm{d}k\, k \int_0^{\sqrt{1-k^2}} \mathrm{d}s\, s \left[\int_{\sqrt{s^2+k^2}}^{s+k} \mathrm{d}x_1\, x_1\, \theta(1-s-k) + \int_{\sqrt{s^2+k^2}}^{1} \mathrm{d}x_1\, x_1\, \theta(s+k-1) \right] f(s,k)\ . \tag{E.8}$$

The integration in x_1 is easily carried out:

$$A = \frac{2k_F^6}{\pi^4} \int_0^1 \mathrm{d}k\, k \int_0^{\sqrt{1-k^2}} \mathrm{d}s\, s \left[ks\, \theta(1-s-k) + \frac{1-s^2-k^2}{2}\, \theta(s+k-1) \right] f(s,k)\ . \tag{E.9}$$

As last step we change the order of integration between s and k (Fig. E.1d):

$$A = \frac{2k_F^6}{\pi^4} \int_0^1 \mathrm{d}s\, s^2 \int_0^{\sqrt{1-s^2}} \mathrm{d}k\, k \left[k\, \theta(1-s-k) + \frac{1-s^2-k^2}{2s}\, \theta(s+k-1) \right] f(s,k)$$
$$= \frac{2k_F^6}{\pi^4} \int_0^1 \mathrm{d}s\, s^2 \int_0^{\sqrt{1-s^2}} \mathrm{d}k\, k\, I(s,k)\, f(s,k)\ , \tag{E.10}$$

where we have used the definition of the function $I(s,k)$ eq. (D.5).

Bibliography

[1] F. Ozel, G. Baym and T. Guver, "Astrophysical Measurement of the Equation of State of Neutron Star Matter," Phys. Rev. D **82** (2010) 101301 [arXiv:1002.3153 [astro-ph.HE]].

[2] A. W. Steiner, J. M. Lattimer and E. F. Brown, "The Equation of State from Observed Masses and Radii of Neutron Stars," Astrophys. J. **722** (2010) 33 [arXiv:1005.0811 [astro-ph.HE]].

[3] P. Demorest, T. Pennucci, S. Ransom, M. Roberts and J. Hessels, "Shapiro Delay Measurement of A Two Solar Mass Neutron Star," Nature **467** (2010) 1081 [arXiv:1010.5788 [astro-ph.HE]].

[4] K. Hebeler, J. M. Lattimer, C. J. Pethick and A. Schwenk, "Constraints on neutron star radii based on chiral effective field theory interactions," Phys. Rev. Lett. **105** (2010) 161102 [arXiv:1007.1746 [nucl-th]].

[5] V. G. J. Stoks, R. A. M. Kompl, M. C. M. Rentmeester and J. J. de Swart, "Partial wave analysis of all nucleon-nucleon scattering data below 350-MeV," Phys. Rev. C **48**, 792 (1993).

[6] V. G. J. Stoks, R. A. M. Klomp, C. P. F. Terheggen and J. J. de Swart, "Construction of high quality N N potential models," Phys. Rev. C **49** (1994) 2950 [nucl-th/9406039].

[7] R. B. Wiringa, V. G. J. Stoks and R. Schiavilla, "An Accurate nucleon-nucleon potential with charge independence breaking," Phys. Rev. C **51** (1995) 38 [nucl-th/9408016].

[8] R. Machleidt, "The high-precision, charge-dependent Bonn nucleon-nucleon potential (CD-Bonn)," Phys. Rev. C **63** (2001) 024001 [arXiv:nucl-th/0006014].

[9] I. E. Lagaris and V. R. Pandharipande, "Phenomenological Two Nucleon Interaction Operator," Nucl. Phys. A **359** (1981) 331.

[10] I. E. Lagaris and V. R. Pandharipande, "Variational Calculations Of Realistic Models Of Nuclear Matter," Nucl. Phys. A **359** (1981) 349.

[11] E. Epelbaum, "Four-nucleon force using the method of unitary transformation," Eur. Phys. J. A **34** (2007) 197 [arXiv:0710.4250 [nucl-th]].

[12] E. Epelbaum, H. -W. Hammer and U. -G. Meissner, "Modern Theory of Nuclear Forces," Rev. Mod. Phys. **81** (2009) 1773 [arXiv:0811.1338 [nucl-th]].

[13] P. A. Seeger and W. M. Howard, "Semiempirical atomic mass formula," Nucl. Phys. A **238** (1975) 491.

[14] D. H. E. Gross, "Statistical decay of very hot nuclei: The Production of large clusters," Rept. Prog. Phys. **53** (1990) 605.

[15] J. Pochodzalla, T. Mohlenkamp, T. Rubehn, A. Schuttauf, A. Worner, E. Zude, M. Begemann-Blaich and T. .Blaich *et al.*, "Probing the nuclear liquid - gas phase transition," Phys. Rev. Lett. **75** (1995) 1040.

[16] J. B. Natowitz, R. Wada, K. Hagel, T. Keutgen, M. Murray, Y. G. Ma, A. Makeev and L. Qin *et al.*, "Caloric curves and critical behavior in nuclei," Phys. Rev. C **65** (2002) 034618 [nucl-ex/0106016].

[17] K. A. Brueckner, S. A. Coon and J. Dabrowski, "Nuclear Symmetry Energy," Phys. Rev. **168** (1968) 1184.

[18] B. A. Li, L. W. Chen and C. M. Ko, "Recent Progress and New Challenges in Isospin Physics with Heavy-Ion Reactions," Phys. Rept. **464**, 113 (2008) [arXiv:0804.3580 [nucl-th]].

[19] A. Lejeune, P. Grange, M. Martzolff and J. Cugnon, "Hot nuclear matter in an extended brueckner approach," Nucl. Phys. A **453** (1986) 189.

[20] J. Cugnon, P. Deneye and A. Lejeune, "Neutron Matter Properties In An Extended Bruckner Approach," Z. Phys. A **328** (1987) 409.

[21] I. Bombaci and U. Lombardo, "Asymmetric Nuclear Matter Equation Of State," Phys. Rev. C **44**, 1892 (1991).

[22] I. E. Lagaris and V. R. Pandharipande, "Variational Calculations Of Realistic Models Of Nuclear Matter," Nucl. Phys. A **359** (1981) 349.

[23] B. Friedman and V. R. Pandharipande, "Hot and cold, nuclear and neutron matter," Nucl. Phys. A **361** (1981) 502.

[24] R. B. Wiringa, V. Fiks and A. Fabrocini, "Equation of state for dense nucleon matter," Phys. Rev. C **38** (1988) 1010.

[25] A. Akmal, V. R. Pandharipande and D. G. Ravenhall, "The Equation of nucleon matter and neutron star structure," Phys. Rev. C **58** (1998) 1804.

[26] A. Mukherjee and V. R. Pandharipande, "Variational Theory of Hot Nucleon Matter," Phys. Rev. C **75** (2007) 035802 [nucl-th/0609058].

[27] P. Armani, A. Y. Illarionov, D. Lonardoni, F. Pederiva, S. Gandolfi, K. E. Schmidt and S. Fantoni, "Recent progress on the accurate determination of the equation of state of neutron and nuclear matter," J. Phys. Conf. Ser. **336** (2011) 012014 [arXiv:1110.0993 [nucl-th]].

[28] E. Campani, S. Fantoni and S. Rosati, "The Fermion Hypernetted chain and the Percus-Yevick Approximation," Nuovo Cim. **12** (1975) 1975.

[29] S. Fantoni and S. Rosati, "The Fermi-Hypernetted-Chain Method for State-Dependent Jastrow-Correlated Functions," Nuovo Cim. **43** (1978) 431.

[30] S. Fantoni and S. Rosati, "Extension of the FHNC Method to Finite Systems," Nucl. Phys. A **328** (1979) 478.

[31] O. Benhar, C. Ciofi degli Atti, S. Fantoni and S. Rosati, "Variational Calculation on Nuclear Matter," Nucl. Phys. A **328** (1979) 127.

[32] Y. Dewulf, D. Van Neck and M. Waroquier, "Effects of selfconsistency in a Green's function description of saturation in nuclear matter," Phys. Rev. C **65** (2002) 054316.

[33] J. Carlson, J. Morales, Jr., V. R. Pandharipande and D. G. Ravenhall, "Quantum Monte Carlo calculations of neutron matter," Phys. Rev. C **68** (2003) 025802 [nucl-th/0302041].

[34] V. Soma and P. Bozek, "In medium T-matrix for nuclear matter with three-body forces: Binding energy and single particle properties," Phys. Rev. C **78** (2008) 054003 [arXiv:0808.2929 [nucl-th]].

[35] R. Brockmann and R. Machleidt, "Nuclear Saturation In A Relativistic Bruckner-hartree-fock Approach," Phys. Lett. B **149** (1984) 283.

[36] C. J. Horowitz and B. D. Serot, "The Relativistic Two Nucleon Problem In Nuclear Matter," Nucl. Phys. A **464** (1987) 613 [Erratum-ibid. A **473** (1987) 760].

[37] R. Brockmann and R. Machleidt, "Relativistic nuclear structure. 1: Nuclear matter," Phys. Rev. C **42** (1990) 1965.

[38] L. Sehn, C. Fuchs and A. Faessler, "Nucleon selfenergy in the relativistic Bruckner approach," Phys. Rev. C **56** (1997) 216 [nucl-th/9701060].

[39] C. Fuchs, T. Waindzoch, A. Faessler and D. S. Kosov, "Scalar and vector decomposition of the nucleon self-energy in the relativistic Brueckner approach," Phys. Rev. C **58** (1998) 2022.

[40] T. Gross-Boelting, C. Fuchs and A. Faessler, "Covariant representations of the relativistic Bruckner T matrix and the nuclear matter problem," Nucl. Phys. A **648** (1999) 105 [nucl-th/9810071].

[41] E. N. E. van Dalen, C. Fuchs and A. Faessler, "The Relativistic Dirac-Brueckner approach to asymmetric nuclear matter," Nucl. Phys. A **744** (2004) 227 [nucl-th/0407070].

[42] B. D. Serot and J. D. Walecka, "The Relativistic Nuclear Many Body Problem," Adv. Nucl. Phys. **16** (1986) 1.

[43] D. Hirata, H. Toki, T. Watabe, I. Tanihata and B. V. Carlson, "Relativistic Hartree theory for nuclei far from the stability line," Phys. Rev. C **44** (1991) 1467.

[44] H. Shen, Y. Sugahara and H. Toki, "Relativistic mean field approach with density dependent couplings for finite nuclei," Phys. Rev. C **55** (1997) 1211.

[45] T. H. R. Skyrme, "CVII. The nuclear surface," Phil. Mag. **1** (1956) 1043.

[46] T. Skyrme, "The effective nuclear potential," Nucl. Phys. **9** (1959) 615.

[47] J. W. Negele and D. Vautherin, "Density-Matrix Expansion for an Effective Nuclear Hamiltonian," Phys. Rev. C **5** (1972) 1472.

[48] G. Sauer, H. Chandra and U. Mosel, "Thermal properties of nuclei," Nucl. Phys. A, **264** (1976) 221.

[49] S. Weinberg, "Phenomenological Lagrangians," Physica A **96** (1979) 327.

[50] D. B. Kaplan, M. J. Savage and M. B. Wise, "Two nucleon systems from effective field theory," Nucl. Phys. B **534** (1998) 329 [nucl-th/9802075].

[51] N. Kaiser, R. Brockmann and W. Weise, "Peripheral nucleon nucleon phase shifts and chiral symmetry," Nucl. Phys. A **625** (1997) 758 [arXiv:nucl-th/9706045].

[52] N. Kaiser, S. Gerstendorfer and W. Weise, "Peripheral N N scattering: Role of Delta excitation, correlated two-pion and vector meson exchange," Nucl. Phys. A **637** (1998) 395 [arXiv:nucl-th/9802071].

[53] M. F. M. Lutz, B. Friman and C. Appel, "Saturation from nuclear pion dynamics," Phys. Lett. B **474** (2000) 7 [arXiv:nucl-th/9907078].

[54] N. Kaiser, S. Fritsch and W. Weise, "Chiral dynamics and nuclear matter," Nucl. Phys. A **697**, 255 (2002) [arXiv:nucl-th/0105057].

[55] S. Fritsch, N. Kaiser and W. Weise, "Chiral approach to nuclear matter: Role of two-pion exchange with virtual Delta-isobar excitation," Nucl. Phys. A **750**, 259 (2005) [arXiv:nucl-th/0406038].

[56] R. Machleidt and D. R. Entem, "Chiral effective field theory and nuclear forces," Phys. Rept. **503**, 1 (2011) [arXiv:1105.2919 [nucl-th]].

[57] N. Kaiser, "Resummation of fermionic in-medium ladder diagrams to all orders," Nucl. Phys. A **860** (2011) 41 [arXiv:1102.2154 [nucl-th]].

[58] B. D. Serot and J. D. Walecka, "Recent progress in quantum hadrodynamics," Int. J. Mod. Phys. E **6** (1997) 515 [nucl-th/9701058].

[59] N. Kaiser, S. Fritsch and W. Weise, "Nuclear energy density functional from chiral pion nucleon dynamics," Nucl. Phys. A **724** (2003) 47 [nucl-th/0212049].

[60] D. Vretenar,"Nuclear Energy Density Functionals Constrained by Low-Energy QCD," Eur. Phys. J. ST **156** (2008) 37 [arXiv:0802.0838 [nucl-th]].

[61] N. Kaiser and W. Weise, "Nuclear energy density functional from chiral pion-nucleon dynamics revisited," Nucl. Phys. A **836** (2010) 256 [arXiv:0912.3207 [nucl-th]].

[62] A. Manohar and H. Georgi, "Chiral Quarks And The Nonrelativistic Quark Model," Nucl. Phys. B **234** (1984) 189.

[63] K. Nakamura et al. (Particle Data Group), JP G 37, 075021 (2010).

[64] J. Gasser, M. E. Sainio and A. Svarc, "Nucleons With Chiral Loops," Nucl. Phys. B **307** (1988) 779.

[65] E. E. Jenkins and A. V. Manohar, "Baryon chiral perturbation theory using a heavy fermion Lagrangian," Phys. Lett. B **255** (1991) 558.

[66] S. Weinberg, "Effective chiral Lagrangians for nucleon - pion interactions and nuclear forces," Nucl. Phys. B **363** (1991) 3.

[67] S. Weinberg, "Nuclear forces from chiral Lagrangians," Phys. Lett. B **251**, 288 (1990).

[68] S. Weinberg, "Three body interactions among nucleons and pions," Phys. Lett. B **295**, 114 (1992) [arXiv:hep-ph/9209257].

[69] E. Epelbaum, "Few-nucleon forces and systems in chiral effective field theory," Prog. Part. Nucl. Phys. **57**, 654 (2006) [arXiv:nucl-th/0509032].

[70] T. R. Hemmert, B. R. Holstein and J. Kambor, "Chiral Lagrangians and Delta(1232) interactions: Formalism," J. Phys. G **24** (1998) 1831 [arXiv:hep-ph/9712496].

[71] V. Bernard, N. Kaiser and U. G. Meissner, "Determination of the low-energy constants of the next-to-leading order chiral pion nucleon Lagrangian," Nucl. Phys. A **615**, 483 (1997) [arXiv:hep-ph/9611253].

[72] E. Epelbaum, H. Krebs and U. G. Meissner, "Delta-excitations and the three-nucleon force," Nucl. Phys. A **806**, 65 (2008) [arXiv:0712.1969 [nucl-th]].

[73] A. Nogga, D. Rozpędzik, E. Epelbaum, W. Glöckle, J. Golak, H. Hamada, R. Skibiński, H. Witała, "Four-nucleon force contribution to the binding energy of 4He," EPJ Web of Conferences **3** (2010) 05006.

[74] A. L. Fetter, J. D. Walecka, *Quantum Theory of Many-Particle Systems*, Dover Publications, 2003.

[75] G. D. Mahan, *Many-Particle Physics*, second edition, Plenum Press, New York, 1990.

[76] S. Fiorilla, N. Kaiser and W. Weise, "Chiral thermodynamics of nuclear matter," Nucl. Phys. A **880** (2012) 65 [arXiv:1111.2791 [nucl-th]].

[77] T. Ericson, W. Weise, *Pions and Nuclei*, Oxford University Press, 1988.

[78] W. Kohn and J. M. Luttinger, "Ground-State Energy of a Many-Fermion System," Phys. Rev. **118** (1960) 41.

[79] J. M. Luttinger and J. C. Ward, "Ground state energy of a many fermion system. 2," Phys. Rev. **118** (1960) 1417.

[80] S. Fritsch, N. Kaiser and W. Weise, "Chiral dynamics of nuclear matter at finite temperature," Phys. Lett. B **545** (2002) 73 [arXiv:nucl-th/0202005].

[81] C. J. Horowitz and A. Schwenk, "The Virial Equation of State of Low-Density Neutron Matter," Phys. Lett. B **638**, 153 (2006) [arXiv:nucl-th/0507064].

[82] D. Vretenar, T. Niksic and P. Ring, "A microscopic estimate of the nuclear matter compressibility and symmetry energy in relativistic mean-field models," Phys. Rev. C **68**, 024310 (2003) [arXiv:nucl-th/0302070].

[83] L. W. Chen, B. J. Cai, C. M. Ko, B. A. Li, C. Shen and J. Xu, "High-order effects on the incompressibility of isospin asymmetric nuclear matter," Phys. Rev. C **80**, 014322 (2009) [arXiv:0905.4323 [nucl-th]].

[84] W. Reisdorf, "Constraints on the equation of state of nuclear matter from nucleus-nucleus collisions," Nucl. Phys. A, **734** (2004) 565.

[85] V. A. Karnaukhov *et al.*, "Critical temperature for the nuclear liquid-gas phase transition (from multifragmentation and fission)," Phys. Atom. Nucl. **71** (2008) 2067 [arXiv:0801.4485 [nucl-ex]].

[86] J. B. Natowitz, K. Hagel, Y. Ma, M. Murray, L. Qin, R. Wada and J. Wang, "Limiting temperatures and the Equation of State of Nuclear Matter," Phys. Rev. Lett. **89**, 212701 (2002) [arXiv:nucl-ex/0204015].

[87] S. Typel, G. Ropke, T. Klahn, D. Blaschke and H. H. Wolter, "Composition and thermodynamics of nuclear matter with light clusters," Phys. Rev. C **81** (2010) 015803 [arXiv:0908.2344 [nucl-th]].

[88] D. E. Gonzalez Trotter, F. S. Meneses, W. Tornow, C. R. Howell, Q. Chen, A. S. Crowell, C. D. Roper and R. L. Walter *et al.*, "Neutron-deuteron breakup experiment at $E(n) = 13$ MeV: Determination of the $^1S_0$ neutron-neutron scattering length a_{nn}," Phys. Rev. C **73** (2006) 034001.

[89] Q. Chen, C. R. Howell, T. S. Carman, W. R. Gibbs, B. F. Gibson, A. Hussein, M. R. Kiser and G. Mertens *et al.*, "Measurement of the neutron-neutron scattering length using the pi-d capture reaction," Phys. Rev. C **77** (2008) 054002.

[90] L. G. Cao and Z. Y. Ma, "Symmetry Energy and Isovector Giant Dipole Resonance in Finite Nuclei," Chin. Phys. Lett. **25**, 1625 (2008).

[91] J. P. Blaizot, "Nuclear Compressibilities," Phys. Rept. **64**, 171 (1980).

[92] P. A. Seeger and W. M. Howard, "Semiempirical atomic mass formula," Nucl. Phys. A, **238** (1975) 491.

[93] T. Li *et al.*, "Isotopic dependence of the giant monopole resonance in the even-A $^{112-124}$Sn isotopes and the asymmetry term in nuclear incompressibility," Phys. Rev. Lett. **99**, 162503 (2007) [arXiv:0709.0567 [nucl-ex]].

[94] A. Rios, A. Polls, A. Ramos and H. Muther, "Liquid-gas phase transition in nuclear matter from realistic many-body approaches," Phys. Rev. C **78**, 044314 (2008) [arXiv:0805.2318 [nucl-th]].

[95] I. Vidana, C. Providencia, A. Polls and A. Rios, "Density dependence of the nuclear symmetry energy: a microscopic perspective," Phys. Rev. C **80**, 045806 (2009) [arXiv:0907.1165 [nucl-th]].

[96] A. Rios, "Effective interaction dependence of the liquid-gas phase transition in symmetric nuclear matter," Nucl. Phys. A **845**, 58 (2010) [arXiv:1002.1907 [nucl-th]].

[97] V. Soma and P. Bozek, "Thermodynamic properties of nuclear matter with three-body forces," Phys. Rev. C **80** (2009) 025803 [arXiv:0904.1169 [nucl-th]].

[98] C. Wu and Z. Ren, "Liquid-gas phase transition in hot asymmetric nuclear matter," Phys. Rev. C **83**, 044605 (2011).

[99] P. Gerber and H. Leutwyler, "Hadrons Below the Chiral Phase Transition," Nucl. Phys. B **321** (1989) 387.

[100] Y. Aoki, Z. Fodor, S. D. Katz and K. K. Szabo, "The QCD transition temperature: Results with physical masses in the continuum limit," Phys. Lett. B **643** (2006) 46 [hep-lat/0609068].

[101] A. Bazavov, T. Bhattacharya, M. Cheng, C. DeTar, H. T. Ding, S. Gottlieb, R. Gupta and P. Hegde *et al.*, "The chiral and deconfinement aspects of the QCD transition," Phys. Rev. D **85** (2012) 054503 [arXiv:1111.1710 [hep-lat]].

[102] , *et al.* [HotQCD Collaboration], "The chiral transition and $U(1)_A$ symmetry restoration from lattice QCD using Domain Wall Fermions," arXiv:1205.3535 [hep-lat].

[103] S. Fiorilla, N. Kaiser and W. Weise, "Nuclear thermodynamics and the in-medium chiral condensate," Phys. Lett. B **714** (2012) 251 [arXiv:1204.4318 [nucl-th]].

[104] J. Gasser, H. Leutwyler and M. E. Sainio, "Sigma term update," Phys. Lett. B **253** (1991) 252.

[105] S. Durr, Z. Fodor, T. Hemmert, C. Hoelbling, J. Frison, S. D. Katz, S. Krieg and T. Kurth *et al.*, "Sigma term and strangeness content of octet baryons," Phys. Rev. D **85** (2012) 01450 [arXiv:1109.4265 [hep-lat]].

[106] A. Semke and M. F. M. Lutz, "On the quark-mass dependence of the baryon ground-state masses," Phys. Rev. D **85** (2012) 034001 [arXiv:1111.0238 [hep-ph]].

[107] N. Kaiser, P. de Homont and W. Weise, "In-medium chiral condensate beyond linear density approximation," Phys. Rev. C **77** (2008) 025204 [arXiv:0711.3154 [nucl-th]].

[108] N. Ishii, S. Aoki and T. Hatsuda, "The Nuclear Force from Lattice QCD," Phys. Rev. Lett. **99** (2007) 022001 [nucl-th/0611096].

[109] S. Aoki, T. Hatsuda and N. Ishii, "Theoretical Foundation of the Nuclear Force in QCD and its applications to Central and Tensor Forces in Quenched Lattice QCD Simulations," Prog. Theor. Phys. **123** (2010) 89 [arXiv:0909.5585 [hep-lat]].

[110] J. Gasser and H. Leutwyler, "Chiral Perturbation Theory to One Loop," Annals Phys. **158** (1984) 142.

[111] G. Colangelo, J. Gasser and H. Leutwyler, "pi pi scattering," Nucl. Phys. B **603** (2001) 125 [hep-ph/0103088].

[112] M. Procura, B. U. Musch, T. R. Hemmert and W. Weise, "Chiral extrapolation of g(A) with explicit Delta(1232) degrees of freedom," Phys. Rev. D **75** (2007) 014503 [hep-lat/0610105].

[113] M. Procura, B. U. Musch, T. Wollenweber, T. R. Hemmert and W. Weise, "Nucleon mass: From lattice QCD to the chiral limit," Phys. Rev. D **73** (2006) 114510 [hep-lat/0603001].

[114] O. Plohl and C. Fuchs, "Nuclear matter in the chiral limit and the in-medium chiral condensate," Nucl. Phys. A **798** (2008) 75 [arXiv:0710.3700 [nucl-th]].

[115] N. Kaiser, "pi pi scattering lengths at finite temperature," Phys. Rev. C **59** (1999) 2945.

[116] N. Kaiser and W. Weise, "Chiral condensate in neutron matter," Phys. Lett. B **671** (2009) 25 [arXiv:0808.0856 [nucl-th]].

[117] D. E. Gonzalez Trotter, F. S. Meneses, W. Tornow, C. R. Howell, Q. Chen, A. S. Crowell, C. D. Roper and R. L. Walter *et al.*, "Neutron-deuteron breakup experiment at E(n) = 13-MeV: Determination of the (1)S(0) neutron-neutron scattering length ann," Phys. Rev. C **73** (2006) 034001.

[118] Q. Chen, C. R. Howell, T. S. Carman, W. R. Gibbs, B. F. Gibson, A. Hussein, M. R. Kiser and G. Mertens *et al.*, "Measurement of the neutron-neutron scattering length using the pi-d capture reaction," Phys. Rev. C **77** (2008) 054002.

[119] H. W. Hammer and R. J. Furnstahl, "Effective field theory for dilute Fermi systems," Nucl. Phys. A **678** (2000) 277 [nucl-th/0004043].

[120] J. V. Steele, "Effective field theory power counting at finite density," nucl-th/0010066.

[121] M. M. Forbes, S. Gandolfi and A. Gezerlis, "Resonantly Interacting Fermions In a Box," Phys. Rev. Lett. **106** (2011) 235303 [arXiv:1011.2197 [cond-mat.quant-gas]].

[122] A. Gezerlis and J. Carlson, "Low-density neutron matter," Phys. Rev. C **81** (2010) 025803 [arXiv:0911.3907 [nucl-th]].

[123] M. Bartenstein, A. Altmeyer, S. Riedl, S. Jochim, C. Chin, J. H. Denschlag and R. Grimm, "Crossover from a Molecular Bose-Einstein Condensate to a Degenerate Fermi Gas," Phys. Rev. Lett. **92** (2004) 120401.

[124] T. Bourdel, L. Khaykovich, J. Cubizolles, J. Zhang, F. Chevy, M. Teichmann, L. Tarruell and S. J. J. M. F. Kokkelmans *et al.*, "Experimental Study of the BEC-BCS Crossover Region in Lithium 6," Phys. Rev. Lett. **93** (2004) 050401.

[125] M. E. Peskin, D. V. Scroeder, *Quantum Field Theory*, Perseus Books, 1995.

[126] L. Dolan and R. Jackiw, "Symmetry Behavior At Finite Temperature," Phys. Rev. D **9** (1974) 3320.

[127] H. A. Weldon, "Covariant Calculations At Finite Temperature: The Relativistic Plasma," Phys. Rev. D **26** (1982) 1394.

[128] M. Le Bellac, *Thermal Field Theory*, Cambridge University Press, 1996.

Acknowledgements

Before dropping the curtain over the PhD period of my life, the last one as a student, and venturing again out into the unknown, I would like to thank all those who shared these years with me:

- the mythologic coffee machine Rommelsbacher, because without the precious liquid arising from it I would have never achieved to finish this thesis;
- Prof. Wolfram Weise, for giving me the opportunity to come to Munich and for his support and patience;
- Prof. Norbert Kaiser, for proving to me that even the uncalculable can be calculated quite reasonably with a good approximation in an elegant way;
- Jeremy Holt, for nice work and out-of-work discussions;
- Nino Bratovic, for showing my small liquid-gas phase transition in his QCD phase diagram;
- Stephan Petschauer, with his hyper(ionic)-cakes;
- Sebastian Schultess, for being interested in my slides;
- Thomas Hell, for planning everything punctually;
- Alexander Laschka, for updating the computers and planning punctually with Thomas;
- Matthias Drews, for learning italian with a french book;
- Robert Lang, for greeting me in chinese;
- Maximilian Duell, for the inauguration of the "coffice" and the paramecius-hunting in the Isar;
- Michael Altenbuchinger, whom I made addicted to the caffeine;
- Corbinian Wellenhofer, for reading my paper;
- the squirrel Nino, for jumping and walking seasonally in front of my office;
- Who passed through here, like Lisheng Geng, Kouji Kashiwa and many others.
- Daniele, for calling me still after four years, and MWG.